Title
Electrochemical Insights on Materials for Next-Generation Batteries

Author
Whang, Grace

Publication Date
2022

Peer reviewed|Thesis/dissertation

UNIVERSITY OF CALIFORNIA
Los Angeles

Electrochemical Insights on Materials for Next-Generation Batteries

A dissertation submitted in partial satisfaction of the requirements for the degree Doctor of Philosophy in Materials Science and Engineering

by

Grace Jeeae Whang

2022

ABSTRACT OF THE DISSERTATION

Electrochemical Insights on Materials for Next-Generation Batteries

by

Grace Jeeae Whang

Doctor of Philosophy in Materials Science and Engineering

University of California, Los Angeles, 2022

Professor Bruce Dunn, Chair

The development of the lithium-ion battery has played an indispensable role in shaping the landscape of portable electronics and emerging electric vehicle industry. While its development has been recognized with a Nobel Prize in 2019, battery technology is far from mature. Since its conception, the battery research landscape has only widened with the rise of electric vehicles and wearable devices, each having a different set of requirements. Therefore, the “next-generation” in the context of this dissertation focuses on two different aspects of the battery field. The first aspect considers the development of high energy density batteries and more specifically the move away from capacity-limited intercalation chemistries. Chapter 3 delves into the interfacial challenges posed by lithium metal anodes during the Li plating/stripping reactions while Chapter 4 visits the complex reaction pathways in FeS_2 conversion cathodes to understand charge product formation and identify capacity loss mechanisms. While both Li and FeS_2 are commercialized as primary battery electrode materials and have the potential to provide high energy density rechargeable batteries, safety and performance issues have limited their use

to primary systems. Ultimately, better understanding of the interfaces and reaction pathways can fuel the design of solutions to improve the performance and safety of these systems. The latter part of the dissertation focuses on the other type of “next-generation” battery, namely, that of miniaturized power sources for IoT technologies. With the vision of an on-chip battery integrated into a device, new materials and processes must be developed to integrate the same semiconductor processing techniques used to make the device to make the batteries as well. Chapter 5 details the development of a conformal, photopatternable separator and the integration of the separator onto various battery architectures. The ability to spatially photopattern a porous separator onto three dimensional architectures provides a path towards high power on-chip batteries. In summary this dissertation aims to provide perspective in the different directions and progress towards the next generation of rechargeable batteries. From better fundamental insights on complex electrochemical pathways to application-driven materials design and development, this dissertation highlights a few of the challenges, discoveries, and advancements of a much larger research landscape of “next-generation” batteries.

The dissertation of Grace Jeeae Whang is approved.

Amartya Banerjee

Qibing Pei

Laurent Pilon

Bruce S. Dunn, Committee Chair

University of California, Los Angeles

2022

To my family, friends, and mentors.

“Nobody ever figures out what life is all about, and it doesn’t matter. Explore the world. Nearly everything is really interesting if you go into it deeply enough.”

-Richard Feynman

Table of Contents

List of Figures

Chapter 1 Figures

Chapter 2 Figures

Figure 2.1. Voltage vs Capacity graph. A typical GV curve for a two phase lithiation (blue trace) and delithiation (pink trace) reaction is shown. The difference in lithiation and delithiation capacity is reflected in the coulombic efficiency of the cell.

Figure 2.2. C-rate testing protocol. The left graph depicts the current vs time plot which shows a series of constant currents applied to the battery. For higher C-rates, the cell experiences higher currents for a shorter period of time. The graph on the right shows a qualitative graph of a typical C-rate test plot. Slower C-rates (orange trace) typically show lower overpotentials and higher capacities while moving to higher C-rates results in increased overpotentials and reduced capacities.

Figure 2.3. Li plating profile graph. During the plating process, negative current is applied to the working electrode. As the voltage is brought below 0 V vs Li^{+}/Li^{0}, plating becomes favorable and begins with the creation of Li nuclei followed by the subsequent growth of the nuclei.

Figure 2.4. Galvanostatic Linear Polarization (GLP) testing protocol. a) current vs time graph showing a series of small current pulses applied to a symmetric coin cell. b) voltage vs time plot showing overpotential (η) for plating/stripping. c) overpotential vs current plot showing the applied current vs the overpotentials obtained from b). At small currents and small overpotentials, a linear trend should be observed.

Figure 2.5. A typical Butler-Volmer graph is shown above in black. The anodic (blue) and cathodic (red) contributions are shown, and the black trace represents the superposition of the two curves. Upon the application of a positive overpotential, the anodic reaction dominates while under a negative overpotential, the cathodic reaction dominates.

Figure 2.6. Side by side comparison of a galvanostatic charge-discharge curve (left) and the corresponding dQ/dV curve (right).

Chapter 3 Figures

Figure 3.1. Schematic of the fabrication of Li-Sn/Cl composite coatings.

Figure 3.2. (a) Schematic comparing Li plating locations in bare lithium (left) and in a Li-Sn coating system (right) (b) Plan-view SEM image of coating morphology. Scale bar is 10 μm. Photograph of a pristine Li-Sn coating on a stainless steel spacer is shown on top right corner. (c) Lithium-Tin binary phase diagram (d) cryo-FIB cross-sectional SEM image of Li-Sn coating on bulk Li foil. Scale bar is 1 μm.

Figure 3.3. EDX spectral mapping of a pristine coating cross section. Scale bar is 1 μm.

Figure 3.4. (a) Energy Dispersive Spectroscopy (EDS) of the Li-Sn coating showing both tin and chlorine signals and the corresponding atomic percentages. (b) X-ray Diffraction (XRD) pattern of Li-Sn coating (black) along with reference scans for Li_7Sn_3 (blue), and $Li_{13}Sn_5$ (red).

Figure 3.5. HRTEM micrographs of the Li-Sn composite coating. (a) Low-magnification image of composite coating. (b) FFT pattern of the entire region in part a. (c) High-magnification image of the composite coating. (d) Phase distribution schematic overlaying the HRTEM image. The coating contains Li_7Sn_3, $Li_{13}Sn_5$, and amorphous regions.

Figure 3.6 XPS of Cl 2p before and after 15 minutes of Ar^+ etching.

Figure 3.7. (a) Voltage vs. time profile of the galvanostatic linear polarization tests using current densities of 5, 10, 20, 30, 40 and 50 μA cm^{-2} (b) Overpotential vs. current density plot demonstrating a linear trend for low overpotentials along with the corresponding exchange

currents extrapolated from the galvanostatic linear polarization test. (c) Nyquist plot of the Li-Sn coated lithium symmetric cell. The light red trace represents the impedance before the test, the medium red trace represents the impedance during the test, and the dark red trace represents the impedance after the test. (d) Nyquist plot of a lithium control (no coating) symmetric cell which shows a larger initial impedance in addition to large increases throughout the test.

Figure 3.8. Bare lithium plating morphology at 0.1 mA cm^{-2} (left) and 2 mA cm^{-2} (right) for a plating capacity of 4 mAh cm^{-2}.

Figure 3.9. (a) Plan-view SEM of a Li-Sn coated lithium plated at 0.1 mA cm^{-2} for a plating capacity of 4 mAh cm^{-2}. Scale bar is 10 μm (b) Plan-view SEM of a Li-Sn coated lithium plated at 2 mA cm^{-2} for a plating capacity of 4 mAh cm^{-2}. Scale bar is Scale bar is 10 μm (c) Potential profile of Li-Sn coated Li plated at a current density of 0.1 mA cm^{-2} (red) and 2 mA cm^{-2} with the same areal capacity of 4 mAh cm^{-2}. Inset shows a zoom up of the 0.1 mA cm^{-2} plated sample which demonstrated a steady overpotential with less than 1 mV throughout the entire 40 hours.

Figure 3.10. Comparison of Li plating profile for Li-Sn coating and bare lithium control at 0.1 mA cm^{-2}.

Figure 3.11. (a) Graphic representing high plating current density case where lithium is observed to plate on top of the Li-Sn coating (b) Cryo FIB cross-section SEM of Li plated on top of Li-Sn coating at a current density of 2 mA cm^{-2} for a capacity of 1 mAh cm^{-2}. Scale bar is 2 μm. (c)-(f) EDX elemental mapping of the cross-section. Scale bar is 2 μm.

Figure 3.12 Comparison of Everhart Thornley Detector (ETD) (left) and backscattered electron detector (BSED) (right) SEM image for Li plated at 2 mA cm^{-2}. Scale bar 5 μm.

Figure 3.13. (a) Cryo FIB cross-section SEM of Li-Sn coating with lithium plated at a current density of 0.1 mA cm^{-2} for a capacity of 1 mAh cm^{-2}. Plated lithium is outlined in green. Scale bar is 2 μm. (b) Backscattered Electron Detector (BSED) SEM image demonstrated a stark contrast between the plated lithium region and Li-Sn coating while showing similar electron signal between the bulk Li and plated Li. Scale bar is 2 μm. (c) EDX elemental mapping for tin. Scale bar is 2 μm. (d) EDX elemental mapping for chlorine. Scale bar is 2 μm.

Figure 3.14. EDX line of plated lithium at 0.1 mA cm^{-2}. Scale bar of SEM-ETD image (left) and SEM-BSED image (right) is 2 μm.

Figure 3.15. Other region where lithium plated underneath coating demonstrating coating's ability to withstand large volume associated with lithium plating. Sulfur signal from electrolyte. SEM image(top) scale bar is 10 μm. EDX spectral map scale bar is 3 μm.

Chapter 4 Figures

Figure 4.1. Initial lithiation of FeS_2 at various temperatures in 1 M LiFSI $PYR_{14}TFSI$ at a rate of C/20.

Figure 4.2. Initial Lithiation of FeS_2 at 60ºC. a) Open circuit potential (OCP) of the initial lithiation of FeS_2 (open red circles) obtained through GITT of FeS_2 at 60ºC. The colored stars serve as indicators for the points at which XRD and XPS were collected. b) *ex-situ* XRD of the initial lithiation of FeS_2. From top to bottom, the XRD scans show the mid first plateau (~1 mol Li), end of first plateau (1.6 V), mid second plateau, and full discharge (1 V). A pristine FeS_2 electrode (red) and Li_2S (black) powder is provided for reference. Red circles, black squares, and yellow diamonds represent c-FeS_2, Li_2S, aluminum current collector peaks, respectively. The grey shaded region highlights the formation of a nanocrystalline h-FeS which is produced in the first plateau and consumed in the second plateau. **c)** *Ex-situ* XPS of initial lithiation of FeS_2 at mid first

plateau, mid second plateau, and full discharge (1 V). S_T and S_B refer to the terminal and bridging sulfurs, respectively, of lithium polysulfides.

Figure 4.3. *Ex-situ* XRD of initial lithiation of FeS_2 at 100 ºC in 1M LiFSI $PYR_{14}TFSI$ at a C-rate of C/20. Colored circles on the lithiation profile on the right indicate approximate locations for the *ex-situ* XRD scans shown on the left.

Figure 4.4. EXAFS of FeS_2 at 1.6V of the first lithiation fit to the first two coordination shells (Fe-S and Fe-Fe). k3-weighted EXAFS spectrum (black) and fit (red) of h-FeS at 1.6V in **a)** real space and **b)** k space.

Figure 4.5. Comparison of h-FeS:Li_2S (1:1 mol) to FeS_2 and h-FeS. a) Graphic of the ball milling process. Li_2S and h-FeS powder were added in 1:1 mole stoichiometries and mixed at 500 rpm for 5 hours. b) XRD comparison of ball milled h-FeS:Li_2S (1:1 mol) electrode (gray) compared to an FeS_2 electrode lithiated half way into the first plateau (purple). Orange arrows indicate peak positions for h-FeS diffraction peaks. FeS_2 (black) and Li_2S (blue) powder references are provided below. Yellow diamonds represent Al current collector diffraction peaks. c-e) 60ºC initial lithiation (black) and rechargeable galvanostatic profiles (pink) of (c) FeS_2, (d) h-FeS:Li_2S, and (e) h-FeS.

Figure 4.6. Top: XRD of a ball milled (BM) FeS:Li_2S (1:1 mol) electrode (purple) along with the individual h-FeS (green) and Li_2S (blue) powders. Bottom: Comparison of a ball milled composite electrode (purple) with a hand mixed (HM) electrode (black). Li_2S reference shown in blue.

Figure 4.7. Delithiation of FeS_2 at 60ºC. a) Galvanostatic curves of the first lithiation (gray) and delithiation (blue) of FeS_2 cycled at C/20 in 1 M LiFSI PYR14TFSI. Colored stars correspond to key points for ex-situ XRD. Regions I-IV correspond to the Fe redox plateau, Li (de)insertion, Li_2S redox plateau, and Fe_3S_4 conversion regions, respectively. b) ex-situ XRD of initial delithiation of

FeS_2 in addition to a Li_2S reference pattern (black). Black asterisks indicate Fe_3S_4 diffraction peaks. Figure S6 provides an expanded view focusing on the intermediate potentials.

Figure 4.8. Temperature invariance of delithiation conversion potential at ~1.8 V from RT-100 ºC. A C/20 charging rate was used for each temperature.

Figure 4.9. Region I: Iron Redox Plateau at 60 ºC. a) XRD comparison of FeS_2 (blue) and h-FeS (red) electrodes delithiated up to 1.85 V. Yellow diamonds represent aluminum current collector peaks. Black circles represent Li_2S diffraction peaks. b) First lithiation (black) and delithiation (pink) of FeS_2 at 60 ºC cycled at C/20. c) First lithiation (black) and delithiation (pink) of h-FeS at 60 ºC cycled at C/20.

Figure 4.10. a) 60 ºC cycling of FeS at C/20 for 10 cycles in 1M LiFSI $PYR_{14}TFSI$. b) XRD h-FeS charged to 3V for one (light purple) and ten cycles (dark purple). For hexagonal FeS, the charge product on the 1^{st} and 10^{th} cycle is found to best resemble a nanocrystalline tetragonal FeS mackinawite (green circle).

Figure 4.11. Region II: 60 ºC (De)insertion Region Kinetics. a) GITT of the isolated region II [1.6-2.3 V]. Red circles indicate open circuit potential during the rest steps. b) Voltage hysteresis plot of (de)insertion region obtained from the GITT data in part a. c) C-rate testing at C/20 (pink), C/10 (purple), and C/5 (blue) where C is based off of the four-electron redox capacity of FeS_2 (894 mAh g^{-1}). Effective C-rates normalized to capacity of the region II are 0.32 C, 0.64 C, and 1.28 C, respectively. d) dQ/dV plots obtained from c-rate galvanostatic curves in part c. The (de)insertion region features a two peak signature which can be observed at all c rates. e) 1.6-2.3 V cycling data at C/5 (effective c-rate: 1.28 C) for 50 cycles demonstrate excellent cycle stability when cycled within this potential window. f) Energy efficiency of region II as a function of C-rate. Error bars represent the standard deviation taken from 10 cycles for each c-rate.

Figure 4.12. Isolation of the Li (de)insertion region (Region II). Step 1: fully lithiate down to 1 V followed by a partial delithiation up to 2.3 V. Step 2: lithiation/delithiation in between 1.6-2.3 V.

Figure 4.13. GITT of various voltage ranges for FeS_2. Left: 1 – 2.4 V range includes the Region I and Region II. Middle: 1.6 – 2.4 V range captures only Region II. Isolation of this region is shown in Figure 4.12. Right: 1 – 3 V range captures all the reactions. For all three graphs, red circles represent the open circuit potential during the rest periods. GITT tests were performed at room temperature.

Figure 4.14. GITT of the delithiation of FeS_2 at C/20 pulse for 20 minutes followed by a four-hour rest period. The open circuit potential (OCP) is shown by the red circles and the corresponding overpotential (light teal) is extrapolated by taking the difference between the rest potential and C/20 applied current potential (blue circles). The yellow shaded region highlights Region II, the least kinetically limited region.

Figure 4.15. Comparison of the delithiation profile of Li_2S in FeS_2 system (red) vs Li_2S-C composite electrodes.

Figure 4.16. Evidence of S_8 as a Charge Product at 3V via DOL extraction UV-Vis.

A FeS_2 coin cell analyzed after one discharge-charge cycle at 60^{o}C. The coin cell was disassembled and the electrode was left to sit in DOL overnight to extract any soluble and adsorbed polysulfide species. The UV-Vis spectrum of the resulting solution is shown on the right. S_8 signals were detected at ~275 nm.

Figure 4.17. Formation of greigite Fe_3S_4 as a charge product. a) XAS spectra of an FeS_2 electrode charged up to 3 V in comparison to other iron sulfide species (Fe foil, h-FeS powder, c-FeS_2 powder). h-FeS and FeS_2 standards represent Fe^{2+}. The inset shows the first derivative plot. The

3 V sample is slightly shifted to the right of FeS and FeS_2 which can be attributed to the mixed Fe $2^+/3^+$ valence of greigite Fe_3S_4 b) k3-weighted Fe K edge Fourier Transform-EXAFS spectra for an FeS_2 electrode charged up to 3 V (black) along with the modeled fit for Fe_3S_4 (red). Fe_3S_4 structure with colored arrows indicate the Fe-S and Fe-Fe bonds fit in the FT-EXAFS spectra. c) XRD graph at 3 V showing temperature dependence of Fe_3S_4 formation from room temperature to 100 ºC. Broad Fe_3S_4 peaks can be seen starting at 40 ºC and become the dominant phase by 60 ºC. Yellow diamonds indicate Al current collector peaks. d) *ex-situ* XRD of FeS_2 electrodes charged to 3 V under varying conditions at 60 ºC: 1) first cycle (red), 2) third cycle (dark red), and 3) partially lithiated to 1.6 V and subsequently charged to 3 V (lavender). Yellow diamonds indicate Al current collector peaks.

Figure 4.18. Fe K-edge EXAFS spectrum in k-space at 3V (black) alongside fit to Fe_3S_4 standard (red).

Figure 4.19. Loss of Fe_3S_4 upon cycling of FeS_2 at 60ºC. a) FeS_2 cycling at C/20 for 10 cycles. Initial lithiation is outlined in black. b) dQ/dV obtained from the first 5 cycles of the data shown in part a. Focusing on 2.5-2.7V, the loss of Fe_3S_4 within the first 5 cycles is shown by the steady decreasing peak around ~2.6V. c) top: XRD of an FeS_2 electrode after first charge at 3V. Peak positions for Fe_3S_4 diffraction peaks are provided in black (PDF 96-900-0124). bottom: XRD of an FeS_2 electrode after 10 cycles at 3V. Peak positions for t-FeS mackinawite are provided in green (PDF 00-015-0037). Yellow diamonds represent diffraction peaks for the Al current collector.

Figure 4.20. dQ/dV comparison for room temperature and 60 ºC. Fe_3S_4 conversion reactions highlighted in yellow region at 60 ºC are absent at room temperature, where Fe_3S_4 does not form.

Figure 4.21. *Ex-situ* UV-vis spectra of the separated coin cell components (anode, cathode, and separator) soaked in DOL solvent after the (a) first and (b) fifth cycles. After the first charge (3 V)

cycle, the polysulfides are primarily localized near the cathode. However, upon further cycling, the largest polysulfide signals originate from the separator indicative of polysulfide shuttling. Each component was soaked in 4.0 mL of DOL (in separate vials) for 24 h before UV-vis analysis. A blank spectrum of pure DOL was used for background subtraction in all cases. S_8 and S_4^{2-} signals were observed at ~275 and ~300 nm, respectively.[7] For graph b, the cathode signal overlaps with the anode (red).

Figure 4.22. XRD comparison of the 1st charge (light purple) and 10th charge (dark purple) cycle at room temperature. t-FeS mackinawite diffraction peaks are shown in green. Orange diamonds indicate Al current collector peaks.

Figure 4.23. a) FeS_2 cycle stability test at 60 ºC for a) 1-3 V window and b) 1-2.42 V window. For both a) and b), the first cycle (pink) was conducted at C/20 while the subsequent cycles were cycled at C/5 (purple, blue, green). Specific capacity as a function of cycle number for c) 1-3 V and d) 1-2.42 V. For both c) and d), the coulombic efficiency is shown in yellow.

Figure 4.24. Electrochemical Performance of FeS_2 in 1M LiFSI $PYR_{14}TFSI$ at 60 ºC. a) C-rate testing for FeS_2. b) FeS_2 cycle stability test. The first cycle (pink) was conducted at C/20 and then subsequently cycled at C/5 for a total of 100 cycles. c) Specific capacity as a function of cycle number from data shown in b). Coulombic efficiency is shown in yellow.

Chapter 5 Figures

Figure 5.1. a) Process flow for fabricating porous SU-8 separators: 1) spin coating of the [EMI][TFSI]/SU-8 solution 2) a pre bake at 100 °C 3) UV exposure 4) a post-bake at 100 °C 5) acetone solvent exchange to remove the [EMI][TFSI] from the porous SU-8 matrix 6) CO_2 supercritical drying to preserve microstructure. b) SEM of a photopatterned circle array on a silicon wafer using a 50 wt% [EMI][TFSI] SU-8 solution. The diameter of each circle is 100 µm. c-

f) EDX spectral maps showing that the [EMI][TFSI] is locally confined in the polymerized SU-8 matrix.

Figure 5.2. Photograph of SU-8/[EMI][TFSI] films after 10 minute post exposure bake at 100 ℃ as a function of [EMI][TFSI] wt%.

Figure 5.3. a) FTIR of a 50 wt% [EMI][TFSI]/SU-8 film before and after ionic liquid removal. Upon removal of ionic liquid, the absorbance bands of the TFSI anions (red dashed lines) disappear indicating the complete removal of ionic liquid from the porous SU-8 matrix. b-c) SEM image of porous separator (b) before (c) and after ionic liquid removal. Upon acetone solvent exchange and CO_2 supercritical drying, the porous SU-8 network is revealed. The scale bar is 10 μm. d) EDX of Figure 5.3c shows that the ionic liquid is completely removed (absence of fluorine and sulfur signals) and only the carbon and oxygen signals from the SU-8 matrix remain. Si signals are from the substrate and Au signals are from sputtering to minimize charging from the electron beam. e) Elastic modulus of neat SU-8, 50 wt% [EMI][TFSI] porous separator, polypropylene (PP), and Polytetrafluoroethylene (PTFE) separators measured using nanoindentation. f) TGA profiles for a 50 wt% [EMI][TFSI] porous separator and a bulk SU-8 control. The porous separator can withstand temperatures up to 219 °C with only 5% weight loss.

Figure 5.4. Cross Section SEM of [EMI][TFSI]/SU-8 ionogel as a function of [EMI][TFSI] wt% a) 30 wt% [EMI][TFSI] b) 40 wt% [EMI][TFSI] c) 50 wt% [EMI][TFSI] d) 60 wt% [EMI][TFSI]. At 60 wt% the [EMI][TFSI] is the dominant phase and the smooth morphology is attributed to the ionic liquid phase. Scale bar for each image is 30 μm. Spin coat speed is 3000 rpm. The thicknesses of the 30-60 wt% [EMI][TFSI] samples are 9.91 ± 0.13 μm , 9.12 ± 0.10 μm, 7.69 ± 0.13 μm, and 5.71 ± 0.15 μm, respectively.

Figure 5.5. Plan view SEM of a) 40 b) 50 and c) 60 wt% [EMIM][TFSI] samples spin coated onto a silicon wafer. Scale bar is 3 μm. d-f) Contact angle measurements using water as the solvent

for 40, 50, and 60 wt% [EMIM][TFSI] porous SU-8 samples demonstrating the hydrophobic property of SU-8. The contact angle increases with increasing porosity. g-i) Contact angle measurements using propylene carbonate (PC), the electrolyte solvent used in electrochemical testing, for 40, 50, and 60 wt% [EMIM][TFSI], respectively.

Figure 5.6. Pore size distribution analysis of (a-c) 40 wt%, (b-f) 50 wt%, and (g-i) 60 wt% [EMI][TFSI] porous separators. SEM images of the porous separators are shown in (a,d,g) while the corresponding pore size analysis images are shown in (b,e,h). The pore size distributions are shown in (c,f,i). The average pore sizes for 40, 50 and 60 wt% [EMI][TFSI] were approximately 33, 116, and 287 nm, respectively. The image analysis computes the local thickness of the SEM images by evaluating the diameter of the largest sphere that fits inside the pore and contains the voxel. The number of voxels with respective local thickness values and the corresponding pore sizes were then obtained.

Figure 5.7. Spin coater speed vs film thickness for 50 wt% [EMI][TFSI]. The thickness of the photopatternable separator can be tuned as a function of spin coating speed. Moreover, it is possible to obtain thinner films by further diluting the SU-8 prepolymer solution in cyclopentanone, while thicker films can be obtained by using a higher viscosity SU-8 photoresist, such as SU-8 3050. Error bars correspond to the standard deviation across 5 samples.

Figure 5.8. a) Impedance spectra for glass fiber separator and porous SU-8 separator saturated with a liquid electrolyte (1 M $LiClO_4$ in PC) along with the corresponding equivalent circuit. Inset: Expanded view of the impedance spectra showing the high frequency Z' intercept. b) Galvanostatic measurements of the amorphous Si thin film half cell showing lithiation and delithiation at C/5 (5 μA cm^{-2}). Similar galvanostatic profiles are obtained for both the SU-8 porous separator and glass fiber separator. c) Specific capacity and coulombic efficiency of the amorphous Si/porous SU-8/Li metal and amorphous Si/ Glass fiber/Li metal coin cells cycled at a

C/5 rate for 25 cycles. d) Charge-discharge characteristics for the full cell of amorphous Si|porous separator|LFP cycled at C/5 (5 μA cm^{-2}) for 25 cycles. e) Areal charge/discharge capacities and coulombic efficiency for 25 cycles for the full cell shown in (d) above. A charge is defined as the delithiation of LFP and lithiation of the Si.

Figure 5.9. Cyclic voltammogram of a-Si thin film cycled at 0.1 mV s^{-1} using a glass fiber separator in 1M $LiClO_4$. Beyond the initial cycle, the a-Si demonstrates good reversibility shown by the similar CV curves for cycle 2 & 3. The areal capacity used in this study was obtained by integrating current (mA) vs time (hr) plot for the second cycle (~25 μAh cm^{-2}).

Figure 5.10. CV of an amorphous silicon thin film with a 50 wt% [EMI][TFSI] photopolymerized porous separator coin cell with lithium metal counter electrode. Lithium metal is in direct contact with the porous separator. Scan rate is 0.1 mV/s.

Figure 5.11. CV of an LFP electrode with a 50 wt% [EMI][TFSI] photopolymerized porous separator in 3 electrode experiment with lithium counter and reference electrode at a scan rate of 0.1 mV/s.

Figure 5.12. SEM images of (a) bare silicon array and (b) silicon array coated with the [EMIM][TFSI] modified photopatternable SU-8 electrolyte. Each silicon post represents 100 μm diameter with 150 μm in height and 15 μm thick SU-8 layer. Inset in (b) shows close up of the conformal separator on the Si post after photopatterning. Scale bar for the inset image is 100 μm. c) Expanded view of the highly porous surface once the ionic liquid has been removed. The scale bar is 50 μm. d) Galvanostatic profile of the separator coated 3D silicon array with a lithium counter and reference electrode and 1M $LiClO_4$ in propylene carbonate as an electrolyte. e) Comparison plot of the coulombic efficiency of silicon post arrays with and without porous separator coating.

Figure 5.13. Two-part exposure process for patterning conformal separators for Si post array. To conformally coat the separator on the 3D Si post, a two part exposure process was employed. The first step consists of forming a base layer to cover the bottom layer (left) followed by the second step in which the side walls and top of the posts are patterned (right).

List of Tables

Acknowledgements

I came to UCLA in 2017 with the intent of getting a Masters degree. Almost 5 years later and no Masters degree in hand, I write this doctoral dissertation. Through a combination of opportunity, luck, and most importantly, the generosity of Professor Dunn, I've been fortunate enough to end up in this position. Without him, none of this research would exist. His constant support, guidance, and positive morale sets the tone for the lab while his enthusiasm for good science, humor, and humility are qualities that are appreciated by many. With his support and encouragement, I've grown to be a more independent and creative scientist. He has shown me what a difference a good advisor and lab can have on a person's academic journey and growth.

To my lab mates who have made my day-to-day life in Dunn Lab always fun and full of surprises, not a day has gone by where there wasn't laughter and that's a wonderful position to be in. I would like to thank those who came before me: Dr. Chun-Han (Matt) Lai, Dr. Jonathan Lau, Dr. David Ashby, Dr. Ryan DeBlock, Dr. Christopher Choi, and Dr. Danielle Butts. David, thank you for your patience and help throughout grad school- I'm glad that we got to work on projects even after your time in grad school. Going to the gym with Chris and you have made for some memorable moments. To Danielle, thank you for always making yourself available to discuss all things that confused me and us. Your kindness, intelligence, and willingness to help is appreciated along with your great Netflix recommendations. Chris, thank you for taking me under your wing and teaching me e-chem in the lab and photolithography in the clean room. You have taught me so much within our overlapping time and I am truly grateful to have you as a lab mate and friend. And of course, I'd like to thank those who I still have the pleasure of seeing every day: Patricia McNeil, Alexander Cheikh, Maggie Fox, Yunkai Luo, Bintao Hu, Randy Chen, Jacky Yu, and Makena White. Thank you all for always keeping things interesting and providing me with my daily dose of comedic relief. I'd also like to give a special thanks to Dr. Esther Lan whose contagious positivity and kindness has shaped our lab culture- I really enjoyed our conversations

and lunchtime seminars. And to my wonderful PhD committee, thank you all for your time, helpful questions, and feedback that helped shaped some of the work presented in this dissertation.

Even before grad school, I have been fortunate to have had the support of great mentors who have inspired me in my path towards science and engineering: Lina Garcia (5th grade teacher), Tobin Brannon (AP Bio teacher), and Clay Carrier (undergrad internship mentor). All of you have certainly shown me the profound impact that good mentors can have on someone's life. In all the different stages of my life, I've been blessed with having mentors who lifted me up with their encouragements.

To my amazing friends who made my graduate school years outside of the lab always interesting and fun (Ari C., Braden P., Taylor S., Arpita I., Michael K., John N., Benaisha P., Sammi C., Mitch N., Rohan R., Lyra K., Chad C., & Will N.), thank you for always providing some much-needed perspective in life.

Lastly, I'd like to thank my family. A PhD is a challenging and interesting time in someone's life. While I devoted countless hours in the research presented here, I truly couldn't have done it without the emotional support and love of my family who stood by me every step of the way. To my mom and dad (Cindy and Steve), thank you for always supporting my decisions in addition to all the quirky interests and hobbies I've picked up along the way. Both of you have shown me the importance of resilience and working hard- I hope this piece of paper is proof of it. I love you both. To my sister Diana, one of the greatest blessings in life has been having you as my sister. Although we are cut from the same cloth, I cannot name someone more different than me. Despite being different people, to this day, you are the one who understands me the best.

All of this is to say, yes, I've done the work and put in the time, but I could not have done it alone. And I'm eternally grateful for you all.

Chapter 3 is a modified version of the published work:

Whang, G.; Yan, Q.; Li, D.; Wei, Z.; Butts, D.; Sautet, P.; Luo, J.; Dunn, B. Avoiding Dendrite Formation by Confining Lithium Deposition underneath Li–Sn Coatings. J. Mater. Res. 2021, 36 (4), 797–811.

Chapter 4 is a modified version of the published work:

Whang, G.; Ashby, D. S.; Lapp, A. S.; Hsieh, Y.-C.; Butts, D. M.; Kolesnichenko, I. V; Wu, P.-W.; Lambert, T. N.; Talin, A. A.; Dunn, B. S. Temperature-Dependent Reaction Pathways in FeS2: Reversibility and the Electrochemical Formation of Fe3S4. Chem. Mater. 2022.

Chapter 5 is a modified version of the published work:

Choi, C. S*.; Whang, G. J*.; McNeil, P. E.; Dunn, B. S. Photopatternable Porous Separators for Micro-Electrochemical Energy Storage Systems. Adv. Mater. 2022, 34 (9), 2108792.

Vita

2013	B.S. in Nanoengineering
	University of California, San Diego
	Magna Cum Laude
	Outstanding Graduating Senior Departmental Awardee
2017 – 2022	Graduate Student Researcher
	Department of Materials Science and Engineering
	University of California, Los Angeles

Publications

15. **G. Whang**, D. S. Ashby, A. S. Lapp, Y.-C. Hsieh, D. M. Butts, I. V Kolesnichenko, P.-W. Wu, T. N. Lambert, A. A. Talin, and B. S. Dunn: Temperature-Dependent Reaction Pathways in FeS 2 : Reversibility and the Electrochemical Formation of Fe 3 S 4. *Chem. Mater.* (2022).

14. D. S. Ashby, J. S. Horner, **G. Whang**, A. S. Lapp, S. A. Roberts, B. Dunn, I. V Kolesnichenko, T. N. Lambert, and A. A. Talin: Understanding the Electrochemical Performance of FeS 2 Conversion Cathodes. *ACS Appl. Mater. Interfaces* (2022).

13. A. S. Lapp, **G. Whang**, A. Bhandarkar, I. V. Kolesnichenko, B. S. Dunn, T. N. Lambert, and A. A. Talin: In Situ UV–Vis Analysis of Polysulfide Shuttling in Ionic Liquid-Based Li-FeS 2 Batteries. *J. Phys. Chem. C* **126**(11), 5101 (2022).

12. C. S. Choi*, **G. J. Whang***, P. E. McNeil, and B. S. Dunn: Photopatternable Porous Separators for Micro-Electrochemical Energy Storage Systems. *Adv. Mater.* **34**(9) (2022).

11. E. Le Calvez, J. C. Espinosa-Angeles, **G. J. Whang**, N. Dupré, B. S. Dunn, O. Crosnier, and T. Brousse: Investigating the Perovskite Ag1-3xLaxNbO3 as a High-Rate Negative Electrode for Li-Ion Batteries. *Front. Chem.* **10**(April), 1 (2022).

10. Q. Yan, S. T. Ko, A. Dawson, D. Agyeman-Budu, **G. Whang**, Y. Zhao, M. Qin, B. S. Dunn, J. Nelson Weker, S. H. Tolbert, and J. Luo: Thermodynamics-driven interfacial engineering of alloy-type anode materials. *Cell Reports Phys. Sci.* **3**(1), 100694 (2022).

9. **G. Whang**, Q. Yan, D. Li, Z. Wei, D. Butts, P. Sautet, J. Luo, and B. Dunn: Avoiding dendrite formation by confining lithium deposition underneath Li–Sn coatings. *J. Mater. Res.* **36**(4), 797 (2021).

8. J. S. Horner, **G. Whang**, D. S. Ashby, I. V. Kolesnichenko, T. N. Lambert, B. S. Dunn, A. A. Talin, and S. A. Roberts: Electrochemical Modeling of GITT Measurements for Improved Solid-State Diffusion Coefficient Evaluation. *ACS Appl. Energy Mater.* **4**(10), 11460 (2021).

7. C. Choi, K. Robert, **G. Whang**, P. Roussel, C. Lethien, and B. Dunn: Photopatternable hydroxide ion electrolyte for solid-state micro-supercapacitors. *Joule* **5**(9), 2466 (2021).

6. R. H. Deblock, Q. Wei, D. S. Ashby, D. M. Butts, **G. J. Whang**, C. S. Choi, and B. S. Dunn: Siloxane-Modified, Silica-Based Ionogel as a Pseudosolid Electrolyte for Sodium-Ion Batteries. *ACS Appl. Energy Mater.* **4**(1), 154 (2021).

5. A. Likitchatchawankun, R. H. DeBlock, **G. Whang**, O. Munteshari, M. Frajnkovič, B. S. Dunn, and L. Pilon: Heat generation in electric double layer capacitors with neat and diluted ionic liquid electrolytes under large potential window between 5 and 80 °C. *J. Power Sources* **488**(August 2020), 229368 (2021).

4. Q. Yan*, G. **Whang***, Z. Wei, S.-T. Ko, P. Sautet, S. H. Tolbert, B. S. Dunn, and J. Luo: A Perspective on interfacial engineering of lithium metal anodes and beyond. *Appl. Phys. Lett.* **117**(8), 080504 (2020).

3. Q. Yan, S. T. Ko, Y. Zhao, **G. Whang**, A. Dawson, S. H. Tolbert, B. S. Dunn, and J. Luo: Cryogenic milling method to fabricate nanostructured anodes. *ACS Appl. Energy Mater.* **3**(11), 11285 (2020).

2. A. Likitchatchawankun, **G. Whang**, J. Lau, O. Munteshari, B. Dunn, and L. Pilon: Effect of temperature on irreversible and reversible heat generation rates in ionic liquid-based electric double layer capacitors. *Electrochim. Acta* **338**, 135802 (2020).

1. O. Munteshari, A. Borenstein, R. H. DeBlock, J. Lau, **G. Whang**, Y. Zhou, A. Likitchatchawankun, R. B. Kaner, B. Dunn, and L. Pilon: In Operando Calorimetric Measurements for Activated Carbon Electrodes in Ionic Liquid Electrolytes under Large Potential Windows. *ChemSusChem* **13**(5), 1013 (2020).

* co-first author

Conferences/Presentations

Grace Whang. Electrochemical Insights on Next Generation High Energy Density Batteries. *WiscProf Workshop*. Madison, WI. May 2022.

Grace Whang, David Ashby,Aliya Lapp, A. Talin, Bruce Dunn. New Insights on Reaction Pathways for FeS_2 Cathodes. *Materials Research Society Spring 2022 Meetin*g. Honolulu, HI. May 2022.

Grace Whang, Qizhang Yan, Jian Luo, Bruce Dunn. Lithium Deposition Underneath Interfacial Coating Layers. *Materials Research Society Fall 2020 Meeting*. November 2020.

Grace Whang, David Ashby, Alec Talin, Bruce Dunn. A multi-faceted investigation of FeS2 in ionic liquid/ionogel systems. Sandia Grand Challenge External Advisory Board Meeting. January 2021.

Chapter 1. Introduction and Motivation

In this Chapter, the two different types of “next generation” batteries relevant to this dissertation are introduced. The first involves moving beyond intercalation chemistries to realize high energy batteries while the second focuses on the development of on-chip batteries to power IoT technologies.

Chapter 1.1 Next Generation High Energy Density Batteries

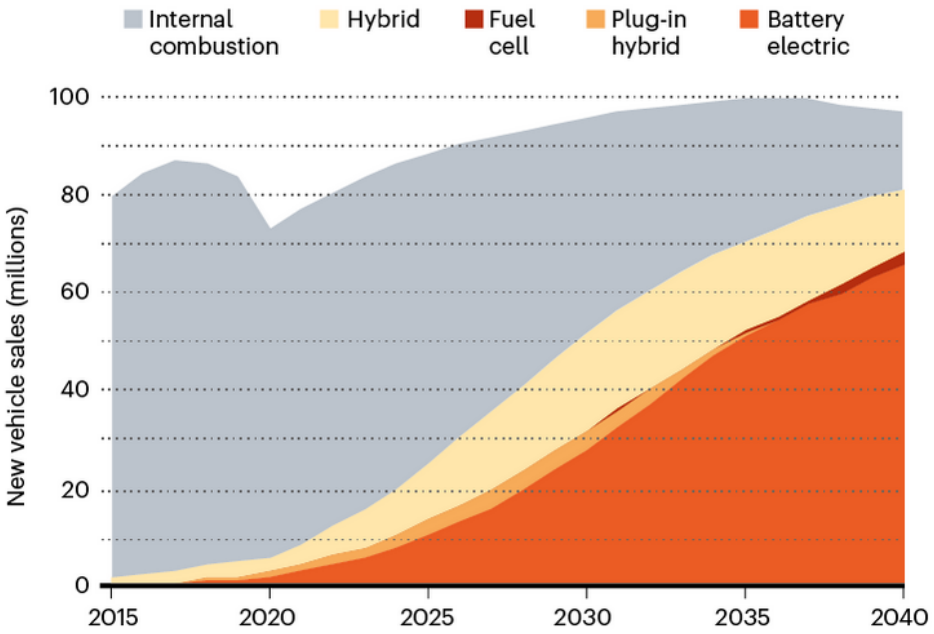

Figure 1.1. Forecast of worldwide vehicle sales. Electric vehicles are projected to rapidly rise to account for half the sales by 2035. Figure reproduced from ref [1].

“Rocking chair” intercalation Li-ion chemistries have revolutionized portable electronics through the commercialization of rechargeable batteries that provide reasonable energy densities and high cyclability (>1000 cycles). While its discovery has been awarded the Nobel Prize in Chemistry in 2019, the journey towards higher energy density batteries is far from mature. The

rapid rise of electric vehicle industry (Figure 1.1) combined with net zero carbon emissions by 2050 in the US and EU[1,2] have paved way for a new era of battery research in search of high energy density batteries. From a materials perspective, energy density can be broken down into two key requirements: 1) the material must possess high specific capacity translating to how much charge can be stored per mass and 2) allow for a large voltage window between the cathode and anode, whereby a cathode should possess a high redox potential and the anode should possess a low redox potential (Eqn. 1.1).

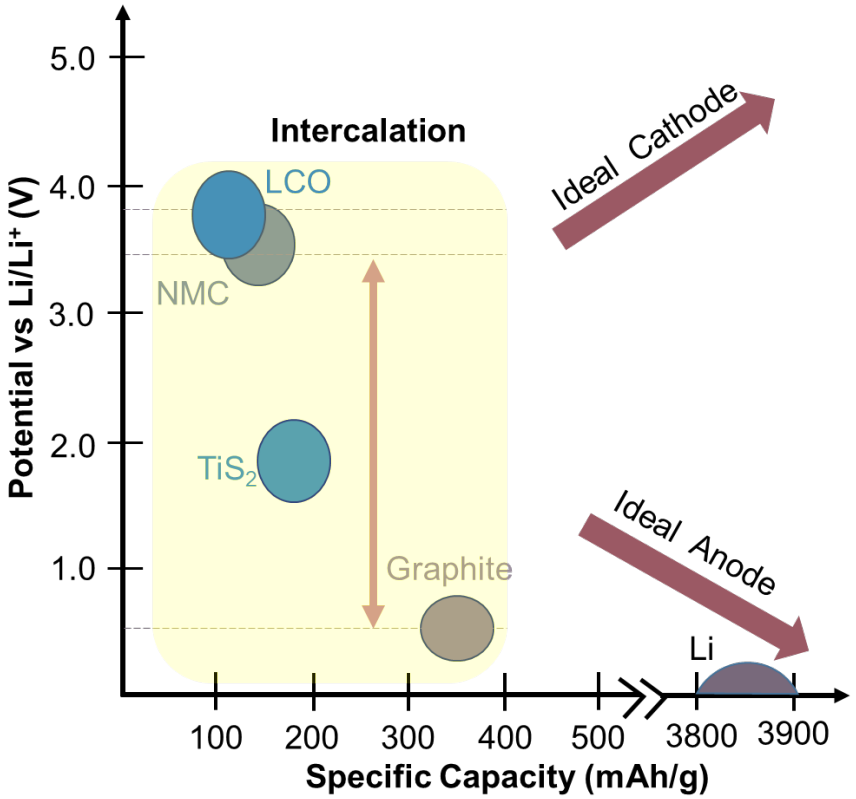

Figure 1.2. Potential vs Specific Capacity Plot. Commercial intercalation cathodes and anodes are shown in the yellow box. Due to their lower specific capacities (<200 mAh/g), they are unable to provide higher energy density batteries (>500 Wh/kg). Mauve arrows point towards ideal properties for high energy density anodes and cathodes.

Figure 1.2 graphically shows the redox potential and capacity of common intercalation compounds. While reasonably large voltage windows can be achieved, the specific capacity of intercalation compounds is typically limited (<200 mAh g^{-1}). Therefore, next generation high energy density batteries must look beyond intercalation chemistries and other charge storage mechanisms such as conversion reactions and Li plating which will be discussed in a later section.

$$E = C \times V \qquad \text{Eqn. 1.1}$$

where E= Energy Density (Wh/g)

C= Specific Capacity (mAh/g)

V= Voltage window (V)

Lastly, while specific capacity and voltage window determine the energy density, other important factors such as cycle stability, power, toxicity, cost, and sustainability provide other constraints in developing a blueprint for next generation high energy density batteries. Therefore, the development of high energy density next generation batteries is a multi-faceted challenge and while the requirements are clear, the path to get there is less so. The current research landscape can be divided in two primary directions. On one end is the pursuit of developing new high specific capacity materials that can provide lower (for anodes) and higher (for cathodes) redox potentials; on the other, a revival of existing materials through new approaches to address the known challenges and fundamental reaction pathways to produce more targeted approaches for improvements. The work presented here aims to address the latter by revisiting: 1) the challenging lithium metal interface and 2) the complex and debated iron disulfide lithiation pathways for primary and secondary batteries.

Chapter 1.1.1. Mechanisms of Charge Storage

In order to under how to increase the specific capacity, it is important to first understand what governs the specific capacity of a material in addition to the mechanisms by which charge can be stored. Specific capacity is determined by 1) the number of electrons (n) the material can undergo redox and 2) the molecular weight of the material (MW) as shown in Eqn. 1.2. Therefore, an ideal candidate would be a light-weight material that undergoes multielectron redox.

$$C\ [mAh\ g^{-1}] = \frac{n\ F}{3.6\ MW} \qquad \text{Eqn. 1.2}$$

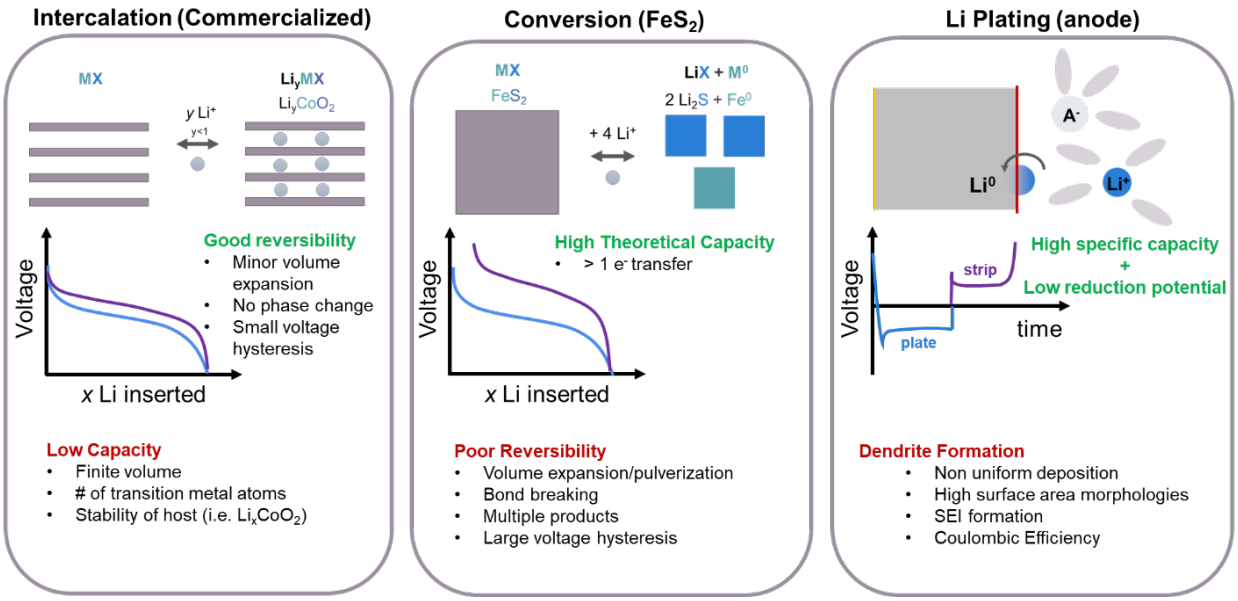

Figure 1.3. Mechanisms of charge storage. The left box shows commercialized intercalation reactions while the middle and right box focus on conversion and plating redox reactions, respectively.

While commercialized intercalation electrodes offer great reversibility resulting in excellent cycle life, their capacities remain limited. Specific capacity for intercalation materials is limited by the number of transition metals (redox active element) and the structural stability of the host upon

lithium removal. Generally, intercalation compounds are limited to ≤1 electron redox per transition metal.[5] In order to increase the numbers of electrons undergoing redox, and thus capacity, other charge storage mechanisms are better suited. Figure 1.3 provides a comparison between the different mechanisms of charge storage relevant to this dissertation.

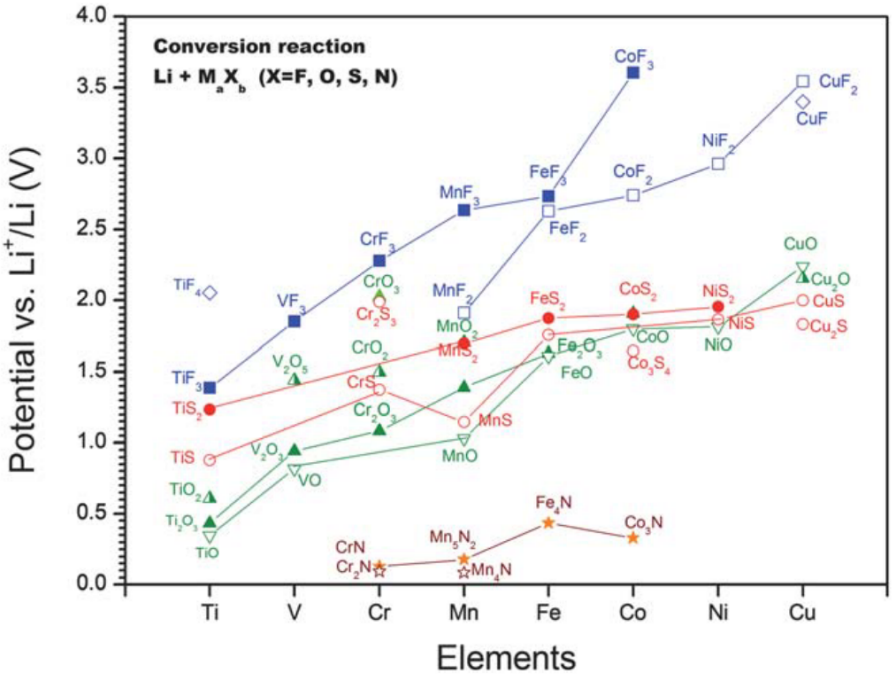

Figure 1.4. Survey of various binary transition metal conversion compounds for Li. Calculated electromotive force (emf) values are shown for each. Figure reproduced from [3].

Conversion chemistries (i.e. FeS_2) typically undergo multi electron redox reactions (n=4 for FeS_2) resulting in high theoretical capacities (894 mAh/g for FeS_2). For conversion reactions, lithiation of the active material results in the breaking of bonds to form a completely different set of products.[4] In the case of FeS_2, upon its four electron lithiation reaction, Fe^0 and Li_2S are formed as the discharge products. While multi-electron redox is a highly attractive characteristic of conversion chemistries, there are challenges such as large volume changes, pulverization of the

material, and large voltage hysteresis that need to be addressed.[5,6] Figure 1.4 shows various binary transition metal compounds known to undergo conversion reactions with Li along with their calculated cell potential.

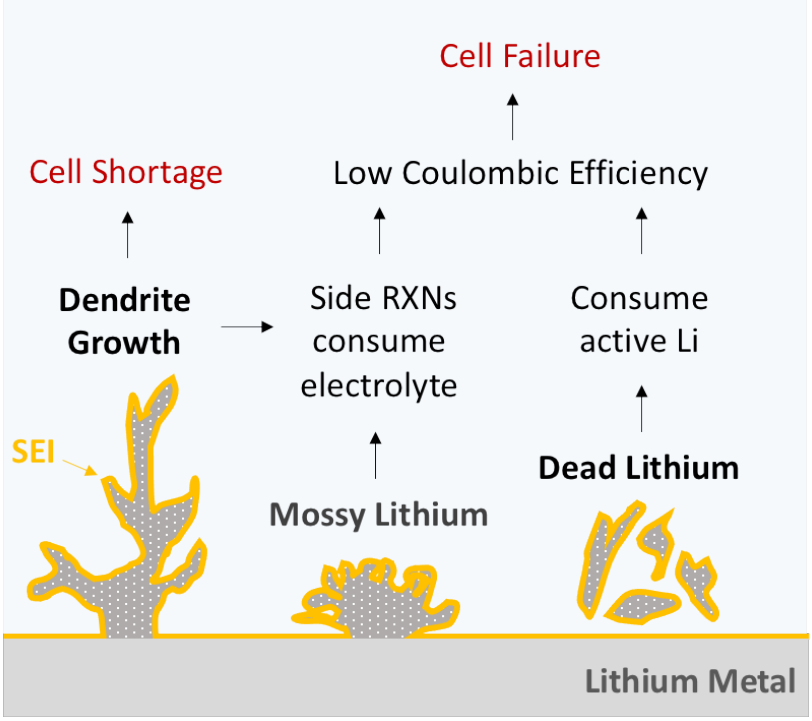

Figure 1.5. Graphic depicting the various challenges with the Li metal anodes. Figure reproduced from.[7]

Beyond intercalation and conversion reactions, lithium plating is a mechanism of charge storage for a Li battery anode (Figure 1.3). Lithium metal batteries have been studied since the first demonstration of a working rechargeable Li-TiS_2 battery by Nobel Prize Laureate Stan Whittingham in the 1970s. From a theoretical standpoint, Li metal is an obvious choice as an anode due to its light mass reflected in its high specific capacity (3860 mAh g^{-1}) in addition its low redox potential (-3.04 vs S.H.E./ 0 V vs Li^+/Li^0). Li plating/stripping is also a host-less process and does not require a host material unlike intercalation reactions and thus is not limited to certain

volume or number of transition metals present to undergo redox. The Li-ions themselves are the redox active species. Li-ions in the electrolyte are adsorbed onto a conductive substrate which can provide an electron to reduce the Li-ion into Li metal under the application of an external current. Li metal batteries and “Li-free” batteries both rely on Li plating/stripping reactions. The largest impediment to the use of Li metal anode in rechargeable batteries revolves around safety and more specifically the challenge of Li dendrites (Figure 1.5). Chapter 3 of this dissertation revisits the challenges of lithium dendrites from the lens of interfacial coating layers. By confining deposition of Li underneath the coating, Li dendrite formation at the surface can be mitigated.

Chapter 1.2 Next Generation On-Chip Batteries for IoT Devices

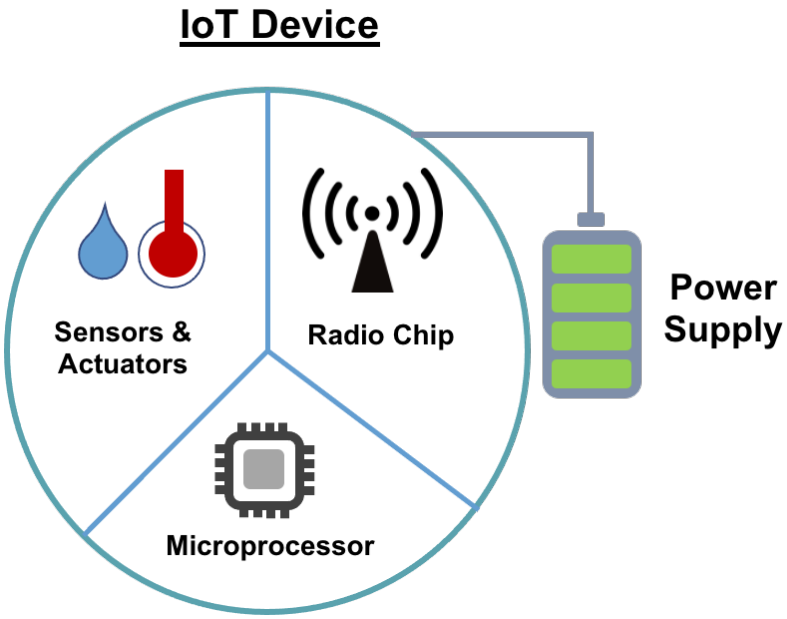

Figure 1.6. Components of an IoT device. IoT devices typically include: 1) sensors and/or motors that collect data or perform an action, 2) a microprocessor that will take in data and process it, 3) a Bluetooth chip or communication protocol that will exchange data to and from the device, and 4) a power supply that provides external power to the device.

The second part of this dissertation focuses on a different kind of “next generation” battery, namely that of small batteries driven by the rapid miniaturization of devices and the Internet of Things technologies. Internet of things (IoT) refers to a network of “things” or objects that are embedded with sensors, processors, and connected to other devices through the internet which allows for information exchange across devices.[8] One major area of IoT devices is wearable electronics and while there has been a huge push towards further scaling down the size, the battery remains the bottleneck.[9] Additionally, while most of the components (sensors, Bluetooth chip, microprocessor, etc) are embedded onto the device, the battery remains as an external component of the device (Figure 1.6). To bridge the gap between small devices and power sources, the integration of the power source to the device as an on-chip battery is a promising approach (Figure 1.7).

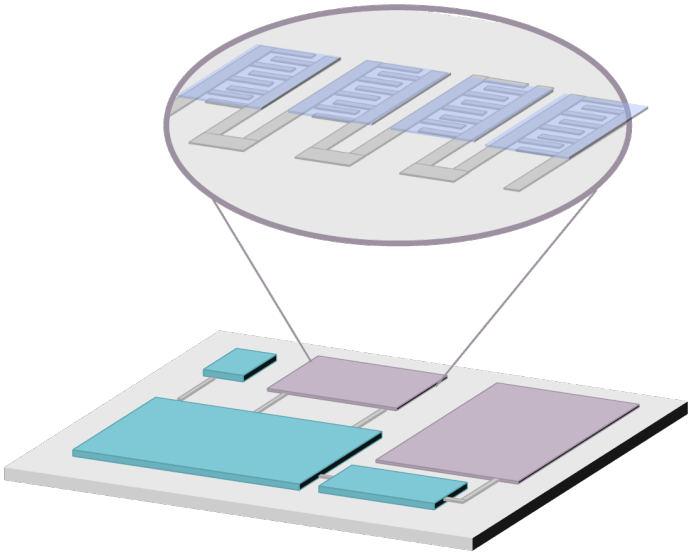

Figure 1.7. Graphic of an embedded on-chip battery.

In the case of next generation on-chip batteries, many opportunities revolve around development of new materials and processes suitable and adaptable with the same technologies used to make the devices and chips themselves. Using photolithography and semiconductor processing to fabricate battery components with high spatial resolution and control, an on-chip

battery is a promising avenue to achieve both high energy and high power through three dimensional micromachined architectures.[10,11]

For an on-chip battery system, ion transport between the electrodes can be a limitation, in particular for high power applications due to the lower ionic conductivities of existing solid-state electrolytes. Table 1.1 presents the ionic conductivity of various electrolytes. While the photopatternable, SU-8 photoresist-based solid electrolyte offers the spatial control required for on-chip batteries, the ionic conductivity remains a few orders of magnitude lower compared to liquid electrolytes (Table 1.1). To bridge the gap between photopatternability and ionic conductivity, a photopatternable porous separator is explored in Chapter 5. That is, rather than using the photoresist as a solid-state electrolyte, introducing porosity into the photopatternable polymer could serve as separator which can spatially confine high ionic conductivity liquid electrolytes. The ability to photopattern a conformal separator with high-resolution photopatternability provides a basis for achieving high energy and high power micro electrochemical energy storage devices.

Table 1.1. Ionic conductivities of various electrolytes

Electrolyte	Ionic Conductivity [S cm^{-1}]	Photopatternable?	Ref
0.2M $LiClO_4$ in SU-8	**5.2×10^{-5}**	**yes**	12
$LiClO_4$-PEO	**~$1\text{-}10 \times 10^{-4}$**	**no**	13
LiTFSI-PMMA	**~2×10^{-3}**	**no**	14
Liquid Electrolyte	**~$1\text{-}10 \times 10^{-3}$**	**no**	15

Chapter 1.3 References

(1) Castelvecchi, D. Electric Cars and Batteries: How Will the World Produce Enough? *Nature* **2021**, *596* (7872), 336–339. https://doi.org/10.1038/d41586-021-02222-1.

(2) IEA. *Net Zero by 2050: A Roadmap for the Global Energy Sector*; 2021.

(3) Zu, C.; Li, H. Thermodynamic Analysis on Energy Densities of Batteries. *Energy Environ. Sci.* **2011**, 2614–2624. https://doi.org/0.1039/c0ee00777c.

(4) Cabana, J.; Monconduit, L.; Larcher, D.; Palacín, M. R. Beyond Intercalation-Based Li-Ion Batteries: The State of the Art and Challenges of Electrode Materials Reacting through Conversion Reactions. *Adv. Mater.* **2010**, *22* (35), 170–192. https://doi.org/10.1002/adma.201000717.

(5) Ashby, D. S.; Horner, J. S.; Whang, G.; Lapp, A. S.; Roberts, S. A.; Dunn, B.; Kolesnichenko, I. V; Lambert, T. N.; Talin, A. A. Understanding the Electrochemical Performance of FeS 2 Conversion Cathodes. *ACS Appl. Mater. Interfaces* **2022**. https://doi.org/10.1021/acsami.2c01021.

(6) Whang, G.; Ashby, D. S.; Lapp, A. S.; Hsieh, Y.-C.; Butts, D. M.; Kolesnichenko, I. V; Wu, P.-W.; Lambert, T. N.; Talin, A. A.; Dunn, B. S. Temperature-Dependent Reaction Pathways in FeS 2 : Reversibility and the Electrochemical Formation of Fe 3 S 4. *Chem. Mater.* **2022**. https://doi.org/10.1021/acs.chemmater.2c00291.

(7) Yan, Q.; Whang, G.; Wei, Z.; Ko, S. T.; Sautet, P.; Tolbert, S. H.; Dunn, B. S.; Luo, J. A Perspective on Interfacial Engineering of Lithium Metal Anodes and Beyond. *Appl. Phys. Lett.* **2020**, *117* (8). https://doi.org/10.1063/5.0018417.

(8) Li, S.; Xu, L. Da; Zhao, S. The Internet of Things : A Survey. *Inf. Syst. Front.* **2015**, No. April 2014, 243–259. https://doi.org/10.1007/s10796-014-9492-7.

(9) UL LLC. *Testing Battery Systems Designed for Wearable Technologies*; 2015.

(10) Hur, J. I.; Smith, L. C.; Dunn, B. High Areal Energy Density 3D Lithium-Ion Microbatteries.

Joule **2018**, *2* (6), 1187–1201. https://doi.org/10.1016/j.joule.2018.04.002.

(11) Long, J. W.; Dunn, B.; Rolison, D. R.; White, H. S. 3D Architectures for Batteries and Electrodes. *Adv. Energy Mater.* **2020**. https://doi.org/10.1002/aenm.202002457.

(12) Choi, C. S.; Lau, J.; Hur, J.; Smith, L.; Wang, C.; Dunn, B. Synthesis and Properties of a Photopatternable Lithium-Ion Conducting Solid Electrolyte. *Adv. Mater.* **2018**, *30* (1), 1703772. https://doi.org/10.1002/adma.201703772.

(13) Das, S.; Ghosh, A. Ionic Conductivity and Dielectric Permittivity of PEO-LiClO 4 Solid Polymer Electrolyte Plasticized with Propylene Carbonate. *AIP Adv.* **2015**, *027125*. https://doi.org/10.1063/1.4913320.

(14) Kufian, M. Z.; Ramesh, S.; Arof, A. K. PMMA-LiTFSI Based Gel Polymer Electrolyte for Lithium-Oxygen Cell Application. *Opt. Mater. (Amst).* **2021**, *120* (July), 111418. https://doi.org/10.1016/j.optmat.2021.111418.

(15) Xu, K. Nonaqueous Liquid Electrolytes for Lithium-Based Rechargeable Batteries. *Chem. Rev.* **2004**, *104* (10), 4303–4417. https://doi.org/10.1021/cr030203g.

Chapter 2. Electrochemical Techniques

This chapter provides a brief background on some of the electrochemical techniques used throughout this dissertation. If the reader is looking for a more in depth and complete discussion of electrochemical methods and techniques, the reader should refer to "Electrochemical Methods: Fundamentals and Applications" by Allen Bard and Larry Faulkner.[1]

Chapter 2.1 Galvanostatic Charge-Discharge

One of the most widely used electrochemical techniques for battery characterization is galvanostatic (GV) cycling. In a GV charge-discharge test, a constant current is applied to the battery until the set voltage or time limit is reached. From a GV test, the amount of charge stored (mAh), typically reported in specific capacity (mAh g^{-1}) can be determined. In addition, performance metrics such as the Coulombic efficiency (CE) can be obtained from the GV data (Figure 2.1)(Eqn. 2.1). The Coulombic efficiency of a battery provides insights in regard to how well the battery can recover (delithiation capacity) the charge put into it (lithiation capacity). Further, it can also indicate the presence of parasitic reactions such as SEI formation or loss of active material during electrochemical cycling. For commercialized Li-ion cells which operate for thousands of cycles, a high CE is absolutely critical. To provide context, a battery with a coulombic efficiency of 99% will only retain ~60% of its original capacity after 50 cycles and therefore cannot meet the cycle life demands of most portable electronic devices. Therefore, commercialized batteries require very high CEs. For example, Apple's 2021 Macbook Pro is rated to retain 80% of the battery's original capacity by cycle 1000. This would translate to achieving CEs ≥ 99.98%.[2]

$$\mathrm{CE}\ [\%] = \frac{\text{Delithiation Capacity [mAh/g]}}{\text{Lithiation Capacity [mAh/g]}} \times 100 \qquad \text{Eqn. 2.1}$$

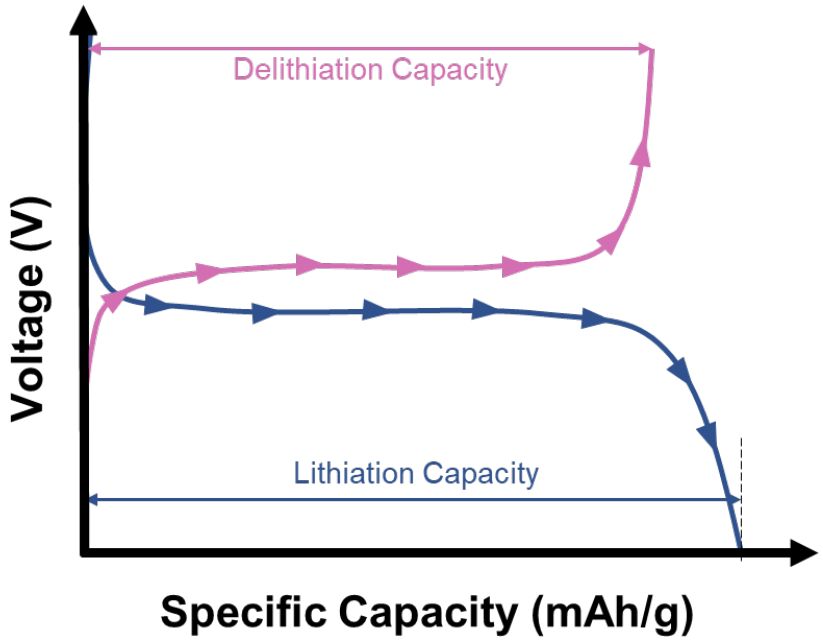

Figure 2.1. Voltage vs Capacity graph. A typical GV curve for a two phase lithiation (blue trace) and delithiation (pink trace) reaction is shown. The difference in lithiation and delithiation capacity is reflected in the coulombic efficiency of the cell.

The applied currents in a GV test are commonly reported in C-rates but can also be reported in specific currents (mA g^{-1}) or current densities (mA cm^{-2}). C-rates are currents that are normalized to the theoretical or maximum capacity and defined by the amount of time it takes to charge or discharge the material as shown in Eqn. 2.2. For example, a C-rate of C/20 and 2C indicates a charge or discharge time of 20 hours and 0.5 hours, respectively. From C-rate testing, capacity as a function of C-rate can provide information in regard to the kinetics of the system which should become more apparent at higher C-rates where kinetic limitations can be easily identified. At slow C-rates (small currents), the overpotentials are minor and the deviation from the open circuit potential is small. However, moving towards higher C-rates (and thus higher currents), the system can experience a variety of polarization losses (ohmic, concentration, and activation polarization) which can be observed in the GV data (Figure 2.2). In addition, at higher

C-rates, there is less time allowed for the battery to undergo redox processes (ion transport in the electrolyte, redox reaction at the interface, solid state diffusion of Li in the active material) and reach its voltage limit. As a result, at higher C-rates, kinetic limitations result in the reduction of capacity. The extent of these effects can vary depending on a range of factors including the electronic conductivity, charge transfer reaction kinetics, and ion transport within the electrode and electrolyte.[3]

$$\mathrm{C-rate\ [mA]} = \frac{\text{Maximum Capacity [mAh]}}{\text{Time it takes to completely charge or discharge battery [h]}} \qquad \text{Eqn. 2.2}$$

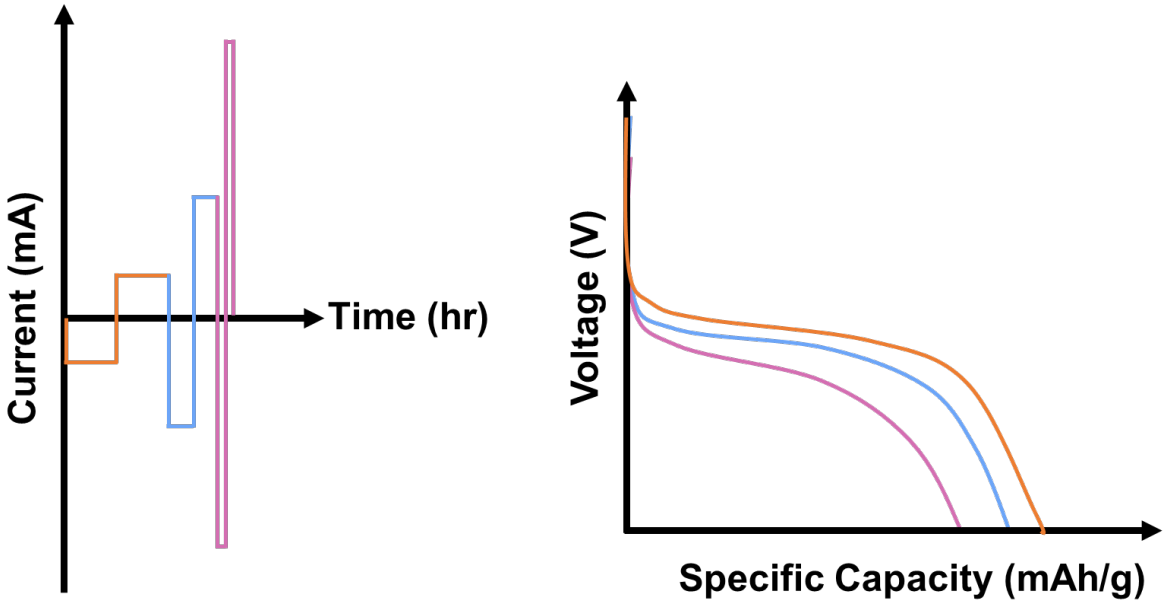

Figure 2.2. C-rate testing protocol. The left graph depicts the current vs time plot which shows a series of constant currents applied to the battery. For higher C-rates, the cell experiences higher currents for a shorter period of time. The graph on the right shows a qualitative graph of a typical C-rate test plot. Slower C-rates (orange trace) typically show lower overpotentials and higher

capacities while moving to higher C-rates results in increased overpotentials and reduced capacities.

Chapter 2.2. Li Plating/Stripping & Butler Volmer Kinetics

In Chapter 3, lithium plating/stripping tests are used to determine the overpotentials (η) and obtain the exchange current (i_o). Overpotential can be defined as the difference between the thermodynamically determined redox potential and the potential at which the redox event is experimentally observed (Eqn. 2.3).[1]

$$\eta = \mathrm{E} - \mathrm{E_{eq}} \qquad \text{Eqn. 2.3}$$

where η=overpotetial, E=experimentally observed redox potential, and E_{eq}= thermodynamic redox potential

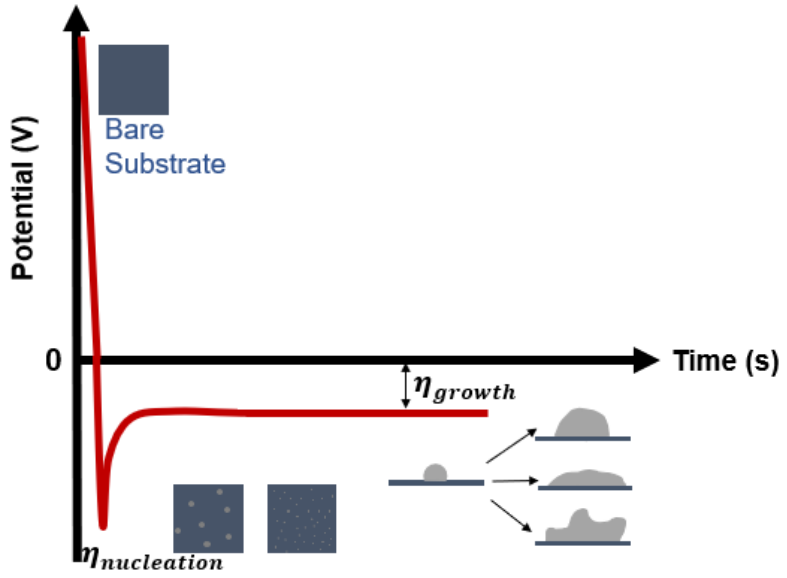

Figure 2.3. Li plating profile graph. During the plating process, negative current is applied to the working electrode. As the voltage is brought below 0 V vs Li^+/Li^0, plating becomes favorable and begins with the creation of Li nuclei followed by the subsequent growth of the nuclei.

For a lithium metal anode, charge is stored through a Li plating process in which Li-ions in the electrolyte accept an electron from the working electrode and become reduced to Li^0. Figure 2.3 shows a typical Li plating profile. In general, the working electrode is an electronically conductive substrate that does not alloy with Li (i.e. copper, stainless steel, or lithium foil). While the thermodynamic reduction potential for Li ($Li^+ + e^- \rightarrow Li^0$) is 0 V vs Li^+/Li^0 (-3.1 V vs S.H.E.), an overpotential (driving force) is required for the plating reaction to occur. Therefore, plating will occur at a potential below 0 V vs Li^+/Li^0 and the magnitude of the overpotential should depend on factors such as the current density, substrate, and electrolyte.[4–6] The plating profile typically shows a sharp kink feature followed by a steadier overpotential which are often cited as nucleation and growth processes respectively.[7,8] Greater detail can be found in Chapter 3.

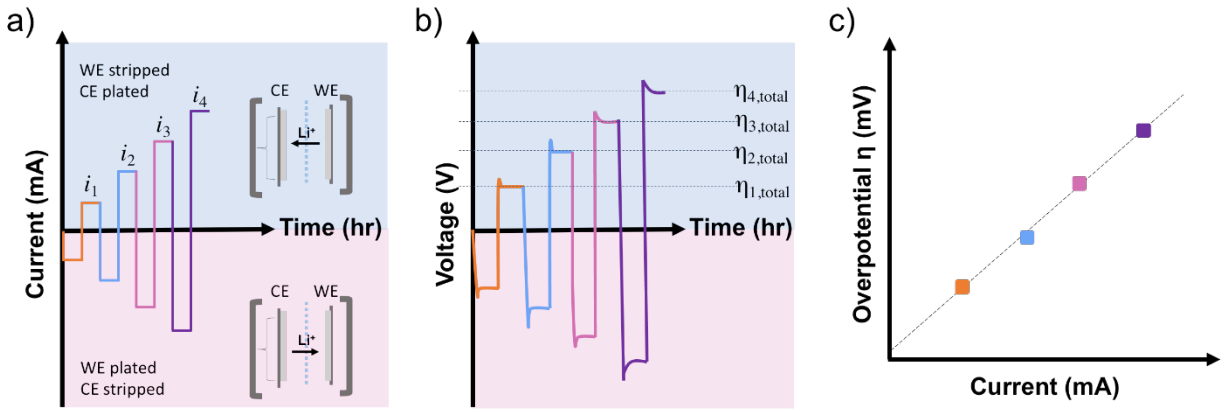

Figure 2.4. Galvanostatic Linear Polarization (GLP) testing protocol. a) current vs time graph showing a series of small current pulses applied to a symmetric coin cell. b) voltage vs time plot showing overpotential (η) for plating/stripping. c) overpotential vs current plot showing the applied current vs the overpotentials obtained from b). At small currents and small overpotentials, a linear trend should be observed.

Symmetric cells are a popular testing format for Li plating/stripping tests. By using a Li metal working and counter electrode, the number of distinct interfaces can be reduced. The open circuit potential of a symmetric cell is ~0 V. However, under the application of a current, the cell is biased, and one electrode undergoes Li plating while the other, Li stripping (Figure 2.4). In Chapter 3, a galvanostatic linear polarization (GLP) (Figure 2.4) is conducted in a symmetric cell to obtain the exchange current (i_o). The exchange current is an important parameter in electrochemical reactions and describes the kinetics of the charge transfer and rate of reaction occurring at the electrode/electrolyte interface.[1,9] While the net current at equilibrium is zero, the anodic and cathodic currents are equal and opposite, and the exchange current is a reflection of the magnitude of this current. Exchange currents can be determined through either Tafel plots or GLP tests which rely on the high and low overpotential regime of the Butler Volmer equation (Eqn. 2.4), respectively. For GLP tests used in Chapter 3, a series of small currents are applied to a symmetric cell and the corresponding overpotentials are measured. Knowing the current applied and corresponding overpotential, the exchange current can be obtained using the Butler-Volmer Equation (Figure 2.5)(Eqn. 2.4) which describes the relationship between the overpotential and current.

$$i = i_o \left[\exp\left(\frac{\alpha z F}{RT}\eta\right) - \exp\left(\frac{(1-\alpha) z F}{RT}\eta\right)\right] \qquad \text{Eqn. 2.4}$$

where i is the current density, i_o is the exchange current density, α is the transfer coefficient, z is number of electrons involved in the reaction, F is Faraday's constant, η is the overpotential, R is the gas constant, and T is the temperature.

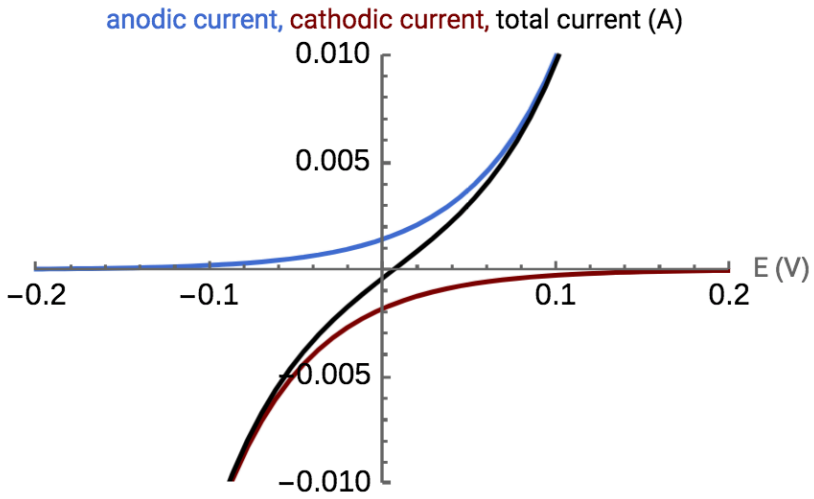

Figure 2.5. A typical Butler-Volmer graph is shown above in black. The anodic (blue) and cathodic (red) contributions are shown, and the black trace represents the superposition of the two curves. Upon the application of a positive overpotential, the anodic reaction dominates while under a negative overpotential, the cathodic reaction dominates.

At low currents, the Butler Volmer relation is linear and referred to as the low overpotential regime. Using a linear approximation (Eqn. 2.5) and assuming the α=0.5, the linearized version of the Butler Volmer can be obtained (Eqn. 2.6).

$$e^{x} \approx 1 + x \qquad \text{Eqn. 2.5}$$

$$i \approx i_o \frac{zF\eta}{RT} \qquad \text{Eqn. 2.6}$$

Where $\eta = \frac{\eta_{total}}{2}$

Lastly, under the assumption that the plating and stripping overpotentials are similar ($\eta_{plating} \approx \eta_{stripping}$), the overpotential at each interface should be approximately half of that

measured from the GLP experiment ($\eta_{total} = \eta_{plating} + \eta_{stripping} \approx \frac{\eta plating}{2}$). From these assumptions, the exchange current can be obtained using eqn. 2.6.

Chapter 2.3. Differential Capacity (dQ/dV)

In Chapter 4, Differential Capacity (dQ/dV) analysis is utilized to characterize specific regions within the FeS_2 GV profile to better identify at what potentials the redox reactions are occurring and how they change upon further cycling or by varying the C-rate. In addition, it has been used as a tool to better understand battery aging and degradation. dQ/dV curves can be obtained by differentiating the capacity (Q) versus the Voltage (V) (Eqn. 2.7). This can be done using software such as Matlab or can often be found built into the battery testing software (Biologic). Figure 2.6 shows an example of a dQ/dV plot processed from a GV plot. Similar to cyclic voltammetry, peaks will be observed at potentials where redox reactions take place. However, dQ/dV is processed from constant current GV data and can be more representative of practical battery conditions.[10,11]

$$\frac{|\delta Q|}{dV} = \frac{|Q_t - Q_{t-1}|}{V_t - V_{t-1}} \qquad \text{Eqn. 2.7}$$

where V_t and E_t represent the capacity and voltage values at time step t, respectively, and Q_{t-1} and V_{t-1} correspond to a previous time step.

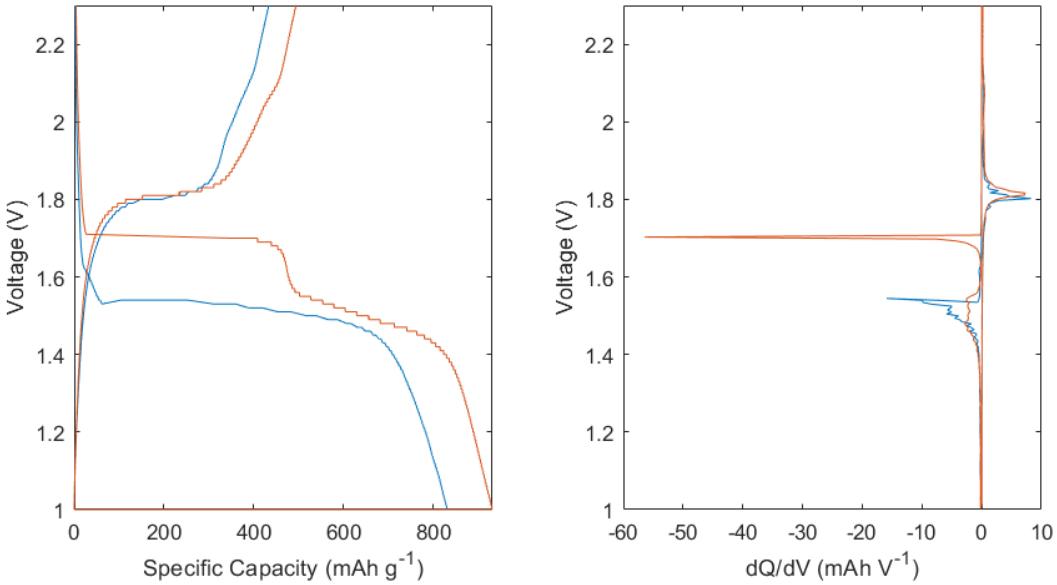

Figure 2.6. Side by side comparison of a galvanostatic charge-discharge curve (left) and the corresponding dQ/dV curve (right).

Chapter 2.4. References

(1) Bard, A. J.; Faulkner, L. R. *Electrochemical Methods: Fundamental and Applications*, 2nd Editio.; John Wiley & Sons: New York, NY, 2001; Vol. 1. https://doi.org/10.1016/B978-0-12-381373-2.00056-9.

(2) Apple. Determine battery cycle count for Mac notebooks https://support.apple.com/en-us/HT201585.

(3) Huggins, R. A. *Advanced Batteries Materials Science Aspects*; 2006; Vol. 34.

(4) Yan, K.; Lu, Z.; Lee, H. W.; Xiong, F.; Hsu, P. C.; Li, Y.; Zhao, J.; Chu, S.; Cui, Y. Selective Deposition and Stable Encapsulation of Lithium through Heterogeneous Seeded Growth. *Nat. Energy* **2016**, *1* (3). https://doi.org/10.1038/NENERGY.2016.10.

(5) Jung, H.; Lee, B.; Lengyel, M.; Axelbaum, R.; Yoo, J.; Kim, Y. S.; Jun, Y. S. Nanoscale: In Situ Detection of Nucleation and Growth of Li Electrodeposition at Various Current Densities. *J. Mater. Chem. A* **2018**, *6* (11), 4629–4635.

https://doi.org/10.1039/c8ta00343b.

(6) Lee, J. Z.; Wynn, T. A.; Schroeder, M. A.; Alvarado, J.; Wang, X.; Xu, K.; Meng, Y. S. Cryogenic Focused Ion Beam Characterization of Lithium Metal Anodes. *ACS Energy Lett.* **2019**, *4* (2), 489–493. https://doi.org/10.1021/acsenergylett.8b02381.

(7) Jung, H.; Lee, B.; Lengyel, M.; Axelbaum, R.; Yoo, J.; Kim, Y. S.; Jun, Y. S. Nanoscale: In Situ Detection of Nucleation and Growth of Li Electrodeposition at Various Current Densities. *J. Mater. Chem. A* **2018**, *6* (11), 4629–4635. https://doi.org/10.1039/c8ta00343b.

(8) Sagane, F.; Ikeda, K. I.; Okita, K.; Sano, H.; Sakaebe, H.; Iriyama, Y. Effects of Current Densities on the Lithium Plating Morphology at a Lithium Phosphorus Oxynitride Glass Electrolyte/Copper Thin Film Interface. *J. Power Sources* **2013**, *233*, 34–42. https://doi.org/10.1016/j.jpowsour.2013.01.051.

(9) Dickinson, E. J. F.; Wain, A. J. The Butler-Volmer Equation in Electrochemical Theory: Origins, Value, and Practical Application. *J. Electroanal. Chem.* **2020**, *872*, 114145. https://doi.org/10.1016/j.jelechem.2020.114145.

(10) Talaie, E.; Bonnick, P.; Sun, X.; Pang, Q.; Liang, X.; Nazar, L. F. Methods and Protocols for Electrochemical Energy Storage Materials Research. *Chem. Mater.* **2017**, *29* (1), 90–105. https://doi.org/10.1021/acs.chemmater.6b02726.

(11) Investigating battery aging using Differential Capacity Analysis (DCA) https://www.biologic.net/topics/investigating-battery-ageing-using-differential-capacity-analysis-dca.

Chapter 3. Lithium Plating Underneath Li-Sn Coating Layers

The use of interfacial layers to stabilize the lithium surface is a popular research direction for improving the morphology of deposited lithium and suppressing lithium dendrite formation. This work considers a different approach to controlling dendrite formation where lithium is plated underneath an interfacial coating. In the present research, a Li-Sn intermetallic was chosen as a model system due to its lithium-rich intermetallic phases and high Li diffusivity. These coatings also exhibit a significantly higher Li exchange current than bare Li thus leading to better charge transfer kinetics. The exchange current is instrumental in determining whether lithium deposition occurs above or below the Li-Sn coating. High-resolution transmission electron microscopy and cryogenic focused ion beam scanning electron microscopy were used to identify the features associated with Li deposition.

Chapter 3.1. Introduction

The Li metal anode is considered to be a critical component for next generation rechargeable batteries due to its high theoretical capacity (3860 mAh g^{-1}) and low reduction potential (-3.040 V vs. S.H.E.) However, the formation of Li dendrites during repeated plating/stripping is a challenge that remains to be fully addressed.[1–3] The problem of Li dendrites is further complicated by the presence of a heterogeneous passivation layer known as the solid electrolyte interface (SEI).[4] Due to the inherently low reduction potential of Li, the SEI formed at the Li surface upon contact with electrolyte results in the immediate electrolyte decomposition and formation of both organic and inorganic decomposition products.[4–6] While the SEI passivates the Li surface from further side reactions under static conditions, it is unstable under electrochemical cycling.[7–9] The compositional heterogeneity of the SEI imparts non-uniform Li-ion fluxes in addition to local differences in mechanical properties which promote the formation of Li dendrites and subsequent fracture of the SEI.[10,11] At higher current densities (> 1 mA cm^{-2}),

dendritic morphologies with high surface areas dominate and continue to form new SEI resulting in continuous loss of active Li. In addition, the breakage of fragile Li dendrites results in the loss of electrical contact and formation of dead Li, which can be directly translated to poor coulombic efficiency.[1] The formation of Li dendrites is a multi-faceted problem that has been addressed through a broad range of approaches over past decades. Strategies employed thus far include the use of electrolyte additives to form a more compact and compositionally uniform SEI,[12,13] high surface area three-dimensional current collectors to reduce the effective current density and accommodate Li volume change,[14,15] separator engineering to mechanically block Li dendrites,[16] lithophilic Li cages/hosts,[15,17,18] and artificial coatings to stabilize the interface.[19–25]

In this work, we describe a different approach towards controlling Li dendrite formation, namely plating lithium underneath a coating formed on Li. This dual purpose coating can stabilize the reactive Li interface during plating/stripping and also facilitate in the transport of Li to allow for Li plating at the Li/coating interface. Although recent work has demonstrated lithium plating beneath a micrometers-thick intermetallic coating[21] there remain open questions on the relationship between the microstructure of the coating and the mechanism which enables Li deposition underneath. The plating of Li underneath a stabilizing layer offers a refreshing perspective on reframing the question of how to best suppress dendrite formation. By confining Li deposition to take place under the coating layer, the growth of lithium dendrites at the anode surface is effectively eliminated. In order to investigate the mechanism of plating underneath coating layers, a Li-Sn system was chosen as a model coating system due to its known ability to form lithium-rich intermetallic compounds [Figure 3.2(c)] which exhibit high Li diffusivity.[26–29] The use of Li-Sn based coatings and substrates has been shown to demonstrate good plating kinetics and cycling performance.[28–30] However, to the best of our knowledge, Li deposition underneath lithium-tin based coatings has not been reported. In this study, we utilized transmission electron

microscopy (TEM) to elucidate the microstructure of the solution processed Li-Sn intermetallic coating on Li, and cryogenic focused ion beam scanning electron microscopy (cryo-FIB-SEM) to characterize the interface morphology under different plating current densities. Through a combination of experiments and theoretical modelling, we identify conditions whereby Li can nucleate either above or underneath the Li-Sn intermetallic coating and thus provide new insight on the mechanism for this lithium plating process.

Chapter 3.2. Experimental Methods

Protective Coating Fabrication

The lithium-tin coating layer was fabricated using a solution-processed route in a sub-ppm Argon-filled glove box(VAC). Anhydrous Tin (II) Chloride (98%, Alfa Aesar) was dissolved and stirred into tetrahydrofuran(Sigma) to form a 50 mM Tin Chloride solution. Lithium metal foil (Alfa Aesar, 99.9%) was polished and subsequently immersed into the Tin(II) chloride solution for ~6-7 seconds to form a conformal dark coating on top of lithium. The coating was left to dry under ambient glovebox conditions for 3 hours and rinsed in dioxolane. For coin cell electrodes, lithium disks were punched out and pressed onto stainless steel spacers before immersing into the tin (II) chloride solution.

Coating Characterization

SEM (Nova NanoSEM230; Thermo Fisher Scientific) and EDX images (Noran System 7, Thermo Fisher Scientific) were obtained using an accelerating voltage of 10.0 kV to image the plan view morphology of the pristine and plated Li-Sn layers. The samples were exposed for a few seconds to ambient air during the sample transfer into the SEM chamber. EDX spectral maps were obtained to characterize the composition of the layer. X-ray photoelectron spectroscopy (XPS; Kratos Axis Ultra) with a monochromatic aluminum X-ray source was performed on the lithium tin coating layer using a voltage of 10kV and emission current of 10 mA. Peak calibration

was performed using the adventitious carbon peak (284.8 eV). Analysis was carried out in CasaXPS software. TEM characterization of the coating layer was conducted using a JEOL 2800 TEM at 300 kV. The coating layer was gently scraped off from the Li metal surface and collected with a Cu grid inside an Ar-filled glovebox. The sample loading was conducted with direct Ar flow toward the sample holder to minimize air exposure. The coating cross-section was characterized using a FEI Scios Dualbeam FIB/SEM. A Ga-ion beam source at 30 kV was used to mill the sample. To preserve the coating and Li morphology, a cryo stage was used during the milling process. The cryo stage temperature was maintained below -180 °C using a heat exchanger in liquid nitrogen. X-ray Diffraction was performed using a PANalytical X'Pert Pro diffractometer using a Cu Kα (λ = 1.5418 Å) source. Samples were sealed in kapton to prevent air exposure. XRD patterns were recorded in the range of 30° < 2θ < 70° using a 0.03° step size, a voltage of 45 kV, and a current of 40 mA.

Electrochemical Characterization

Galvanostatic plating/stripping experiments were conducted in a symmetric coin cell using a 25mm thick polypropylene separator and 80 μL of 1M lithium bis(trifluoromethane)sulfonimide (LiTFSI) in dioxolane/dimethoxyethane (DOL/DME) (1:1 vol). Current densities of 100 μA cm^{-2} to 2mA cm^{-2} were used for the plating studies. For the galvanostatic linear polarization experiments, symmetric coin cells were subject to 3 cycles of plating and stripping for a set of current densities ranging from 5 to 50 μA cm^{-2}. In the calculation of the exchange current density, the plating and stripping overpotentials were assumed to be similar thus the plating overpotential was assumed to be half of the total overpotential and used to calculate the exchange current density. The low overpotential, linearized form of the Butler-Volmer equation was used in our study (See Chapter 2).

Chapter 3.3. Results & Discussion

Chapter 3.3.1. Li-Sn Composite Coating Fabrication and Characterization

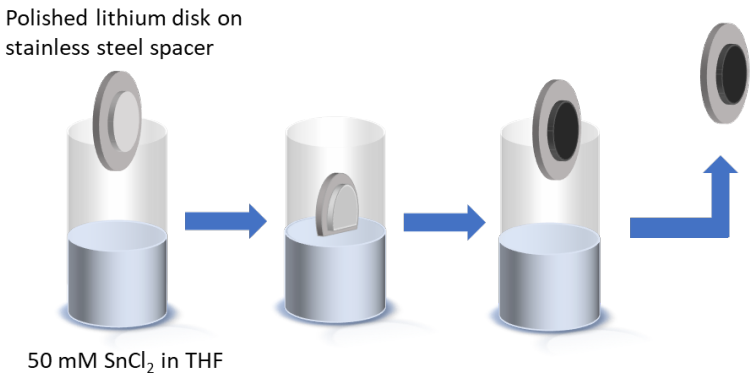

Figure 3.1. Schematic of the fabrication of Li-Sn/Cl composite coatings.

Li-Sn composite coatings were formed through a solution processing route using a 50 mM solution of $SnCl_2$ dissolved in THF (Figure 3.1). Due to the reducing power and chemical reactivity of Li, the direct immersion of Li foil in the $SnCl_2$ solution resulted in the immediate reduction of the chloride solution on the lithium surface, producing a dark grey coating with intimate contact to the bulk foil. The plan-view SEM image in Figure 3.2(b) reveals the microstructure of the coating surface. The reaction between the bare Li and the $SnCl_2$ solution produced a uniform coating consisting of submicron particle-like features. Cryo-FIB SEM was utilized to characterize the cross-section of the layer to reduce the risk of ion beam damage. As shown in Figure 3.2(d), the coating is dense and has a thickness of around 1 μm. EDS mapping (Figure 3.3) confirms the uniform distribution of both Sn and Cl throughout the bulk coating.

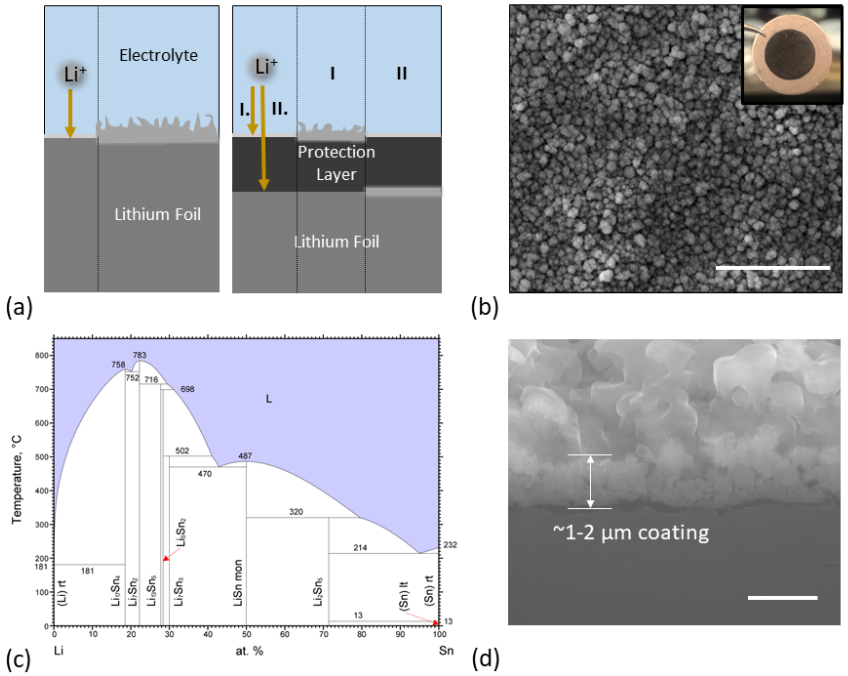

Figure 3.2. (a) Schematic comparing Li plating locations in bare lithium (left) and in a Li-Sn coating system (right) (b) Plan-view SEM image of coating morphology. Scale bar is 10 µm. Photograph of a pristine Li-Sn coating on a stainless steel spacer is shown on top right corner. (c) Lithium-Tin binary phase diagram[31] (d) cryo-FIB cross-sectional SEM image of Li-Sn coating on bulk Li foil. Scale bar is 1 µm.

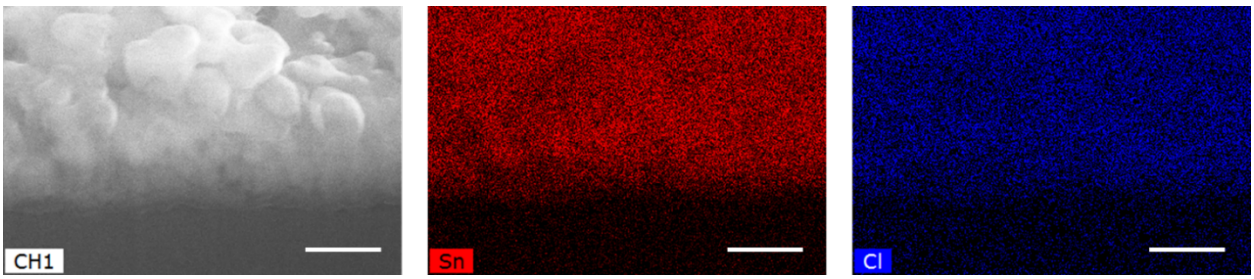

Figure 3.3. EDX spectral mapping of a pristine coating cross section. Scale bar is 1 µm.

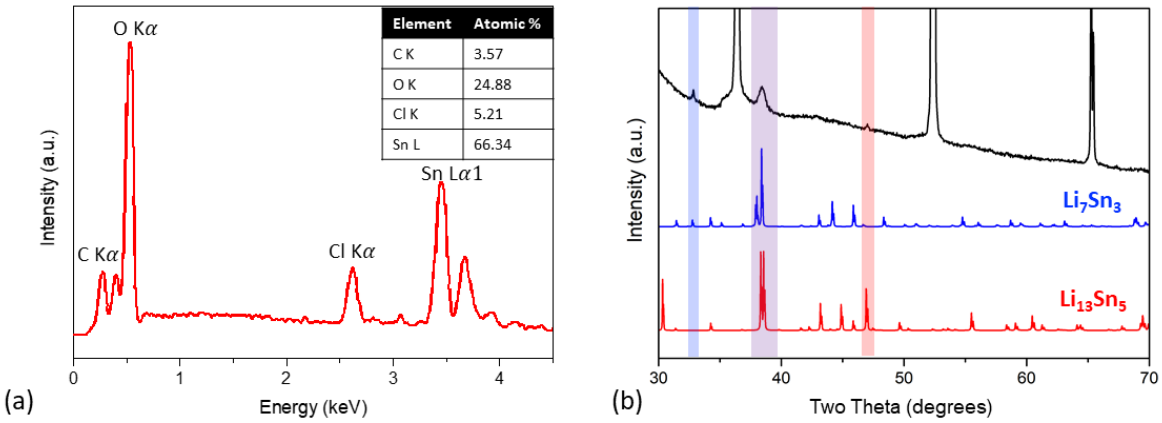

Figure 3.4. (a) Energy Dispersive Spectroscopy (EDS) of the Li-Sn coating showing both tin and chlorine signals and the corresponding atomic percentages. (b) X-ray Diffraction (XRD) pattern of Li-Sn coating (black) along with reference scans for Li_7Sn_3 (blue), and $Li_{13}Sn_5$ (red).

The structure and phases of the coating were characterized with XRD and HRTEM. The (2θ) diffraction peaks at 32.6 degrees and 46.8 degrees in Figure 3.4(b) suggest that the coating likely contains both crystalline Li_7Sn_3 ($P12_1/m1$, ICSD-104785) and $Li_{13}Sn_5$ ($P\bar{3}m1$, ICSD-104786) phases. The broad diffraction peak at 38 degrees indicates the combination of the two Li-rich intermetallic phases, Li_7Sn_3 and $Li_{13}Sn_5$. Additionally, the broadness and low intensity of the diffraction peaks indicate that the intermetallic species present in the coating layer were either nanocrystalline and/or there were amorphous regions within the coating. HRTEM was utilized to further understand the microstructural characteristics of the layer which showed the presence of percolating nanocrystalline phases embedded in an amorphous matrix .Figure 3.5(a, c-d)]. The Fast Fourier Transform (FFT) pattern of the entire region in Figure 3.5(b) showed the existence of Li_7Sn_3 and $Li_{13}Sn_5$ phases. In Figure 3.5(c), the magnified TEM micrograph showed grains with d-spacing measured to be 0.20 nm and 0.23 nm. These values correspond to orientations of

Li_7Sn_3 (102) and Li_7Sn_3 (212)/$Li_{13}Sn_5$ (110), respectively. The crystalline regions contain intermetallic grains that are <10 nm in diameter in addition to amorphous regions between the grains. The direct observation of amorphous regions could help to explain the broad and low intensity peaks observed for other solution processed intermetallic coatings.[21,30]

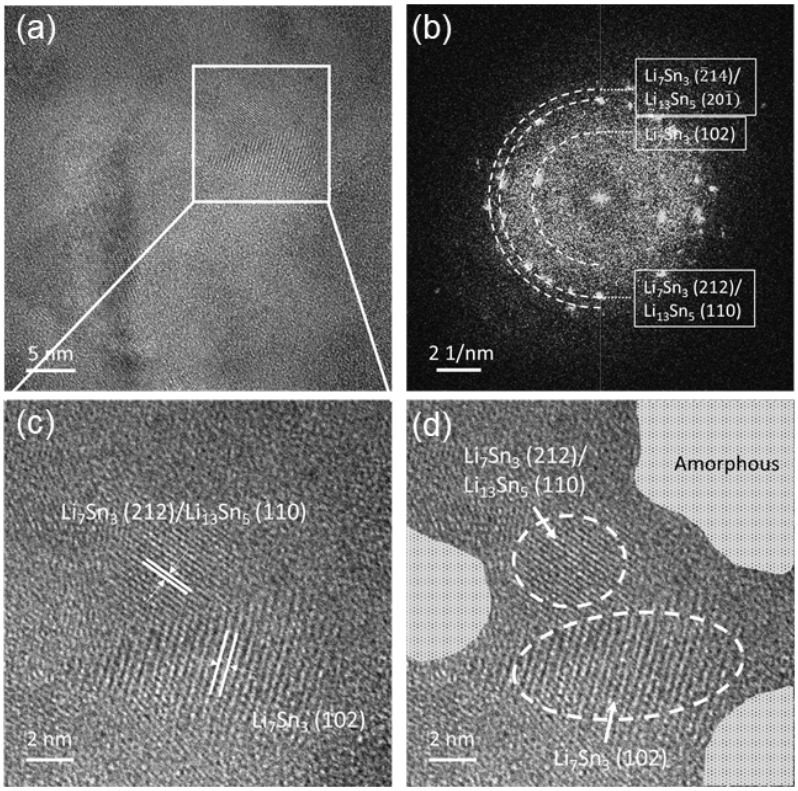

Figure 3.5. HRTEM micrographs of the Li-Sn composite coating. (a) Low-magnification image of composite coating. (b) FFT pattern of the entire region in part a. (c) High-magnification image of the composite coating. (d) Phase distribution schematic overlaying the HRTEM image. The coating contains Li_7Sn_3, $Li_{13}Sn_5$, and amorphous regions.

Chapter 3.3.2. Chlorine in the Composite Coating

The chlorine in the layer is suspected to be LiCl. In previous reports[21,31,32] LiCl was reported to form as a reaction product in a two-step reaction between Li and the metal chloride (MCl_x)[21]:

$$Li + MCl_x \rightarrow M + xLiCl.$$

$$yLi + zM \rightarrow Li_yM_z$$

Around 5% chlorine was detected by EDX analysis to be present within the intermetallic layer .Figure 3.4(a)]. Thus, the chlorine species is a minor constituent of the coating layer. To complement the EDX results, XPS was used to provide chemical information regarding the nanometer region near the surface (<10 nm)[33] of the coating. Both Cl $2p_{1/2}$ and Cl $2p_{3/2}$ were detected based on signals at 200.04 eV and 198.39 eV, respectively. These energies lie within comparable binding energies reported for the chlorine species produced under similar solution processing routes.[21,31,32] The Cl 2p signals could still be observed with no peak shifts after 15 minutes of argon ion etching (Figure 3.6), indicating that the chlorine species does not change in or near the surface of the coating while the cross-sectional EDS mapping demonstrated a uniform distribution of Cl signals throughout the bulk of the coating (Figure 3.3).

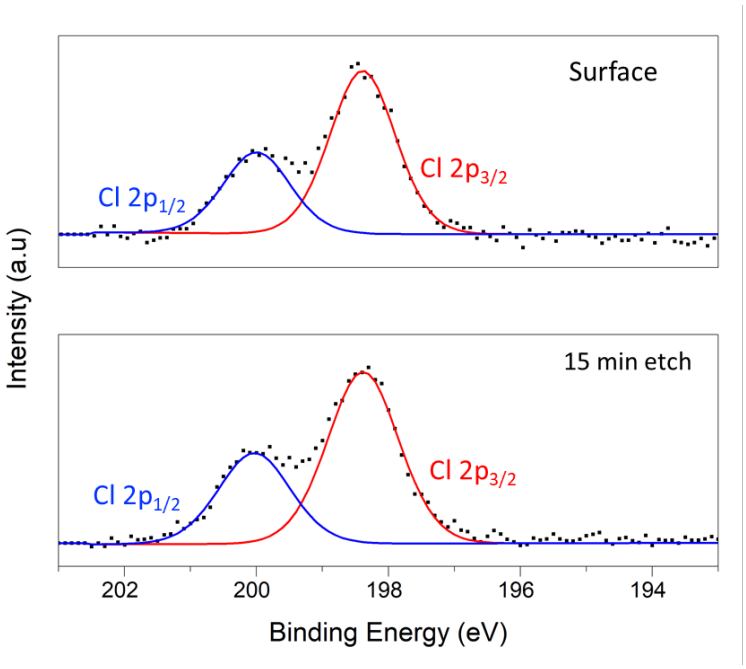

Figure 3.6 XPS of Cl 2p before and after 15 minutes of Ar^+ etching.

The fact that crystalline LiCl was not detected in either XRD or FFT patterns is not surprising [Figures 3.4(b) and 3.5(b)]. This result is consistent with previous reports for metal chloride solution-processed intermetallic coatings[21,31,32] which assume the formation of an amorphous/nanocrystalline LiCl phase but provide no further evidence. In our study, the microstructure of the coating layer was revealed to contain amorphous regions (Figure 3.5). To further assess the most likely chlorine species in the layer, density functional theory (DFT) calculations were performed to determine the most stable surfaces for $Li_{13}Sn_5$ and Li_7Sn_3. In a second series of calculations, a comparison of reaction energies was made for different Cl configurations on the most stable surfaces, inside the bulk intermetallic phases, or as a separate LiCl phase. Table 3.1 shows the reaction energies of various Cl configurations for both intermetallic phases. The formation of a separate LiCl phase is energetically more favorable over the doping of Cl into the intermetallic structure for both $Li_{13}Sn_5$ and Li_7Sn_3. While the presence of LiCl is not expected to take part in lithium transport due to its low lithium diffusivity, it can be of

benefit to a coating layer by imparting fast surface diffusivity at the electrolyte/electrode interface which has been reported for lithium halide salts.[34]

Table 3.1. The reaction energies (eV) to form a Cl doped LiSn intermetallic structures (either in the bulk or at the surface) and a separate LiCl phase for Li-Sn coating layer, energies are normalized as per $SnCl_2$ chemical formula.

Systems	$Li_{13}Sn_5$ Phase			Li_7Sn_3 Phase	
	Cl doped bulk	Cl doped (001) surface	Separate LiCl	Cl doped bulk	Separate LiCl
Reaction Energy (eV)	-5.72	-5.74	-5.86	-5.08	-5.72

Although the question of whether an amorphous LiCl phase forms is outside the scope of this paper, an interesting possibility is that the amorphous region is a Li-Sn-Cl glass. Regions of binary or multi-component systems with decreased liquidus temperature are known to have increased glass forming ability[35] and the binary system of LiCl-$SnCl_2$ displays a eutectic at 488 K.[36,37] Thus, there is the prospect that $SnCl_2$ from the solution and LiCl from the reaction product react to form an amorphous phase with a eutectic-like composition. It is interesting to note that binary and multicomponent metal chloride based glasses have been known for decades.[38–40]

Chapter 3.3.3. Lithium Plating Exchange Current

In order to study the kinetics of the lithium plating process in the Li-Sn composite coatings, the Butler-Volmer equation was used to determine the exchange current of the coating layer system. The exchange current is a reflection of the kinetics of the charge transfer process and

the rate of the reaction occurring at the electrode/electrolyte interface.[41] While Tafel plots are commonly employed to determine the exchange currents using the high overpotential approximation, it has recently been reported that the Butler Volmer Equation fails to describe the kinetics of lithium plating and stripping at overpotentials above 50 mV.[42] Therefore, the linear, low overpotential regime of the Butler-Volmer equation (See Chapter 2) was used to extrapolate the exchange current from a galvanostatic linear polarization experiment [Figure 3.7(a)]. The lithium plating exchange current of the Li-Sn coating was found to be twice that of the bare lithium control, indicating more favorable charge transfer plating kinetics in the Li-Sn layer over the bare lithium control. The exchange current is inversely proportional to the charge transfer resistance,[41] which can also be seen in the impedance measurements [Figure 3.7(c) and 4(d)]. The Nyquist plot of the data not only shows a lower charge transfer resistance for the Li-Sn coating, but also demonstrates the ability of the coating to stabilize the lithium surface throughout the repeated plating and stripping during the galvanostatic linear polarization tests. In contrast, the bare lithium control suffers from a continuous increase in charge transfer resistance throughout the galvanostatic linear polarization measurement. This can be attributed to an increased surface area from non-uniform lithium deposition/stripping and the accompanying formation of more SEI, resulting in increased resistance.[25,43–45] The higher exchange current in combination with the stabilizing effect of the Li-Sn coating is expected to be favorable in terms of plating and stripping by imparting faster plating/stripping kinetics in addition to providing surface stabilization during electrochemical cycling.

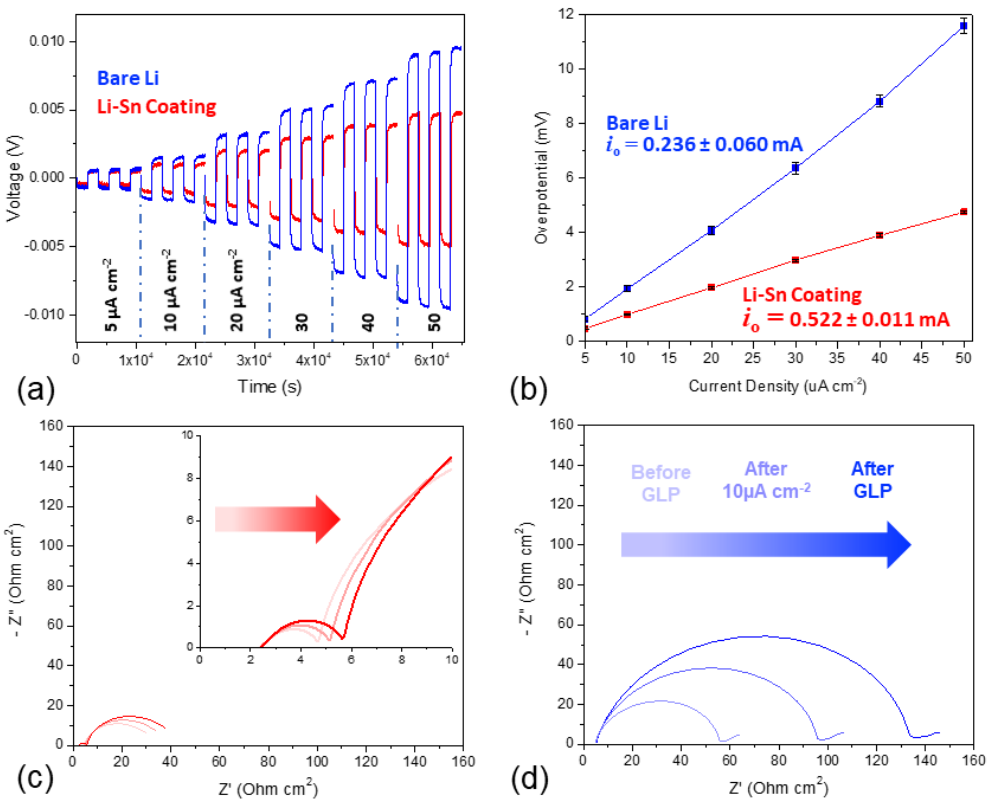

Figure 3.7. (a) Voltage vs. time profile of the galvanostatic linear polarization tests using current densities of 5, 10, 20, 30, 40 and 50 µA cm^{-2} (b) Overpotential vs. current density plot demonstrating a linear trend for low overpotentials along with the corresponding exchange currents extrapolated from the galvanostatic linear polarization test. (c) Nyquist plot of the Li-Sn coated lithium symmetric cell. The light red trace represents the impedance before the test, the medium red trace represents the impedance during the test, and the dark red trace represents the impedance after the test. (d) Nyquist plot of a lithium control (no coating) symmetric cell which shows a larger initial impedance in addition to large increases throughout the test.

Chapter 3.3.4. The Role of Plating Current Density in Lithium-Tin Coatings

In order to study the effect of the plating current density in Li-Sn coatings, two test case current densities were chosen: 1) a low current density of 0.1 mA cm^{-2} that is below the exchange

current densities of both Li-Sn coating and bare lithium systems and 2) a high current density of 2 mA cm^{-2} that is above the exchange current density and represents a current density commonly used in Li plating studies.[21,46,47] For a bare lithium anode (no Li-Sn coating), lower currents, and thus smaller overpotentials (driving force), result in a larger critical radius for nucleation as shown by Equation 3.1:[47]

$$r_c = -\frac{2\gamma_{n/e}\Omega}{F\eta} \qquad \text{Eqn. 3.1}$$

where r_c is the critical nucleus radius, $\gamma_{n/e}$ is the interfacial energy between the Li nucleus and the electrolyte, Ω is the molecular volume of Li , F is Faraday's constant, and η is the overpotential.

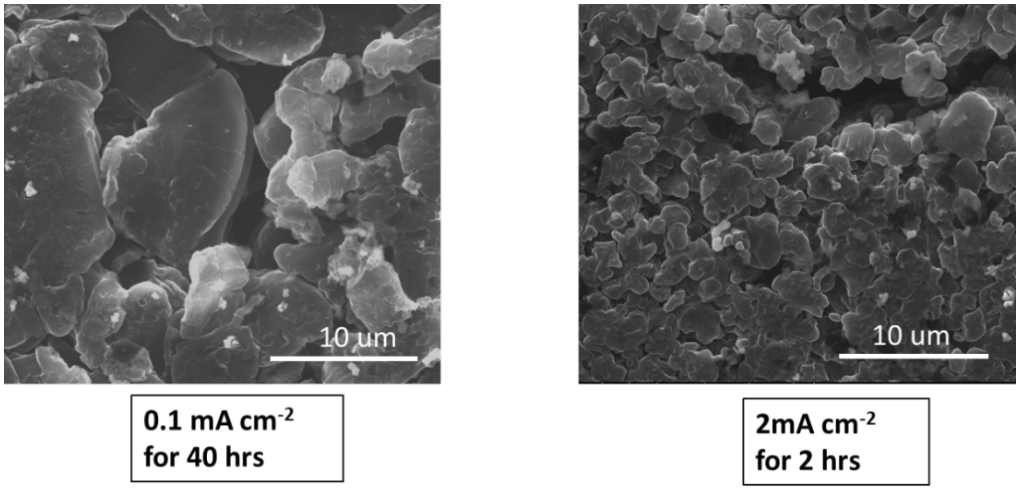

Figure 3.8. Bare lithium plating morphology at 0.1 mA cm^{-2} (left) and 2 mA cm^{-2} (right) for a plating capacity of 4 mAh cm^{-2}.

As a result, at lower current densities, more favorable plating morphologies with larger deposited features are typically observed whereas at high current densities of 2 mA cm^{-2}, smaller features with higher surface area morphologies are more favorable to form (Figure 3.8). However,

unlike bare lithium, where lithium ions in the electrolyte have no other option but to plate on the lithium surface, Li-Sn coatings not only offer the possibility for heterogeneous lithium nucleation on top of the coating surface but also the possibility to plate underneath the coating. For plating to occur underneath, the charge transfer kinetics at the interface must be favorable in addition to the transport of lithium through the layer, which must be relatively fast to minimize polarization and resistance within the coating.

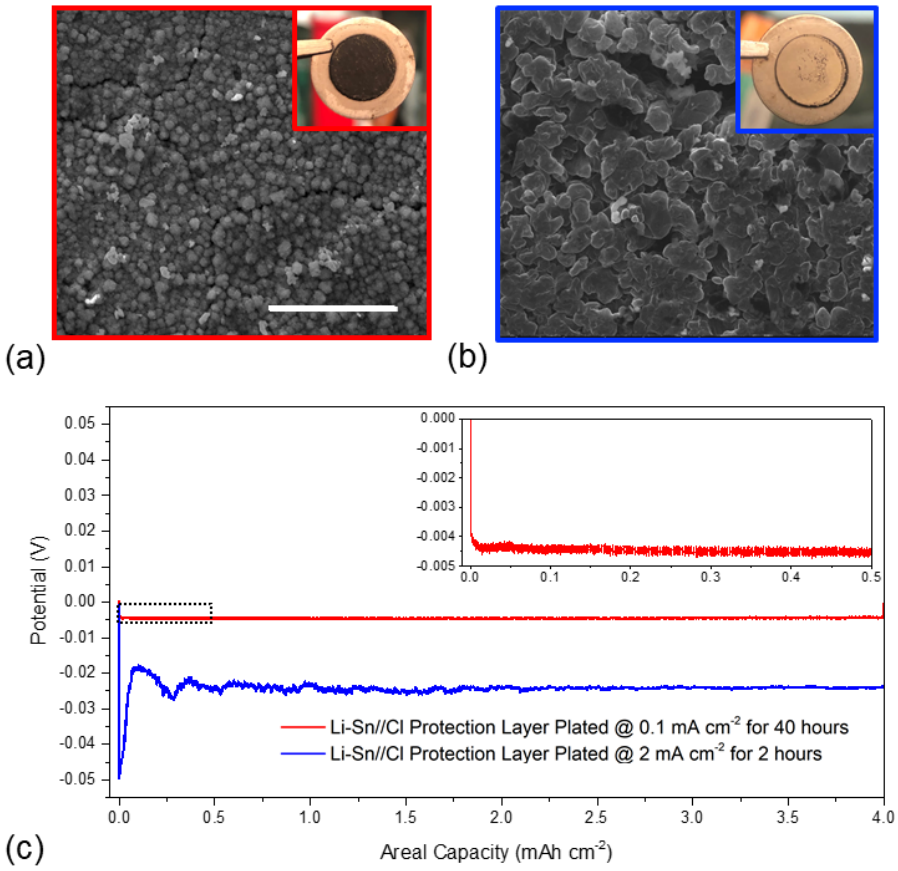

Figure 3.9. (a) Plan-view SEM of a Li-Sn coated lithium plated at 0.1 mA cm^{-2} for a plating capacity of 4 mAh cm^{-2}. Scale bar is 10 μm (b) Plan-view SEM of a Li-Sn coated lithium plated at 2 mA cm^{-2} for a plating capacity of 4 mAh cm^{-2}. Scale bar is Scale bar is 10 μm (c) Potential profile of Li-

Sn coated Li plated at a current density of 0.1 mA cm^{-2} (red) and 2 mA cm^{-2} with the same areal capacity of 4 mAh cm^{-2}. Inset shows a zoom up of the 0.1 mA cm^{-2} plated sample which demonstrated a steady overpotential with less than 1 mV throughout the entire 40 hours.

Figure 3.9(c) shows the electrochemical signature of lithium plating in Li-Sn coatings plated at the low and high test case current densities. For the high plating current sample, the initial kink observed is commonly attributed to the nucleation overpotential for the lithium plating and the subsequent steadier overpotential after the nucleation event is related to the continuous growth of the deposits.[47,48] However, in the potential profile for the low plating current, there was no visible nucleation overpotential. The lack of a nucleation kink was also observed in a bare lithium symmetric cell plated at 0.1 mA cm^{-2} thus indicating that at the lower current densities, the nucleation and growth overpotentials are similar (Figure 3.10).

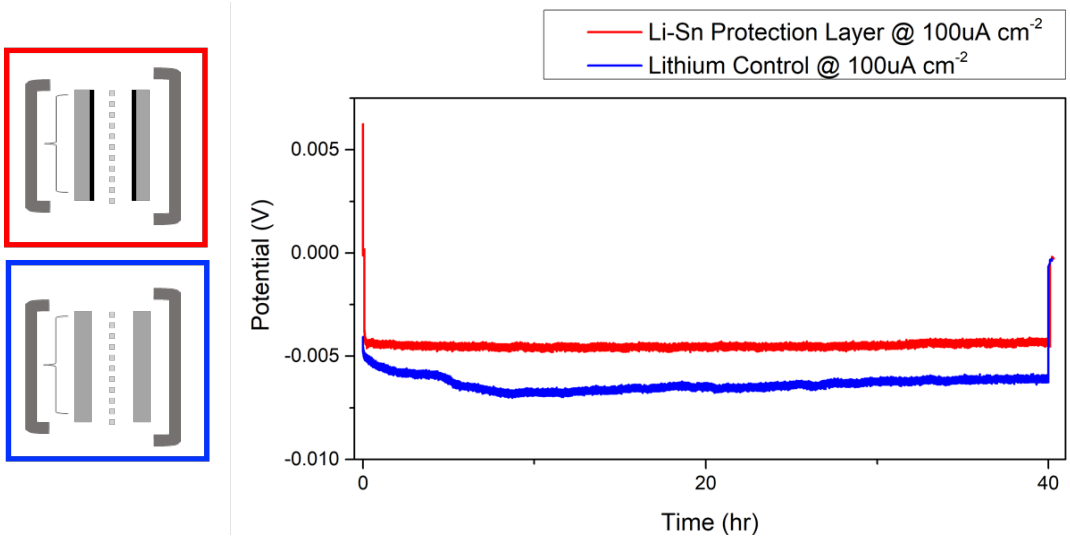

Figure 3.10. Comparison of Li plating profile for Li-Sn coating and bare lithium control at 0.1 mA cm^{-2}.

However, in the bare lithium plating profile, the growth overpotential exhibited fluctuations which are likely the result of lithium deposition changing the electrode surface. In contrast, the Li-Sn sample plated at the low current density of 0.1mA cm^{-2} [Figure 3.9(c)] demonstrated a stable overpotential with less than 1 mV change throughout the entire 40 hours of plating. The stability of the overpotential profile can be an indicator of the unchanging surface of the electrode as a result of lithium deposition underneath and preservation of the Li-Sn coating surface exposed to the electrolyte. In contrast, when lithium deposition occurs on the top of the Li-Sn coating, slight fluctuations in the overpotential [Figure 3.9(c)] are exhibited and attributed to the changing surface area [Figure 3.9(b)] associated with the non-uniform Li deposition.[49,50]

In terms of the physical appearance of the electrodes, even at a plating capacity as high as 4 mAh cm^{-2}, no lithium plating was observed on the surface of the lithium tin coating for the lower plating current density (0.1 mA cm^{-2}). A capacity of 4 mAh cm^{-2} equates to roughly 20 μm of plated lithium assuming uniform deposition and should be identifiable even from visual inspection. In comparing the different current densities, the plated lithium for the higher plating current density sample [Figure 3.9(b)], is confined to the upper surface, covering the dark grey/black Li-Sn coating completely, while the lower plating current density sample retained the lithium tin coating morphology [Figure 3.9(a)]. The drastic visual differences between the two samples indicate that there exists a critical current at which the lithium deposition location can be tuned to favor either plating at the surface or underneath the Li-Sn coating. This critical current is likely influenced by the exchange current density, which reflects the ease of charge transfer at the interface in addition to the fast transport of lithium through the coating via the lithium-rich intermetallic phase (vide infra). While plan-view SEM images show the absence of lithium on the surface of the lower plating current density sample, the use of cross-sectional Cryo-FIB SEM is able to elucidate the presence of buried lithium underneath the interface.

Chapter 3.3.5. Probing above and beneath the Li-Sn layer

Cryo-FIB SEM was used to probe the Li plating morphology while minimizing the artifacts from the ion milling process.[30,51] For the Cryo-FIB samples, a smaller plating capacity of 1 mAh cm^{-2} was chosen to minimize the Cryo-FIB milling time. One key question to address was whether plated lithium could be distinguished from the bulk underlying lithium foil using the FIB milling process. As a control, a high plating current density sample (2 mA cm^{-2}, 1 mAh cm^{-2}) where lithium plated on top of the Li-Sn coating was analyzed to: 1) determine whether the Li-Sn layer could be easily distinguished and 2) compare the plated lithium to the bulk lithium foil underneath the Li-Sn layer. Figure 3.11(b) shows that at the higher current density of 2 mA cm^{-2}, heterogeneous nucleation of Li on top of the coating is observed and lithium deposition occurs on the top of the Li-Sn layer.

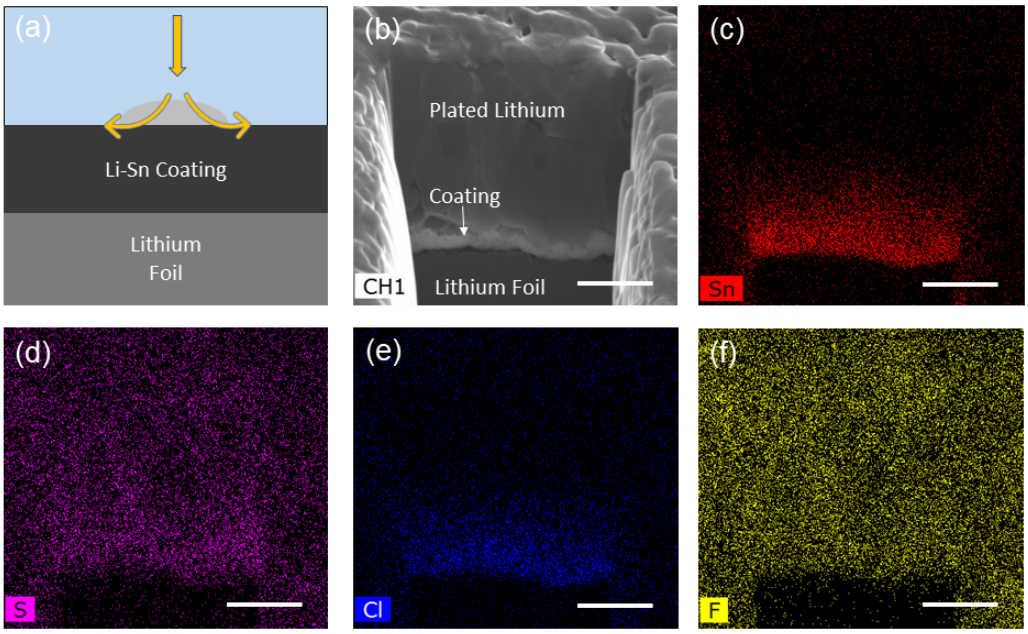

Figure 3.11. (a) Graphic representing high plating current density case where lithium is observed to plate on top of the Li-Sn coating (b) Cryo FIB cross-section SEM of Li plated on top of Li-Sn coating at a current density of 2 mA cm^{-2} for a capacity of 1 mAh cm^{-2}. Scale bar is 2 μm. (c)-(f) EDX elemental mapping of the cross-section. Scale bar is 2 μm.

The nucleation of Li is driven by overpotential[52] whereby larger currents result in larger overpotentials. The Everhart-Thornley Detector (ETD) SEM image in Figure 3.11(b) shows the plated lithium on top of the Li-Sn coating. The plated Li above the coating can be better distinguished from the Li-Sn coating using a Backscattered Electron Detector (BSED), which provides greater contrast due to the atomic number dependence of backscattered electrons (Figure 3.12). The large difference between the atomic numbers of Sn (z=50) and Li (z=3), allow us to easily distinguish lithium (both plated and bulk foil) from the Li-Sn coating. While the plated and underlying bulk foil are both lithium, the plated lithium contains signals from the SEI (Fluorine, Sulfur, Carbon) which represents a characteristic feature of plated lithium observed in this study [Figure 3.11(c)-(f)].

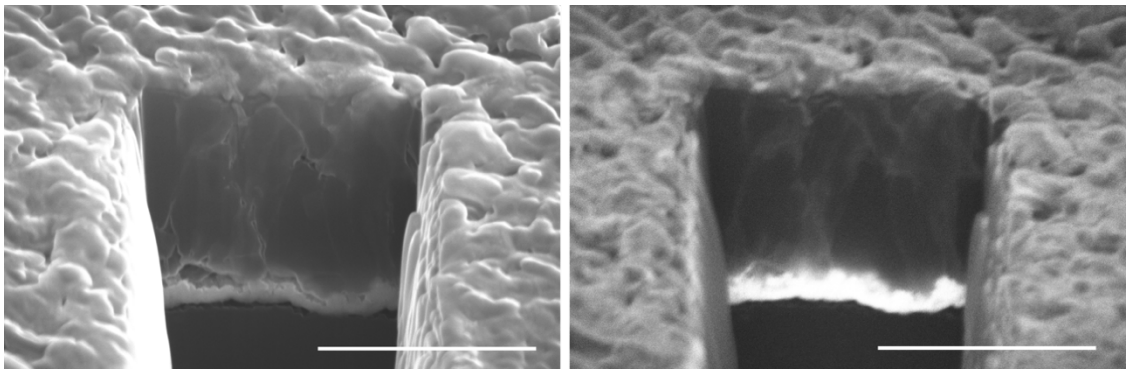

Figure 3.12 Comparison of Everhart Thornley Detector (ETD) (left) and backscattered electron detector (BSED) (right) SEM image for Li plated at 2 mA cm^{-2}. Scale bar 5 μm.

The thickness of Li for 1 mAh cm^{-2}, assuming uniform deposition, is expected to be around 4.8 μm. This agrees well with the measured cross-section thickness for plated Li (4.87 $\pm$ 0.21 μm) indicating relatively uniform and dense Li deposition [Figure 3.11(b)]. While Li plating occurred on top of the Li-Sn layer at higher current densities, the deposited Li layer exhibited a dense

morphology. This demonstrates the critical influence of the substrate in lithium plating, which has previously shown favorable plating morphologies for tin-based interfaces.[30] The dense morphology for Li deposited at the higher current density of 2 mA cm^{-2} can be attributed to the fast surface diffusion at the Li-Sn coating interfaces. In addition to the contribution of the intermetallic phase, the presence of the chloride species also plays an important role in the surface diffusion of lithium when considering plating above the Li-Sn coating. The presence of lithium halide salts has been reported to improve plating morphology, which can be correlated to an enhanced surface diffusion from the halide due to a reduced barrier for Li diffusion at the electrode/electrolyte interface.[53,54] Therefore, in our study, the dense, uniform, and dendrite-free plating morphology is attributed to both the Li-Sn intermetallic compounds and the chloride component in the composite coating.

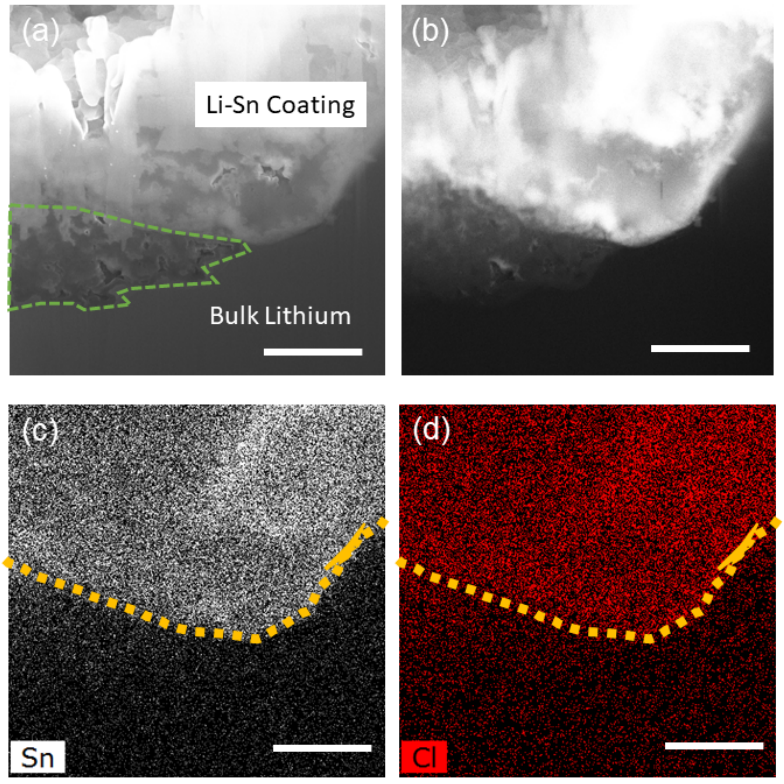

Figure 3.13. (a) Cryo FIB cross-section SEM of Li-Sn coating with lithium plated at a current density of 0.1 mA cm^{-2} for a capacity of 1 mAh cm^{-2}. Plated lithium is outlined in green. Scale bar is 2 μm. (b) Backscattered Electron Detector (BSED) SEM image demonstrated a stark contrast between the plated lithium region and Li-Sn coating while showing similar electron signal between the bulk Li and plated Li. Scale bar is 2 μm. (c) EDX elemental mapping for tin. Scale bar is 2 μm. (d) EDX elemental mapping for chlorine. Scale bar is 2 μm.

For the lower plating current density (0.1 mA cm^{-2}, 1 mAh cm^{-2}), where the applied current was lower than the exchange current density, the Li plating process is more complex than what has been observed previously.[21] To complement the plan-view SEM image in Figure 3.9(a) which showed no indication of Li plating on the surface of the coating, Cryo-FIB SEM was used to probe Li deposition below the surface. By comparing the secondary electron image with the backscattered electron image [Figure 3.13(a-b)], the plated Li region (outlined in green) could be distinguished by both its morphology and composition. The plated Li beneath the Li-Sn coating contained porosity that helped distinguish it from the bulk Li foil. The EDX spectral mapping indicated a lack of tin signals from the region where morphology is different from the bulk Li while the EDX line scan showed an immediate decrease for both the tin and chlorine signals in the plated Li region (Figure 3.14).

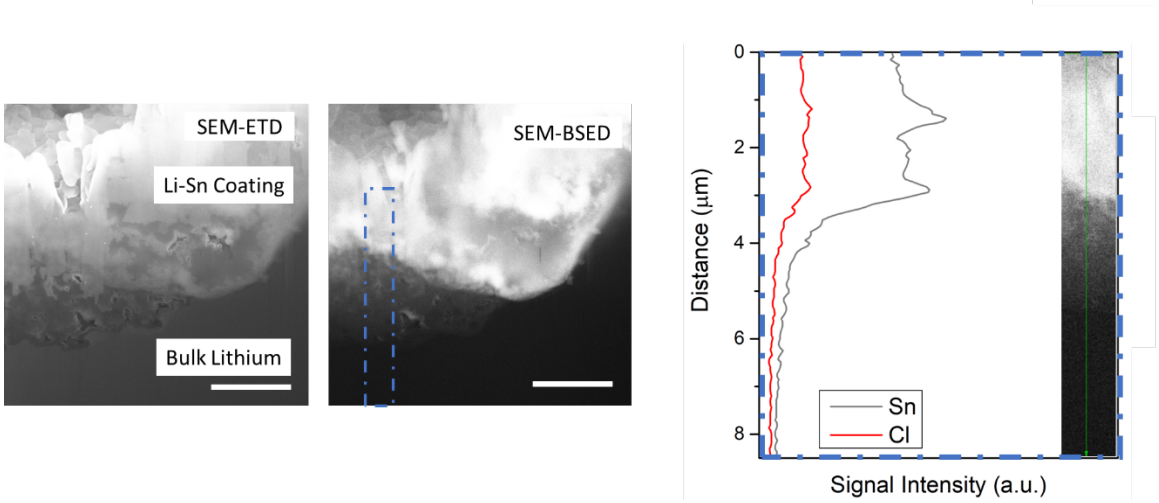

Figure 3.14. EDX line of plated lithium at 0.1 mA cm^{-2}. Scale bar of SEM-ETD image (left) and SEM-BSED image (right) is 2μm.

Similar to the Li plated on top of the coating at the higher current density, the Li plated underneath the coating also contained oxygen and sulfur signals from the electrolyte. The plated Li region underneath the coating in Figure 3.13(a) was found to be less than the theoretical thickness of 4.8 μm. However, other regions within the sample were found to have plated Li thicknesses greater than 4.8 μm (Figure 3.15) indicating that the deposition of Li underneath the Li-Sn is non-uniform.

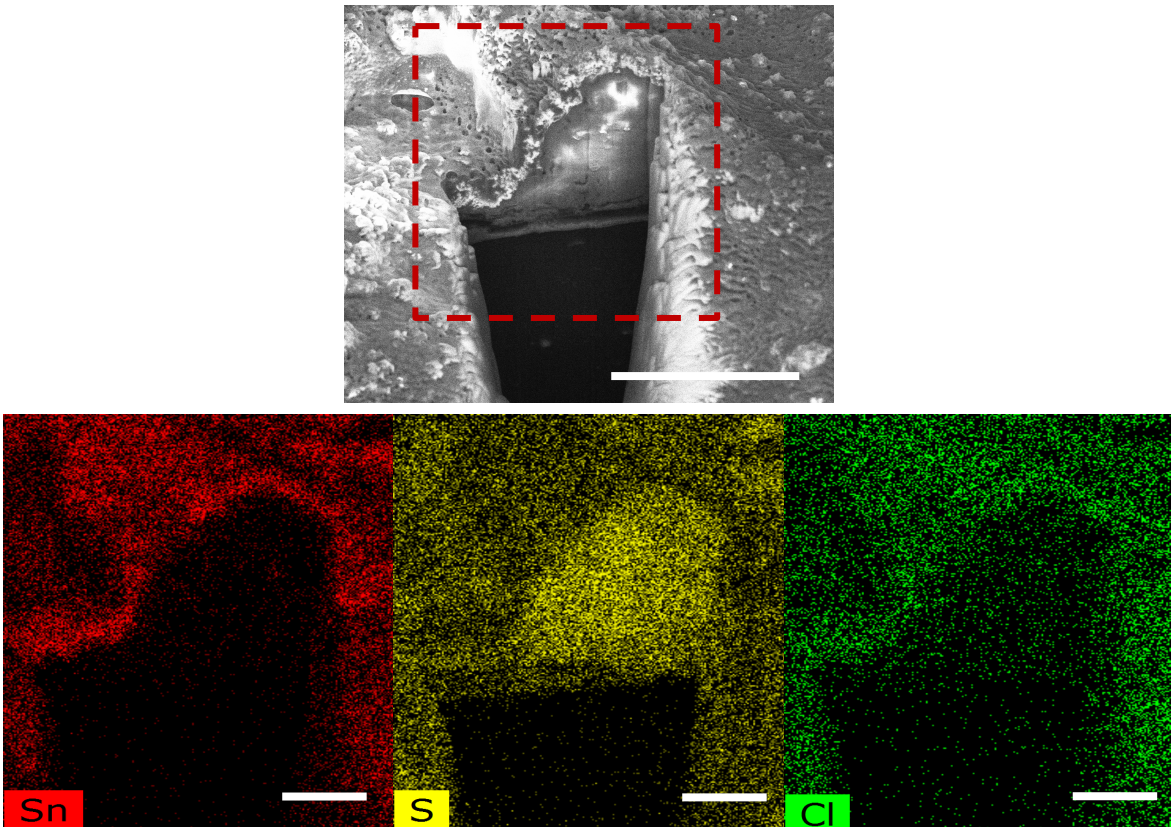

Figure 3.15. Other region where lithium plated underneath coating demonstrating coating's ability to withstand large volume associated with lithium plating. Sulfur signal from electrolyte. SEM image(top) scale bar is 10 μm. EDX spectral map scale bar is 3 μm.

Chapter 3.4. Conclusion

In this work, we investigate the mechanism of Li plating underneath Li-Sn coatings which can serve as a strategy to mitigate dendrite formation. Li-Sn coatings were fabricated directly on lithium foil using a solution-based approach. HRTEM revealed a unique microstructure consisting of both Li-rich intermetallic grains and amorphous chloride regions. The plating kinetics for the Li-Sn coating demonstrated an exchange current twice that of bare lithium indicating enhanced charge transfer kinetics in combination with the ability to stabilize the surface during plating/stripping. We demonstrate that by tuning the plating current density, the lithium deposition

location can be modified. At current densities of 100 μA cm^{-2}, lithium deposition can be observed underneath the coating. At higher current densities of 2 mA cm^{-2}, heterogeneous nucleation of Li on top of the coating becomes more kinetically favorable compared to the diffusion of Li through the coating layer. The results shown here suggest a novel approach for Li dendrite suppression.

Chapter 3.5. References

1. C. Fang, J. Li, M. Zhang, Y. Zhang, F. Yang, J. Z. Lee, M. H. Lee, J. Alvarado, M. A. Schroeder, Y. Yang, B. Lu, N. Williams, M. Ceja, L. Yang, M. Cai, J. Gu, K. Xu, X. Wang, and Y. S. Meng: Quantifying inactive lithium in lithium metal batteries. *Nature* **572**(7770), 511 (2019).
2. C. Fang, X. Wang, and Y. S. Meng: Key Issues Hindering a Practical Lithium-Metal Anode. *Trends Chem.* **0**(0), 1 (2019).
3. X. B. Cheng, R. Zhang, C. Z. Zhao, and Q. Zhang: Toward Safe Lithium Metal Anode in Rechargeable Batteries: A Review. *Chem. Rev.* **117**(15), 10403 (2017).
4. E. Peled: The Electrochemical Behavior of Alkali and Alkaline Earth Metals in Nonaqueous Battery Systems—The Solid Electrolyte Interphase Model. *J. Electrochem. Soc.* **126**(12), 2047 (1979).
5. J. Qian, W. A. Henderson, W. Xu, P. Bhattacharya, M. Engelhard, O. Borodin, and J. G. Zhang: High rate and stable cycling of lithium metal anode. *Nat. Commun.* **6** (2015).
6. J. B. Goodenough and Y. Kim: Challenges for rechargeable Li batteries. *Chem. Mater.* **22**(3), 587 (2010).
7. M. S. Whittingham: Electrical Energy Storage and Intercalation Chemistry. *Science (80-.).* **192**(4244), 1126 (1976).
8. B. D. Adams, J. Zheng, X. Ren, W. Xu, and J. G. Zhang: Accurate Determination of Coulombic Efficiency for Lithium Metal Anodes and Lithium Metal Batteries. *Adv. Energy*

Mater. **8**(7), 1 (2018).

9. D. Aurbach: Review of selected electrode-solution interactions which determine the performance of Li and Li ion batteries. *J. Power Sources* **89**(2), 206 (2000).
10. X. B. Cheng, R. Zhang, C. Z. Zhao, F. Wei, J. G. Zhang, and Q. Zhang: A review of solid electrolyte interphases on lithium metal anode. *Adv. Sci.* **3**(3), 1 (2015).
11. M. D. Tikekar, S. Choudhury, Z. Tu, and L. A. Archer: Design principles for electrolytes and interfaces for stable lithium-metal batteries. *Nat. Energy* **1**(9), 1 (2016).
12. X. Q. Zhang, X. B. Cheng, X. Chen, C. Yan, and Q. Zhang: Fluoroethylene Carbonate Additives to Render Uniform Li Deposits in Lithium Metal Batteries. *Adv. Funct. Mater.* **27**(10), 1 (2017).
13. D. Aurbach, K. Gamolsky, B. Markovsky, Y. Gofer, M. Schmidt, and U. Heider: On the use of vinylene carbonate (VC) as an additive to electrolyte solutions for Li-ion batteries. *Electrochim. Acta* **47**(9), 1423 (2002).
14. C. P. Yang, Y. X. Yin, S. F. Zhang, N. W. Li, and Y. G. Guo: Accommodating lithium into 3D current collectors with a submicron skeleton towards long-life lithium metal anodes. *Nat. Commun.* **6**(May) (2015).
15. Q. Yun, Y. B. He, W. Lv, Y. Zhao, B. Li, F. Kang, and Q. H. Yang: Chemical Dealloying Derived 3D Porous Current Collector for Li Metal Anodes. *Adv. Mater.* **28**(32), 6932 (2016).
16. K. Liu, D. Zhuo, H. W. Lee, W. Liu, D. Lin, Y. Lu, and Y. Cui: Extending the Life of Lithium-Based Rechargeable Batteries by Reaction of Lithium Dendrites with a Novel Silica Nanoparticle Sandwiched Separator. *Adv. Mater.* **29**(4), 1 (2017).
17. G. Zheng, S. W. Lee, Z. Liang, H. W. Lee, K. Yan, H. Yao, H. Wang, W. Li, S. Chu, and Y. Cui: Interconnected hollow carbon nanospheres for stable lithium metal anodes. *Nat. Nanotechnol.* **9**(8), 618 (2014).

18. Y. Chen, Z. Wang, X. Li, X. Yao, C. Wang, Y. Li, W. Xue, D. Yu, S. Y. Kim, F. Yang, A. Kushima, G. Zhang, H. Huang, N. Wu, Y. W. Mai, J. B. Goodenough, and J. Li: Li metal deposition and stripping in a solid-state battery via Coble creep. *Nature* **578**(7794), 251 (2020).

19. G. A. Umeda, E. Menke, M. Richard, K. L. Stamm, F. Wudl, and B. Dunn: Protection of lithium metal surfaces using tetraethoxysilane. *J. Mater. Chem.* **21**(5), 1593 (2011).

20. D. Lin, Y. Liu, W. Chen, G. Zhou, K. Liu, B. Dunn, and Y. Cui: Conformal Lithium Fluoride Protection Layer on Three-Dimensional Lithium by Nonhazardous Gaseous Reagent Freon. *Nano Lett.* **17**(6), 3731 (2017).

21. X. Liang, Q. Pang, I. R. Kochetkov, M. S. Sempere, H. Huang, X. Sun, and L. F. Nazar: A facile surface chemistry route to a stabilized lithium metal anode. *Nat. Energy* **6**, 17119 (2017).

22. Q. Yan, G. Whang, Z. Wei, S.-T. Ko, P. Sautet, S. H. Tolbert, B. S. Dunn, and J. Luo: A Perspective on interfacial engineering of lithium metal anodes and beyond. *Appl. Phys. Lett.* **117**(8), 080504 (2020).

23. F. Guo, C. Wu, H. Chen, F. Zhong, X. Ai, H. Yang, and J. Qian: Dendrite-free lithium deposition by coating a lithiophilic heterogeneous metal layer on lithium metal anode. *Energy Storage Mater.* **24**(April 2019), 635 (2020).

24. L. Luo and A. Manthiram: An Artificial Protective Coating toward Dendrite-Free Lithium-Metal Anodes for Lithium–Sulfur Batteries. *Energy Technol.* **8**(7), 1 (2020).

25. R. Pathak, K. Chen, A. Gurung, K. M. Reza, B. Bahrami, J. Pokharel, A. Baniya, W. He, F. Wu, Y. Zhou, K. Xu, and Q. (Quinn) Qiao: Fluorinated hybrid solid-electrolyte-interphase for dendrite-free lithium deposition. *Nat. Commun.* **11**(1), 1 (2020).

26. A. Anani and R. A. Huggins: Technical Notes Kinetic and Thermodynamic Parameters of Several Binary Lithium. *J. Electrochem. Soc.* **134**(12), 3098 (1987).

27. C. J. Wen and R. A. Huggins: Chemical diffusion in intermediate phases in the lithium-tin system. *J. Solid State Chem.* **35**(3), 376 (1980).

28. M. Wan, S. Kang, L. Wang, H. W. Lee, G. W. Zheng, Y. Cui, and Y. Sun: Mechanical rolling formation of interpenetrated lithium metal/lithium tin alloy foil for ultrahigh-rate battery anode. *Nat. Commun.* **11**(1), 1 (2020).

29. H. Xu, S. Li, C. Zhang, X. Chen, W. Liu, Y. Zheng, Y. Xie, Y. Huang, and J. Li: Roll-to-roll prelithiation of Sn foil anode suppresses gassing and enables stable full-cell cycling of lithium ion batteries. *Energy Environ. Sci.* **12**(10), 2991 (2019).

30. Z. Tu, S. Choudhury, M. J. Zachman, S. Wei, K. Zhang, L. F. Kourkoutis, and L. A. Archer: Fast ion transport at solid-solid interfaces in hybrid battery anodes. *Nat. Energy* **3**(4), 310 (2018).

31. L. Lin, F. Liang, K. Zhang, H. Mao, J. Yang, and Y. Qian: Lithium phosphide/lithium chloride coating on lithium for advanced lithium metal anode. *J. Mater. Chem. A* **6**(32), 15859 (2018).

32. K. Liao, S. Wu, X. Mu, Q. Lu, M. Han, P. He, Z. Shao, and H. Zhou: Developing a “Water-Defendable” and “Dendrite-Free” Lithium-Metal Anode Using a Simple and Promising GeCl4 Pretreatment Method. *Adv. Mater.* **30**(36), 1 (2018).

33. J. F. Moulder, W. F. Stickle, and P. E. Sobol: Handbook of X-Ray Photoelectron Spectroscopy : A Reference Book of Standard Spectra for Identification and Interpretation of XPS Data (Physical Electronics, Inc., Eden Prairie, Minn., 1995).

34. Y. Ozhabes, D. Gunceler, and T. A. Arias: Stability and surface diffusion at lithium-electrolyte interphases with connections to dendrite suppression. *arXiv:1504.05799* 1 (2015).

35. H. Rawson: Inorganic Glass-Forming Systems (Academic Press, London, 1967).

36. G. Rack: The binary system SnCl2-LiCl. *Centr. Min. Geol.* **326**–**8** (1914).

37. Phase Equilibria Diagrams Online Database (NIST Standard Reference Database 31). *Am. Ceram. Soc. Natl. Inst. Stand. Technol.* Figure Number 3090 (2020).

38. M. Shojiya, M. Takahashi, R. Kanno, Y. Kawamoto, and K. Kadono: Optical transitions of Er3+ ions in ZnCl2-based glass. *J. Appl. Phys.* **82**(12), 6259 (1997).

39. K. Annapurna, R. N. Dwivedi, P. Kundu, and S. Buddhudu: Fluorescence properties of Sm3+: ZnCl2-BaCl2-LiCl glass. *Mater. Res. Bull.* **38**(3), 429 (2003).

40. A. J. Easteal, E. J. Sare, C. T. Moynihan, and C. A. Angell: Glass-transition temperature, electrical conductance, viscosity, molar volume, refractive index, and proton magnetic resonance study of chlorozinc complexation in the system ZnCl2+LiCl+H2O. *J. Solution Chem.* **3**(11), 807 (1974).

41. A. J. Bard and L. R. Faulkner: Electrochemical Methods: Fundamental and Applications, 2nd Editio (John Wiley & Sons, New York, NY, 2001).

42. D. T. Boyle, X. Kong, A. Pei, P. E. Rudnicki, F. Shi, W. Huang, Z. Bao, J. Qin, and Y. Cui: Transient Voltammetry with Ultramicroelectrodes Reveals the Electron Transfer Kinetics of Lithium Metal Anodes. *ACS Energy Lett.* **5**(3), 701 (2020).

43. G. Bieker, M. Winter, and P. Bieker: Electrochemical in situ investigations of SEI and dendrite formation on the lithium metal anode. *Phys. Chem. Chem. Phys.* **17**(14), 8670 (2015).

44. I. S. Kang, Y.-S. Lee, and D.-W. Kim: Improved Cycling Stability of Lithium Electrodes in Rechargeable Lithium Batteries. *J. Electrochem. Soc.* **161**(1), A53 (2014).

45. C. Wei, H. Fei, Y. An, Y. Tao, J. Feng, and Y. Qian: Uniform Li deposition by regulating the initial nucleation barrier: Via a simple liquid-metal coating for a dendrite-free Li-metal anode. *J. Mater. Chem. A* **7**(32), 18861 (2019).

46. K. Park and J. B. Goodenough: Dendrite-Suppressed Lithium Plating from a Liquid Electrolyte via Wetting of Li3N. *Adv. Energy Mater.* **7**(19), 1 (2017).

47. H. Jung, B. Lee, M. Lengyel, R. Axelbaum, J. Yoo, Y. S. Kim, and Y. S. Jun: Nanoscale: In situ detection of nucleation and growth of Li electrodeposition at various current densities. *J. Mater. Chem. A* **6**(11), 4629 (2018).

48. F. Sagane, K. I. Ikeda, K. Okita, H. Sano, H. Sakaebe, and Y. Iriyama: Effects of current densities on the lithium plating morphology at a lithium phosphorus oxynitride glass electrolyte/copper thin film interface. *J. Power Sources* **233**, 34 (2013).

49. K. I. Popov, S. S. Djokić, and B. N. Grgur: in *Fundam. Asp. Electrometall.* (Springer US, Boston, MA, 2002), pp. 29–100.

50. A. Maraschky and R. Akolkar: Mechanism Explaining the Onset Time of Dendritic Lithium Electrodeposition via Considerations of the Li + Transport within the Solid Electrolyte Interphase . *J. Electrochem. Soc.* **165**(14), D696 (2018).

51. J. Z. Lee, T. A. Wynn, M. A. Schroeder, J. Alvarado, X. Wang, K. Xu, and Y. S. Meng: Cryogenic Focused Ion Beam Characterization of Lithium Metal Anodes. *ACS Energy Lett.* **4**(2), 489 (2019).

52. D. R. Ely and R. E. García: Heterogeneous Nucleation and Growth of Lithium Electrodeposits on Negative Electrodes. *J. Electrochem. Soc.* **160**(4), A662 (2013).

53. Y. Lu, Z. Tu, and L. A. Archer: Stable lithium electrodeposition in liquid and nanoporous solid electrolytes. *Nat. Mater.* **13**(10), 961 (2014).

54. Q. Pang, X. Liang, I. R. Kochetkov, P. Hartmann, and L. F. Nazar: Stabilizing Lithium Plating by a Biphasic Surface Layer Formed In Situ. *Angew. Chemie - Int. Ed.* **57**(31), 9795 (2018).

Chapter 4. Temperature-dependent reaction pathways in FeS_2: reversibility and the electrochemical formation of Fe_3S_4

As mentioned in chapter 1, the specific capacity of a material depends on the number of electrons undergoing redox and its gravimetric weight. Conversion materials undergo multielectron redox enabling access to higher specific capacities. FeS_2 is a conversion cathode offering both high specific capacity and sustainability, being the most abundant metal sulfide on earth. However, the complex reaction pathways in the rechargeable system presents many discrepancies in both the intermediate and charge products across the past few decades. The present study has used a variety of characterization techniques to determine the products and reaction pathways involved in the rechargeable Li-FeS_2 system. We revisit both the initial lithiation and subsequent cycling of FeS_2 employing an ionic liquid electrolyte to investigate the intermediate and final charge products formed under varying thermal conditions (room temperature to 100 ºC). The detection of Li_2S and hexagonal FeS as the intermediate phases in the initial lithiation and the electrochemical formation of greigite, Fe_3S_4, as a charge product in the rechargeable reaction differ significantly from previous reports. The conditions for Fe_3S_4 formation are shown to be dependent on both the temperature (~60 ºC) and the availability of sulfur to drive a FeS to Fe_3S_4 transformation. Upon further cycling, Fe_3S_4 transforms to a lower sulfur content iron sulfide phase, a process which coincides with the loss of sulfur based on the new reaction pathways established in this work. The connection between sulfur loss, capacity fade, and charge product composition highlights the critical need to retain sulfur in the active material upon cycling.

4.1 Introduction

With the goal of net zero carbon emissions by 2050 in the US, there has been a significant move towards advancing fully electric and hybrid vehicles.[1,2] However, the intercalation chemistries that currently power electric vehicles have limited capacity owing to their host-limited redox processes.[3,4] Further, the rising demand for lithium-ion batteries underscores the equally critical need for finding sustainable alternatives to replace cobalt and nickel-based cathodes.[5–7] Conversion materials present an attractive path towards obtaining higher energy density batteries enabled by their multi-electron redox processes. In particular, pyrite, a cubic form of FeS_2, presents a sustainable path to high energy density batteries given its high theoretical capacity (894 mAh g^{-1}) and designation as the most abundant metal sulfide on earth.[8,9] FeS_2 has been commercialized as a primary battery cathode, where upon lithiation, pyrite undergoes an irreversible reaction.[10–12] That is, once cubic-FeS_2 (c-FeS_2) is lithiated to 1 V, the pyrite phase is not recovered on recharge. Therefore, the rechargeable FeS_2 system is starkly different from its primary battery counterpart.[10,13] While the end discharge products, Fe^0 and Li_2S, are generally agreed upon, the presence of multiple reactions along with the complexity of the iron-sulfur phase diagram[14] has made the identification of intermediates and charge products challenging. Even after decades of research, there exist discrepancies in interpreting the reaction pathways of both the initial[10,12,13] and subsequent cycling[10–12,15] of FeS_2. Despite these discrepancies, recent research has focused less on reconciling the differences in the reaction pathways[10–12,15] and more towards improving the performance of FeS_2 through engineering approaches that increase the electronic conductivity,[16,17] reduce polysulfide shuttling,[11,15] and minimize the Li^+ diffusion path.[18–20] While engineering approaches have improved performance, incomplete mechanistic insight hinders targeted approaches to address fundamental limitations in reversibility and kinetics inherent to the FeS_2 system.

In the present work, an ionic liquid electrolyte, 1M lithium bis(fluorosulfonyl)imide (LiFSI) in 1-butyl-1-methylpyrrolidinium bis(trifluoromethanesulfonyl)imide ($PYR_{14}TFSI$), is utilized in the electrochemical experiments for two reasons: 1) to study the FeS_2 system under a large temperature range (room temperature to 100 ºC) which cannot be achieved using common organic electrolytes[21] and 2) to take advantage of the lower solubility of polysulfides in ionic liquid electrolytes[15] in order to reduce the influence of polysulfide shuttling. Through a suite of characterization techniques, we establish that the intermediates formed in the first plateau of the initial lithiation at elevated temperatures consist of two phases, Li_2S and hexagonal FeS (h-FeS), in contrast to commonly accepted but elusive Li_2FeS_2.[10,13] Based on our revised initial lithiation reaction, we draw the connection between c-FeS_2 and that of h-FeS studied previously by Goodenough.[22] The similar reaction pathways and charge products formed in these two systems have received little attention despite their importance in capacity and cycling.[23,24]

The delithiation reaction is divided into four distinct regions. Our results provide context for the discrepancies in charge products reported since the 1980's (Table 4.1). The most significant result presented here is the electrochemical formation of greigite, Fe_3S_4, as a charge product of FeS_2. We establish that its formation is dependent both on temperature and the availability of sulfur produced in the upper conversion reaction at ~2.4 V. The loss of active sulfur during cycling, attributed to polysulfide shuttling, is responsible for the loss of Fe_3S_4 after the first few charge cycles, leading to a charge mechanism similar to that observed at room temperature. Once greigite is no longer produced, the reversible formation of a nanocrystalline FeS mackinawite on charge becomes the dominating iron sulfide phase in battery operation. The insights presented here underscore the critical importance of sulfur retention in the active material in addition to the dynamic nature of charge product formation in FeS_2. These features are also likely to impact the emerging interest in solid-state FeS_2 systems.

Table 4.1. Survey of Charge Products Reported for FeS_2

Charge Products at 3 V	Temperature	Slurry Ratio	Electrolyte	Cell Format	Technique	Reference	Year Published
FeS_y (pyrrhotite) S	RT 60 ºC	**94**:4:2 FeS_2:PEO:EC	1M $LiAsF_6$ in PC:EC (1:1 vol)	Two electrode in-situ cells	XRD Mossbauer	[10]	1990
t-FeS (mackinawite) S	RT 60 ºC	**60**:30:10 FeS_2: Super P: PVDF	1M LiTFSI in DOL: DME (1:1 vol)	Coin cell	XRD HRTEM	[12]	2020
o-FeS_2 **(marcasite) $FeS_{8/7}$ S**	RT	**60**:20:20 FeS_2: Acetylene Black: PVDF	0.6M LiTFSI PYR13TFSI 1M $LiPF_6$ in EC:DMC (1:1 vol)	Coin Cell	FIB + HRTEM	[15]	2014
o-FeS_2 (marcasite) $FeS_{8/7}$ S	30-60 ºC	31.25:62.5:6.25 FeS_2:Solid Electrolyte: Carbon Black	amorphous $77.5Li_2S$:$22.5P_2S_5$	Solid State Cell	FIB + HRTEM	[11]	2013
c-FeS_2 $Fe_{1-x}S$	410 ºC	Ratio not provided	LiCl-rich molten electrolyte	Three electrode custom built molten electrolyte cell with Li/Al Counter and Ref electrode	XRD	[39]	1982
Fe_3S_4 S t-FeS_y y=0.9-1 (Mackinawite)	40-100 ºC	**80**:10:10 FeS_2: Super P: PVDF	1M LiFSI PYR_{14}TFSI	Coin Cell	XRD XAS UV-Vis	**This Work**	2022

Chapter 4.2. Experimental Methods

Materials and Electrode Preparation

As received FeS_2 powder (99.9%, Sigma Aldrich) was ball milled for 6 hours at 1000 rpm using a Fritsch Pulverisette 7 Premium Line Planetary Micro Mill using a 20 mL stainless steel Fritsch grinding bowl and 3 mm stainless steel Fritsch media. The resulting FeS_2 powder contained both micron and nano sized particles. FeS (99.9%, Sigma Aldrich) and Li_2S (99.9%,

Alfa Aesar) was used as received and stored in an argon glovebox (<1 ppm O_2 and <1 ppm H_2O). Lithium bis(fluorosulfonyl)imide salt (99.9%, Alfa Aesar) was dried on a Schlenk line at 110 ºC overnight prior to pumping into the glovebox and mixing into 1-Butyl-1-methylpyrrolidinium bis(trifluoromethanesulfonyl)imide (99.9%, Solvionic). For the FeS:Li_2S (1:1 mol) composites, equal molar amounts of Li_2S and FeS powder were loaded into the ball mill jar inside the glovebox, transferred out using an air free enclosure, and subsequently ball milled for 5 hours at 500 rpm in a Retsch PM 100 planetary ball mill. The ball mill jar was transferred back into the glovebox for slurry fabrication. Slurry electrodes in this study were made by mixing the active material (ball-milled FeS_2, FeS, FeS:Li_2S (1:1 mol), or Li_2S), Super P (Alfa Aesar), and PVDF (polyvinylidene fluoride) Binder (Kynar Flex 2801) in an 80:10:10 ratios by weight, respectively, in N-methyl-2-pyrrolidone (NMP, Sigma Aldrich), using a mortar and pestle to produce a homogeneous slurry. Slurries were doctor bladed onto a carbon-coated aluminum foil current collector (MTI Corp.) FeS_2 slurries were made outside the box and dried in a vacuum oven overnight at 120 °C prior to pumping into an Argon glove box (<1 ppm O_2 and <1 ppm H_2O, VAC) for coin cell assembly.

Materials Characterization

Scanning electron microscope (SEM; FEI Nova NanoSEM230) images were obtained using an accelerating voltage of 10.0 kV and at a working distance of ~5 mm. X-ray Diffraction (XRD) was performed using a PANalytical X'Pert Pro diffractometer using a Cu Kα (λ = 1.5418 Å) source. Samples were sealed in Kapton inside the glovebox and transferred into a glass vial to minimize air exposure. XRD patterns were recorded in the range of $20° < 2\theta < 70°$ using a voltage of 45 kV, and a current of 40 mA. X-ray photoelectron spectroscopy (XPS; Kratos Axis Ultra) with a monochromatic aluminum X-ray source was performed using a voltage of 10 kV and emission current of 10 mA on cycled electrodes. The electrodes were removed from a coincell inside the glove box, rinsed in dimethyl carbonate (DMC), and dried in the glovebox prior to loading into an

air-free transfer carrier. The data was processed in Casa XPS software using a peak calibration of 284.8 eV for adventitious carbon peak and a Shirley background for the fitting. UV-Vis spectroscopy was performed using the same setup as a previously reported.[25] To characterize sulfur and polysulfides as a function of cycling, two coin cells were charged up to 3 V (C/20, 60 ºC) for 1 or 5 cycles. The coin cells were decrimped and each component (lithium anode, separator, and FeS_2 electrode) was left to sit in separate vials of 1,3-dioxolane (DOL) for 24 h to extract adsorbed polysulfides (PS) or sulfur in each component. UV-vis sample prep and spectral collection were conducted inside of a glovebox with <1 ppm of water and oxygen. Each UV-vis spectrum was background subtracted for pristine DOL.

X-ray absorption spectroscopy (XAS) of the iron K edge was conducted at beam line BL17C1 of National Synchrotron Radiation Research Center (NSRRC, Hsinchu, Taiwan) with ring energy of 1.5 GeV and emission current of 300-360 mA. The data was collected from 6.9 to 7.9 keV with a 40-minute duration, with a reference spectrum of Fe foil measured simultaneously. For the powder reference samples (FeS_2 and FeS), 18 mg of powder was spread onto a 1 cm x 6 cm strip of Kapton tape to achieve an areal loading of 3 mg cm^{-2}. For cycled electrodes 10 mm electrodes were cycled in a coin cell, disassembled, rinsed in DMC to remove ionic liquid, and then pressed onto Kapton tape to transfer the electrode slurry off the Al current collector and onto the tape. The area loading for each electrode was around ~1.5 mg cm^{-2}. Measurements for each sample were performed three times, and the spectra were merged together for further analysis. For data processing, the obtained XAS spectra were calibrated with the Fe foil reference and analyzed by Athena using the intensity normalization and curve merging/fitting functions. The experimental χ(k) in the Extended X-ray Absorption Fine Structure (EXAFS) region was weighted by k3 and Fourier transformed into r-space for fitting by Artemis, and the parameters are extracted from the iron sulfide standards (FeS, FeS_2, and Fe_3S_4).

Electrochemical Characterization

All electrochemical testing was conducted using two electrode 2032 coin cells (MTI Corp). Coin cells were made using a 3/8" diameter working electrode, ½" diameter lithium counter electrode, and a 14 µm Celgard Trilayer separator containing 50 µL of 1M Lithium bis(fluorosulfonyl)imide (LiFSI) in 1-Butyl-1-methylpyrrolidinium bis(trifluoromethanesulfonyl)imide ($PYR_{14}TFSI$) as the electrolyte. The active mass loading used in this study were ~1-1.5 mg cm^{-2}. All electrochemical testing was performed on a Biologic VMP3. Galvanostatic lithiation/delithiation tests were performed at a C/20 (unless specified otherwise) based on the theoretical capacity of FeS_2, 894 mAh g^{-1}. Galvanostatic intermittent titration technique (GITT) was performed using a C/20 pulse for 20 minutes followed by a 4-hour rest period.

Chapter 4.3. Results and Discussion

Chapter 4.3.1. The Irreversible First Cycle Lithiation

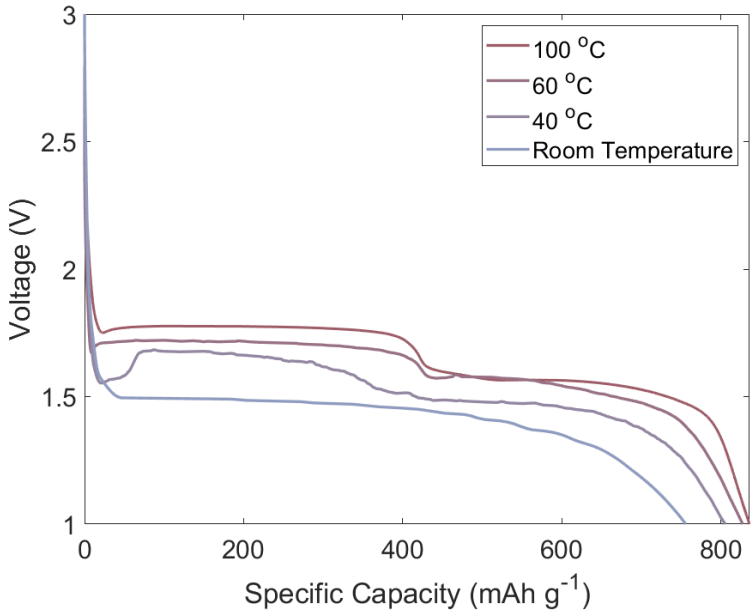

Figure 4.1. Initial lithiation of FeS_2 at various temperatures in 1 M LiFSI $PYR_{14}TFSI$ at a rate of C/20.

The initial lithiation of c-FeS_2 is an irreversible reaction in that c-FeS_2 is not recovered upon charge.[10,11,13] The crystal structure (space group: Pa-3) of c-FeS_2 [Fe^{2+}][S_2^{2-}] is a rock salt structure with the Fe^{2+} cations in the Na^+ sites and the S_2^{2-} sulfur dimers, oriented in the <111> direction, located at the Cl^- sites. Typically, at room temperature, the electrochemical signature of the initial lithiation can be described as a single plateau (~1.5 V) (Figure 4.1, blue trace). However, at elevated temperatures (≥40 ºC)[10–12] or reduced diffusion distances (thin films or nanoparticles),[26] a two plateau signature is revealed, indicating a two-step lithiation reaction (Figure 4.1, pink trace). The most commonly cited reaction pathway ascribes the first plateau to the formation of Li_2FeS_2 and the second plateau to the conversion of Li_2FeS_2 to Li_2S and Fe^0.[10] However, identification of the Li_2FeS_2 phase has not been detected by X-ray diffraction (XRD), so amorphous Li_2FeS_2 was proposed as the intermediate.[17–19,27–29] In addition, there have been reports of other non-lithiated intermediates including hexagonal $Fe_{1-x}S$[30,31] and, more recently, tetragonal FeS.[12] From a more general perspective, the two plateau lithiation can be categorized as anion redox in the first plateau, whereby the S-S dimer (S_2^{2-}) breaks to form a sulfide (S^{2-}), followed by cation redox in the second plateau in which the Fe^{2+} is reduced to elemental Fe^0.[30–32] The Fe^0 formed upon discharge has been characterized as clusters of Fe exhibiting local disorder.[32,33]

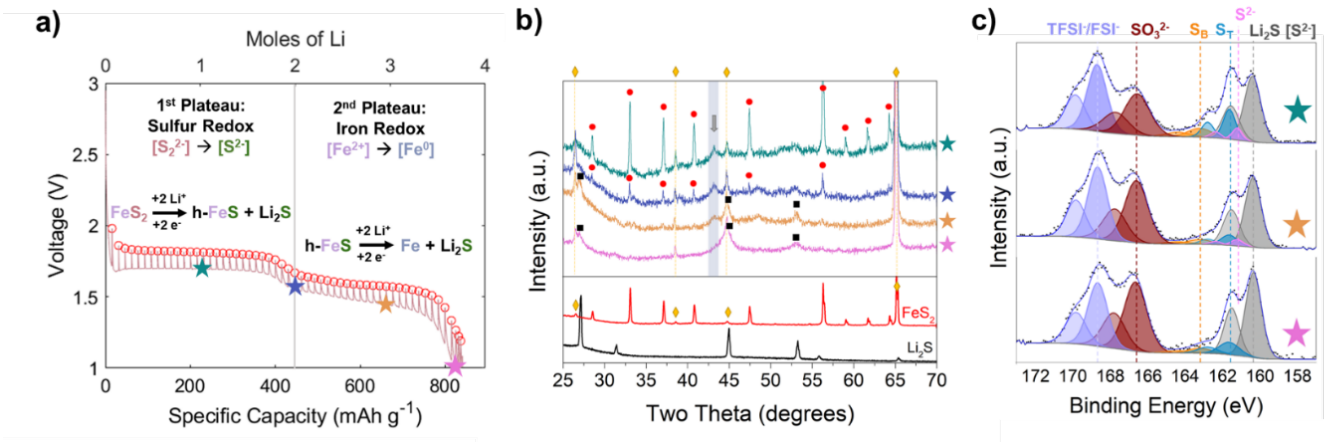

Figure 4.2. Initial Lithiation of FeS_2 at 60ºC. **a)** Open circuit potential (OCP) of the initial lithiation of FeS_2 (open red circles) obtained through GITT of FeS_2 at 60ºC. The colored stars serve as indicators for the points at which XRD and XPS were collected. **b)** *ex-situ* XRD of the initial lithiation of FeS_2. From top to bottom, the XRD scans show the mid first plateau (~1 mol Li), end of first plateau (1.6 V), mid second plateau, and full discharge (1 V). A pristine FeS_2 electrode (red) and Li_2S (black) powder is provided for reference. Red circles, black squares, and yellow diamonds represent c-FeS_2, Li_2S, aluminum current collector peaks, respectively. The grey shaded region highlights the formation of a nanocrystalline h-FeS which is produced in the first plateau and consumed in the second plateau. **c)** *Ex-situ* XPS of initial lithiation of FeS_2 at mid first plateau, mid second plateau, and full discharge (1 V). S_T and S_B refer to the terminal and bridging sulfurs, respectively, of lithium polysulfides.

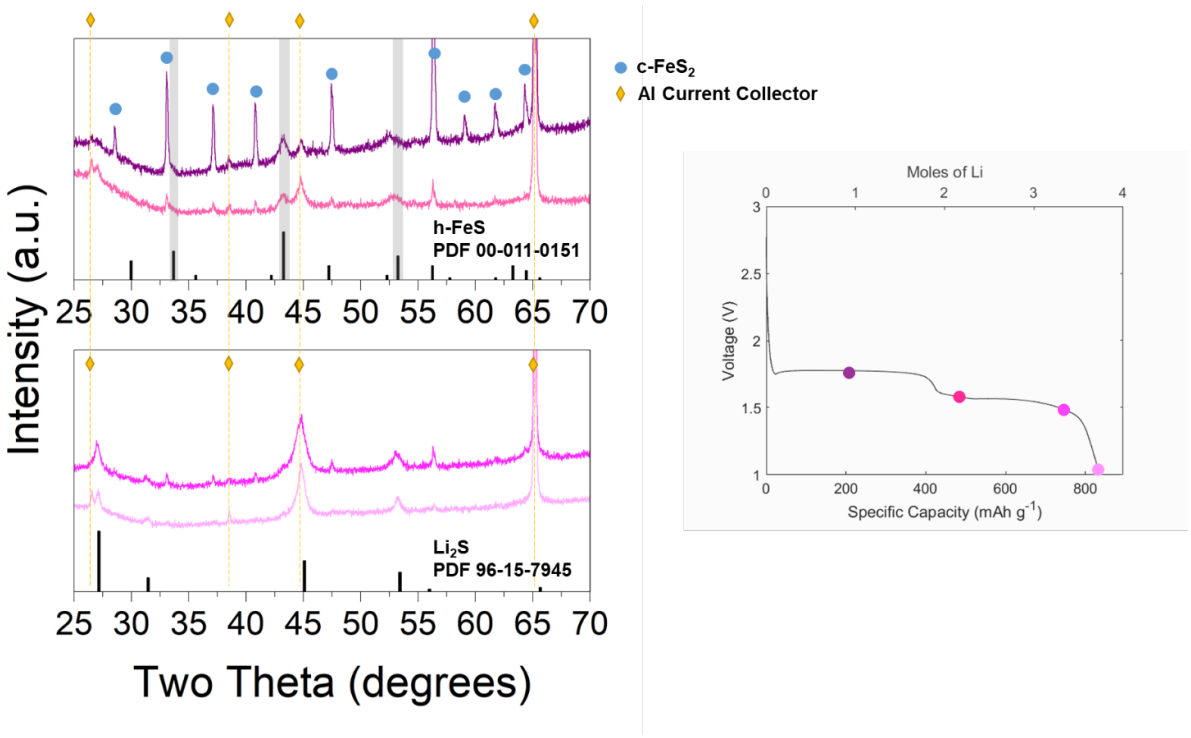

Figure 4.3. *Ex-situ* XRD of initial lithiation of FeS_2 at 100 ºC in 1M LiFSI $PYR_{14}TFSI$ at a C-rate of C/20. Colored circles on the lithiation profile on the right indicate approximate locations for the *ex-situ* XRD scans shown on the left.

The results described here are based on the lithiation of FeS_2 at 60 ºC, as the clear plateau distinctions enable different intermediate species to be identified (Figure 4.2a). *Ex situ* XRD in the first lithiation plateau (~0-2 mol Li) shows the emergence of a broad peak around 43º corresponding to the highest intensity diffraction peak of hexagonal-structured FeS (h-FeS) (Figure 4.2b; highlighted by the gray shaded region). To better elucidate the formation of h-FeS, XRD was repeated on a cell cycled at 100 ºC where the second highest intensity peak at 52.5 º can also be observed (Figure 4.3). The broad diffraction peak indicates the nanocrystalline nature of electrochemically formed h-FeS. To further confirm the formation of h-FeS, k3-weighted Fe Extended X-ray Absorption Fine Structure (EXAFS) spectra extracted from X-ray absorption

spectroscopy (XAS) for the *ex-situ* cycled electrode at 1.6 V was fit with the theoretical crystal h-FeS standard (Figure 4.4) for the first two coordination shells (Fe-S and Fe-Fe). Taking into account the nanocrystallinity of the electrochemically-formed h-FeS at 60 ºC, the fit shows good agreement (R-factor = 0.01405) between the Fe environment in the experiment and the h-FeS standard. Upon further lithiation into the second plateau (~3-4 mol Li; Figure 4.2, orange and pink stars), h-FeS is progressively consumed to form the final state of Fe and Li_2S, as demonstrated by the decrease of the peak at 43° (Figure 4.2b).[10]

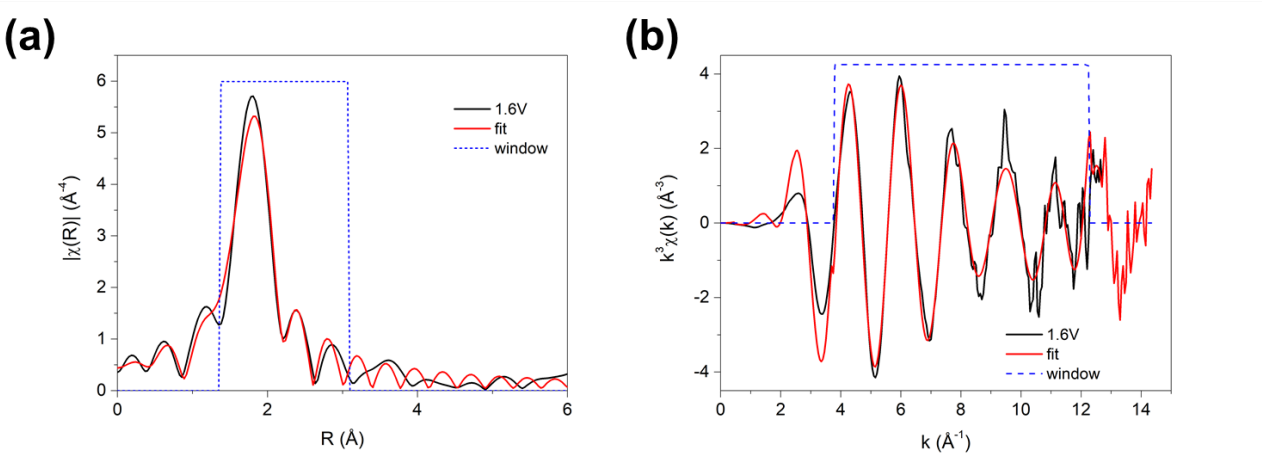

Figure 4.4. EXAFS of FeS_2 at 1.6V of the first lithiation fit to the first two coordination shells (Fe-S and Fe-Fe). k3-weighted EXAFS spectrum (black) and fit (red) of h-FeS at 1.6V in **a)** real space and **b)** k space.

The detection of a non-lithiated iron sulfide (h-FeS) intermediate suggests that in the first plateau region, a lithium sulfide species accompanies the formation of the iron sulfide. To confirm the formation of Li_2S in the first plateau, XPS was utilized to probe the surface of the electrode. *Ex-situ* XPS confirms the presence of Li_2S (160.2 eV)[34,35] in the first plateau [223 mAh/g /~1 mol of Li] (Figure 4.2c, teal star). In addition to the presence of Li_2S, an S^{2-} signal from h-FeS can also be observed (161.2 eV).[14] As lithiation continues into the second plateau region (Figure 4.2c, orange and pink stars), the relative peak ratio between Li_2S (160.2 eV) and FeS (161.2 eV)

increases as h-FeS undergoes a conversion reaction to form Li_2S and Fe^0. In addition to the presence of Li_2S and h-FeS, two additional sets of peaks corresponding to bridging (S_B) (163.2 eV)[35,36] and terminal (S_T) (161.3 eV)[35,36] sulfurs, commonly associated with polysulfides, were found to provide the best fit for the XPS spectra. Though typically not expected to form during the first lithiation, the low polysulfide species signal can be partly explained by the solubility of sulfides in many electrolytes.[12] Another possibility is that Li_2S formation in the first plateau is facilitated through polysulfide intermediates which have recently been detected during the first lithiation of FeS_2 under both electrochemical and chemical lithiation conditions.[25]

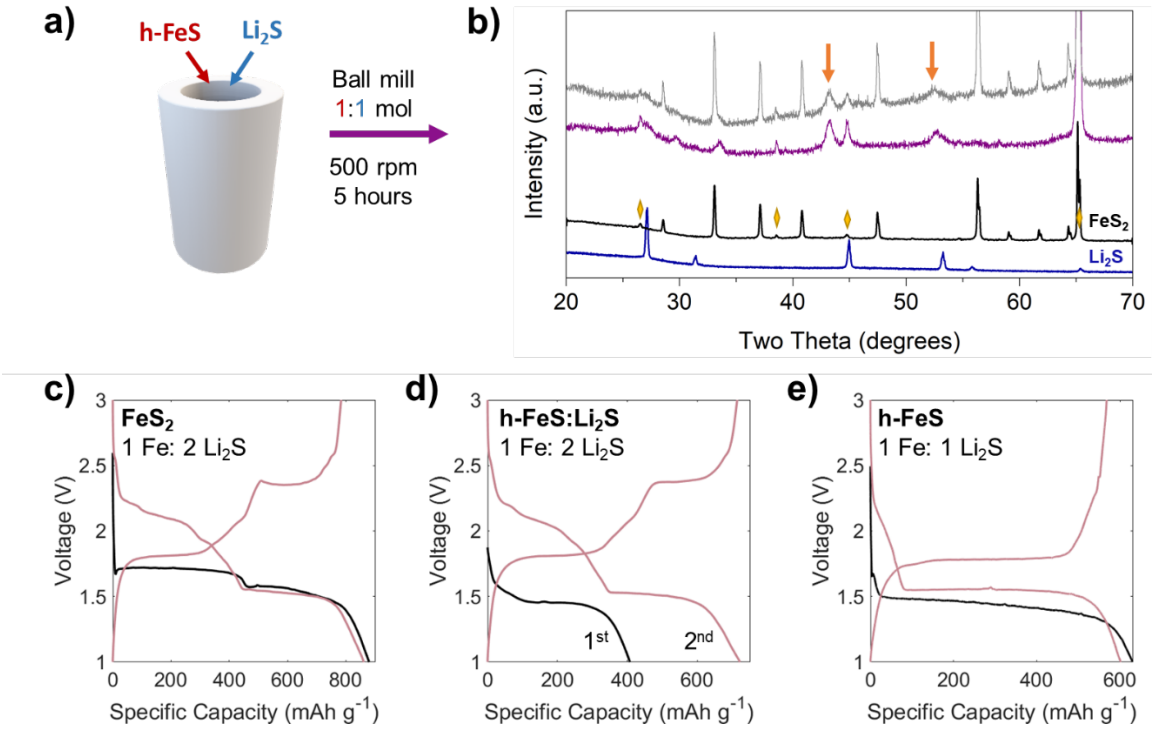

Figure 4.5. Comparison of h-FeS:Li_2S (1:1 mol) to FeS_2 and h-FeS. a) Graphic of the ball milling process. Li_2S and h-FeS powder were added in 1:1 mole stoichiometries and mixed at 500 rpm for 5 hours. b) XRD comparison of ball milled h-FeS:Li_2S (1:1 mol) electrode (gray) compared to an FeS_2 electrode lithiated half way into the first plateau (purple). Orange arrows indicate peak positions for h-FeS diffraction peaks. FeS_2 (black) and Li_2S (blue) powder references are provided

below. Yellow diamonds represent Al current collector diffraction peaks. c-e) 60ºC initial lithiation (black) and rechargeable galvanostatic profiles (pink) of (c) FeS_2, (d) h-FeS:Li_2S, and (e) h-FeS.

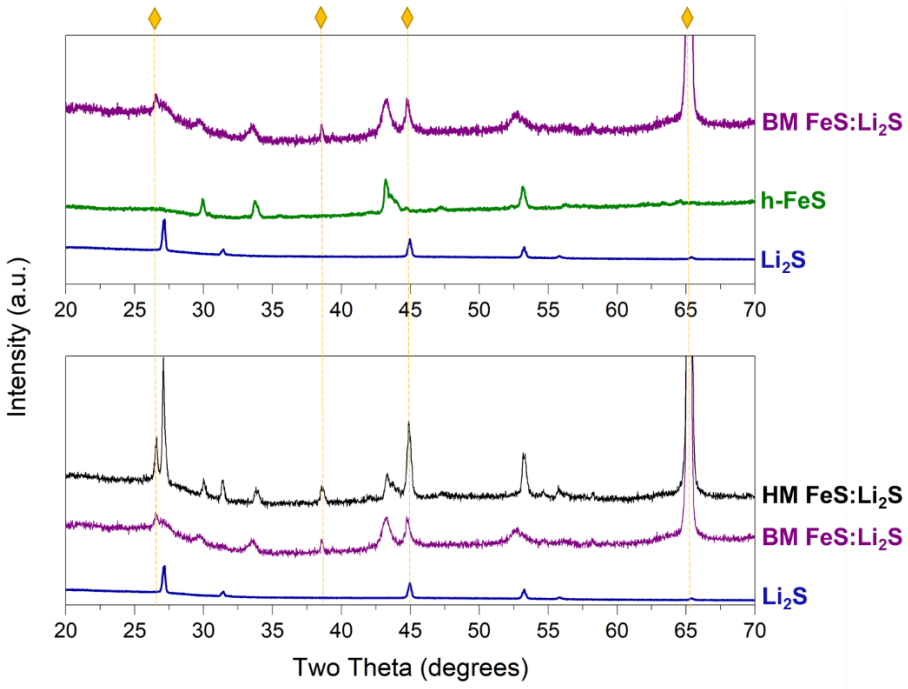

Figure 4.6. Top: XRD of a ball milled (BM) FeS:Li_2S (1:1 mol) electrode (purple) along with the individual h-FeS (green) and Li_2S (blue) powders. Bottom: Comparison of a ball milled composite electrode (purple) with a hand mixed (HM) electrode (black). Li_2S reference shown in blue.

The detection of h-FeS and Li_2S as the intermediates formed in the first plateau raises the question of whether a composite of the two produces an electrochemically-equivalent system to FeS_2. To address this question, composite powders were produced by ball milling h-FeS and Li_2S powders in 1:1 mole ratios (Figure 4.5a). XRD of the ball milled h-FeS:Li_2S (1:1 mol) electrode features peak positions and breadths similar to those formed electrochemically upon lithiating c-FeS_2 (Figure 4.5 b). We note that ball milling of the two powders is necessary to reduce the size of Li_2S (Figure 4.6) which otherwise remains electrochemically inactive due to its low electronic (~10^{-9} S cm^{-1}) and ionic conductivity (~10^{-13} S cm^{-1}).[37] Without the initial conversion of FeS_2 (Figure

4.5c black trace), the h-FeS:Li_2S system demonstrates a lower initial lithiation capacity (Figure 4.5d, black trace); however, in subsequent cycles, near identical (dis)charge curves are identified for FeS_2 and the h-FeS:Li_2S mixture, both featuring two conversion plateaus and a sloped intermediate region. (Figure 4.5 c-d, pink traces). In contrast, pure h-FeS, without the additional Li_2S, exhibits a two-electron redox process and features one conversion plateau (Figure 4.5e). The appearance of an upper conversion plateau is exhibited by systems containing more Li_2S (1 Fe: 2 Li_2S) as is the case with both c-FeS_2 and h-FeS:Li_2S. In a later section, we show that this upper redox plateau represents Li_2S redox (*vide infra*). The ability to physically create an electrochemically equivalent system to FeS_2 further supports the intermediates identified in this work and provides future direction towards using the discharge products, Li_2S and Fe, to produce an anode-free, iron-sulfide-based battery.

In summary, our lithiation results at 60°C indicate the formation of two intermediate species, h-FeS and Li_2S, in the first plateau. While Li_2S was previously thought to form only in the second plateau, we provide evidence for its formation in the first plateau from the conversion of c-FeS_2 into h-FeS and Li_2S (Equation 4.1). The formation of Li_2S continues in the second plateau from the reduction of h-FeS to form Fe^0 and Li_2S (Equation 4.2). In the context of understanding the rechargeable FeS_2 system, the initial lithiation has received relatively little attention. However, the discovery of these new intermediates in the initial lithiation process provides new insight with regard to the rechargeable redox processes.

First plateau: $FeS_2 + 2\ Li^+ + 2e^- \rightarrow$ h-FeS + Li_2S (Eqn. 4.1)

Second plateau: h-FeS + $2\ Li^+ + 2e^- \rightarrow Fe^0 + Li_2S$ (Eqn. 4.2)

Chapter 4.3.2. Delithiation of the FeS_2 System (Rechargeable Reaction)

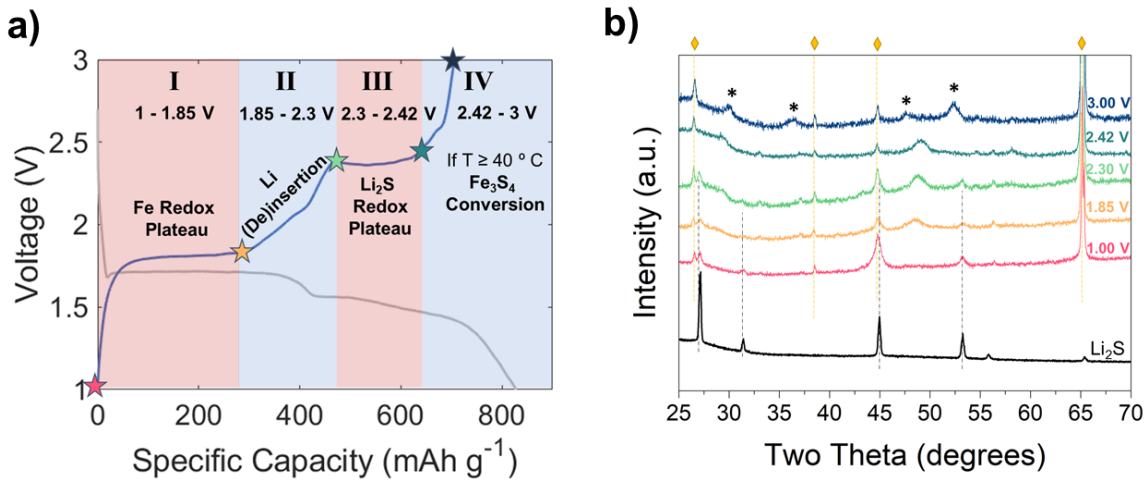

Figure 4.7. Delithiation of FeS_2 at 60ºC. a) Galvanostatic curves of the first lithiation (gray) and delithiation (blue) of FeS_2 cycled at C/20 in 1 M LiFSI PYR14TFSI. Colored stars correspond to key points for ex-situ XRD. Regions I-IV correspond to the Fe redox plateau, Li (de)insertion, Li_2S redox plateau, and Fe_3S_4 conversion regions, respectively. b) ex-situ XRD of initial delithiation of FeS_2 in addition to a Li_2S reference pattern (black). Black asterisks indicate Fe_3S_4 diffraction peaks. Figure S6 provides an expanded view focusing on the intermediate potentials.

There is general agreement that once the Li-FeS_2 system has been discharged (lithiated) to 1.0 V, c-FeS_2 does not reform on charging. The electrode does charge, however, discrepancies exist regarding both the intermediates[10,30,32] and final charge products formed when the Li-FeS_2 system recharges (Table 4.1).[10–12,15] The lack of agreement across literature conveys the complexity of iron sulfide phases at lower temperatures which consist of various compositions, polymorphs, amorphous and metastable phases.[8,14] The current literature on the charge products for FeS_2 vary within the same temperature range indicating that temperature alone cannot account

for the differences in charge products reported in the literature (Table 4.1). Our results clearly indicate that after the first lithiation, c-FeS_2 is no longer formed as a charge product and that the reversible electrochemical properties result from the formation of other iron sulfide phases. To better identify the evolution of the iron sulfide phases, we separate the reaction pathways for the rechargeable FeS_2 system into four regions which are defined by their delithiation potential ranges (Figure 4.7): I) Fe redox plateau [1-1.85 V], II) Li insertion/extraction region [1.85 – 2.3 V], III) Li_2S redox plateau [2.3 – 2.42 V], and IV) Fe_3S_4 conversion [2.42 – 3 V] (for T≥ 60 ºC).

Chapter 4.3.2.1. Region I: Fe redox plateau [1-1.85 V]

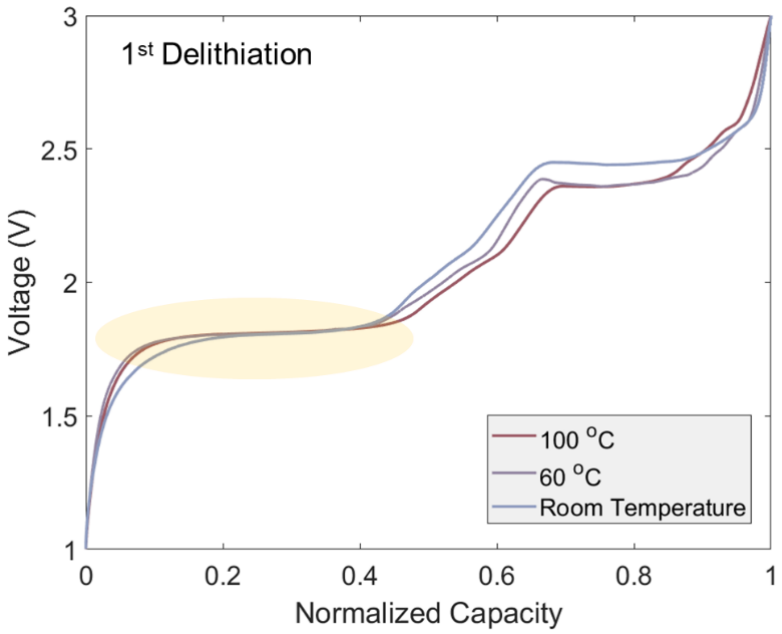

Figure 4.8. Temperature invariance of delithiation conversion potential at ~1.8 V from RT-100 ºC. A C/20 charging rate was used for each temperature.

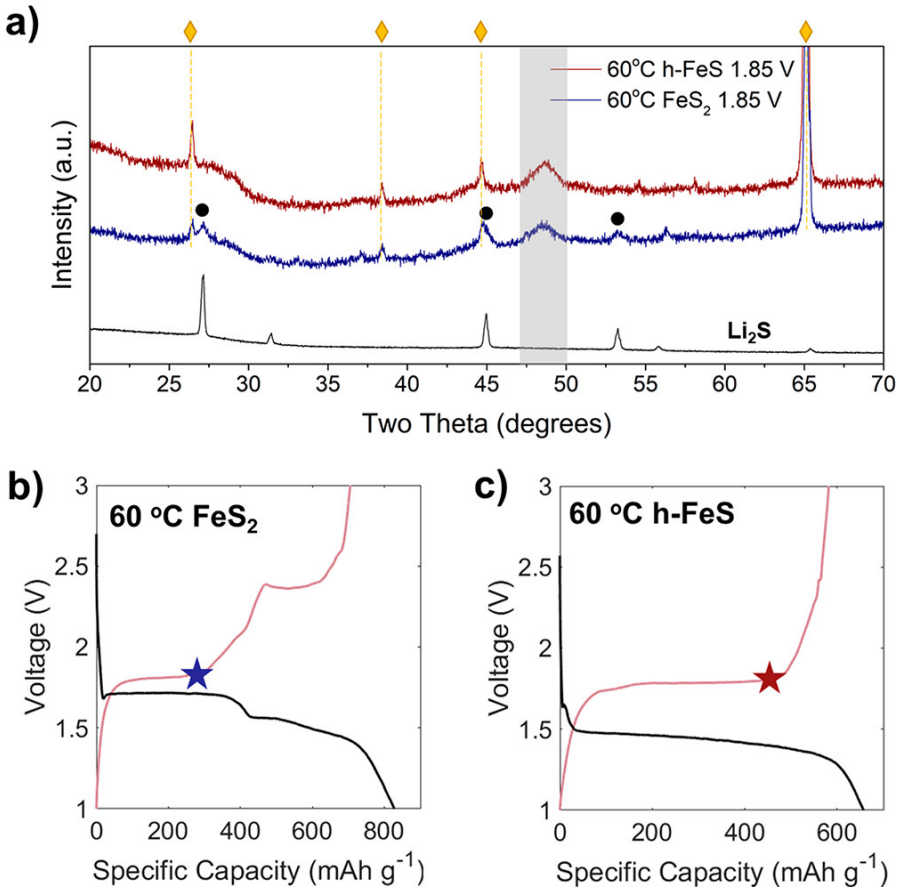

Figure 4.9. Region I: Iron Redox Plateau at 60 ºC. a) XRD comparison of FeS_2 (blue) and h-FeS (red) electrodes delithiated up to 1.85 V. Yellow diamonds represent aluminum current collector peaks. Black circles represent Li_2S diffraction peaks. b) First lithiation (black) and delithiation (pink) of FeS_2 at 60 ºC cycled at C/20. c) First lithiation (black) and delithiation (pink) of h-FeS at 60 ºC cycled at C/20.

Region I is generally cited as the conversion of the discharge products, Li_2S and Fe, into Li_2FeS_2 despite lack of strong evidence for its formation.[10] In revisiting Region I, we observe that the Fe redox plateau features a temperature invariant (room temperature to 100ºC) charging potential (Figure 4.8), a feature commonly associated with conversion reactions.[3,38] In addition, the intermediate species formed in Region I is characterized by the appearance of a broad peak

around ~49º (Figure 4.9a). Interestingly, the observation of a broad peak at ~49º was reported previously by Goodenough while studying lithium insertion into transition metal sulfides, including h-FeS.[22] Here, in comparing the reaction pathways for h-FeS and FeS_2 we note that both iron sulfides share a similarity in the delithiation potential (Figure 4.9 b-c) and product (Figure 4.9a) formed at 1.85 V despite the fact that the overall 1-3 V electrochemical signature of FeS_2 (4 electron redox) differs from h-FeS (2 electron redox). That is, while the reaction pathways are not identical, the reaction pathways in h-FeS are partly observed in FeS_2. For h-FeS, increased crystallinity is observed upon cycling, resulting in the observation of a second peak at ~30º, corresponding closely to tetragonal FeS Mackinawite (t-FeS) (Figure 4.10). Thus, the intermediate formed after the Fe redox plateau in both h-FeS and FeS_2 (Region I) best resembles a lithiated structure similar to nanocrystalline t-FeS (Li_xFeS) as further discussed in the next section. In terms of the differences between the two sulfides, the main observable distinction between FeS_2 and h-FeS is the presence of Li_2S after the Fe redox plateau (Region I) in FeS_2. The detection of Li_2S diffraction peaks (27º, 31º, and 53º) up until 2.3 V (end of Region II) (Figure 4.7) establishes that Li_2S is only partially consumed when it reacts with Fe^0 in Region I. The disappearance of these peaks above 2.3 V indicates complete consumption of Li_2S in Region III. In summary, the presence of Li_2S beyond Region I contrasts with the commonly cited mechanism, where Li_2S consumption is limited to Region I, and leads to the formation of Li_2FeS_2, neither of which are reported in this work. Thus, the following may be written for Region I for our 60°C system.

$$2\ Li_2S + Fe^0 \rightarrow Li_xFeS + y\ Li_2S\ (\text{unreacted}) + z\ Li^+ + z\ e^- \qquad \text{(Eqn. 4.3)}$$

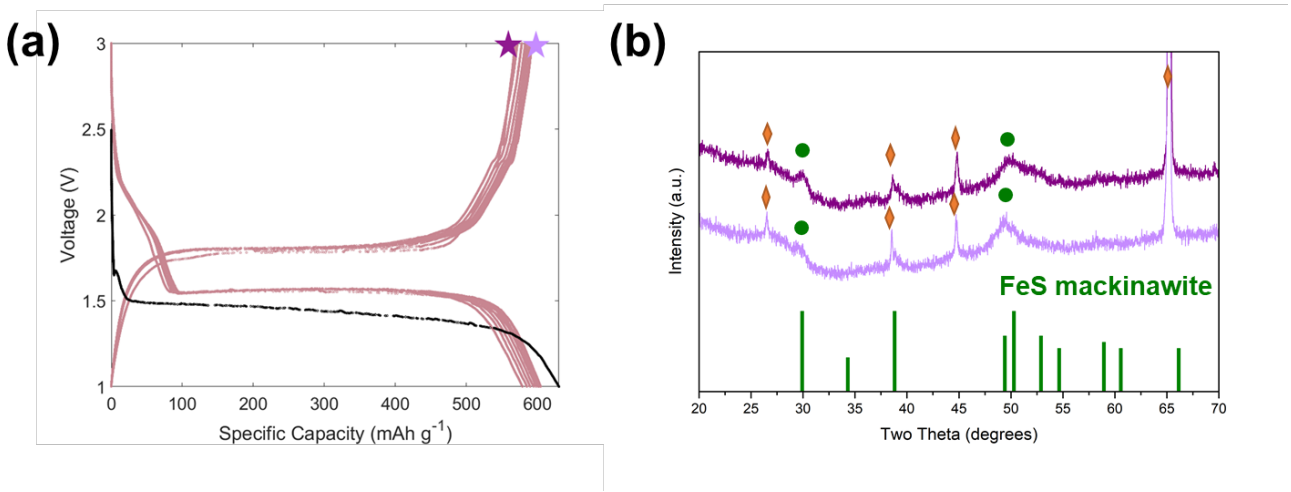

Figure 4.10. a) 60 ºC cycling of FeS at C/20 for 10 cycles in 1M LiFSI $PYR_{14}TFSI$. b) XRD h-FeS charged to 3V for one (light purple) and ten cycles (dark purple). For hexagonal FeS, the charge product on the 1st and 10th cycle is found to best resemble a nanocrystalline tetragonal FeS mackinawite (green circle).

Chapter 4.3.2.2. Region II: Li (De)insertion Region [1.85 – 2.3 V]

The sloped potential regime between 1.8-2.3 V (Region II in Figure 4.7a) is commonly referred to as the (de)intercalation region of Li_2FeS_2. [10,15] However, in our work, we find no evidence for this intermediate phase in the primary reaction or the rechargeable reaction at 60°C. Further, while this region has received much less attention, the capacity contribution is non-negligible and the kinetics of this specific region have yet to be established. The difficulty in studying Region II stems from the large voltage hysteresis which makes it challenging to isolate without capturing the conversion reactions above (Region III) and below it (Region I). To separate this region from the other two conversion reactions, a pre-cycling treatment protocol was employed (Figure 4.12). GITT demonstrates that Region II contributes approximately 140 mAh/g, corresponding to roughly 0.63 e^- transferred.

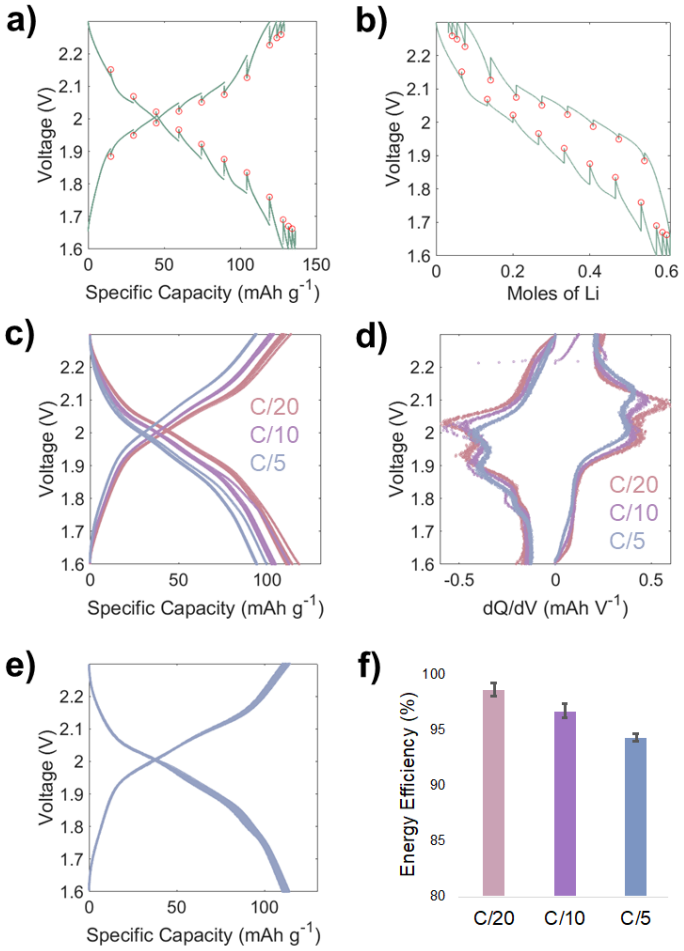

Figure 4.11. Region II: 60 ºC (De)insertion Region Kinetics. a) GITT of the isolated region II [1.6-2.3 V]. Red circles indicate open circuit potential during the rest steps. b) Voltage hysteresis plot of (de)insertion region obtained from the GITT data in part a. c) C-rate testing at C/20 (pink), C/10 (purple), and C/5 (blue) where C is based off of the four-electron redox capacity of FeS_2 (894 mAh g^{-1}). Effective C-rates normalized to capacity of the region II are 0.32 C, 0.64 C, and 1.28 C, respectively. d) dQ/dV plots obtained from c-rate galvanostatic curves in part c. The (de)insertion region features a two peak signature which can be observed at all c rates. e) 1.6-2.3 V cycling data at C/5 (effective c-rate: 1.28 C) for 50 cycles demonstrate excellent cycle stability when

cycled within this potential window. f) Energy efficiency of region II as a function of C-rate. Error bars represent the standard deviation taken from 10 cycles for each c-rate.

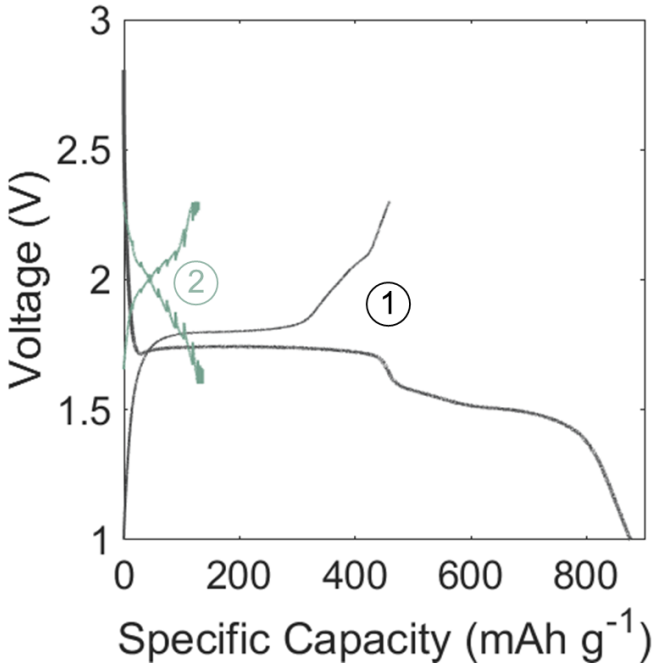

Figure 4.12. Isolation of the Li (de)insertion region (Region II). Step 1: fully lithiate down to 1 V followed by a partial delithiation up to 2.3 V. Step 2: lithiation/delithiation in between 1.6-2.3 V.

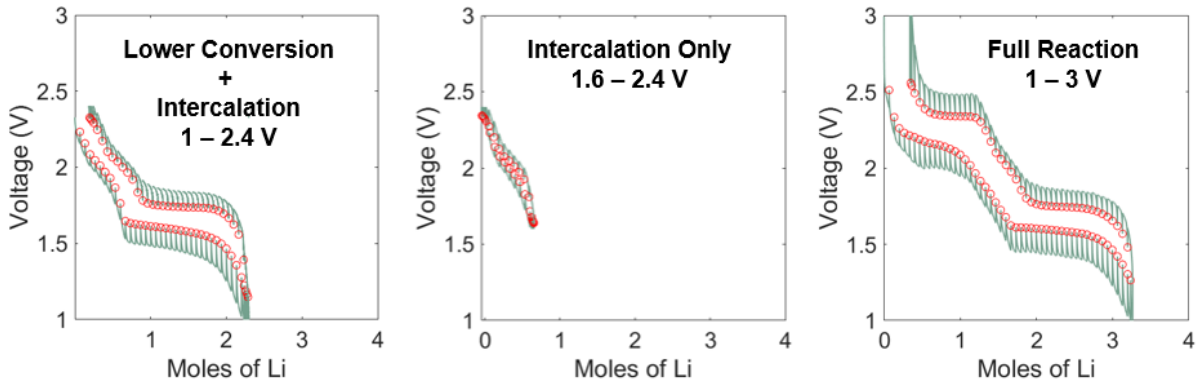

Figure 4.13. GITT of various voltage ranges for FeS_2. Left: 1 – 2.4 V range includes the Region I and Region II. Middle: 1.6 – 2.4 V range captures only Region II. Isolation of this region is shown

in Figure 4.12. Right: 1 – 3 V range captures all the reactions. For all three graphs, red circles represent the open circuit potential during the rest periods. GITT tests were performed at room temperature.

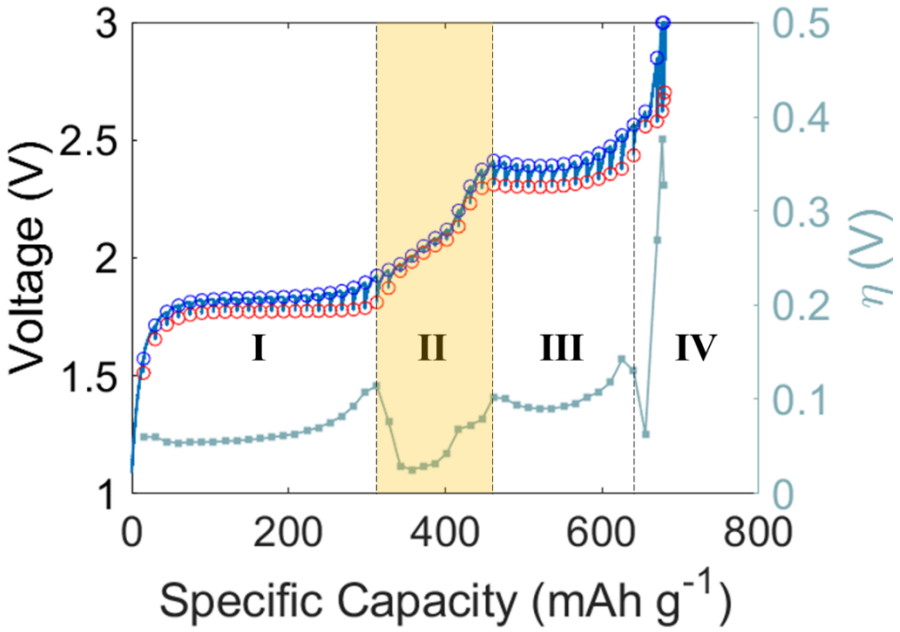

Figure 4.14. GITT of the delithiation of FeS_2 at C/20 pulse for 20 minutes followed by a four-hour rest period. The open circuit potential (OCP) is shown by the red circles and the corresponding overpotential (light teal) is extrapolated by taking the difference between the rest potential and C/20 applied current potential (blue circles). The yellow shaded region highlights Region II, the least kinetically limited region.

Further, the voltage hysteresis in this region is found to be relatively small in comparison to the full 3 V window indicating that Region II's relative contribution to the cell voltage hysteresis is minimal (Figure 4.13). The kinetics and rate capability of Region II are shown in Figure 4.11a-d. While the C-rates used in this study correspond to the full 4 electron redox capacity for FeS_2 (894 mAh g^{-1}), the effective C-rate using the capacity specific to this region (140 mAh/g) translates

to roughly 0.32 C (t~3.1 hr), 0.64 C (t~1.57 hr), and 1.28 C (t~0.78 hr) for C/20, C/10, and C/5, respectively. The good rate capability is further supported by the lower overpotentials observed in GITT, which identify Region II as the least kinetically limited region (Figure 4.14). In terms of cycle stability, at C/5 (effective C-rate: 1.28C) Region II demonstrates excellent stability with an average coulombic efficiency of 99.4% ± 0.2% across 50 cycles (Figure 4.11e). Lastly, while the full 3 V FeS_2 system suffers from a low energy efficiency (~88.7 % at C/20), Region II alone exhibits a much higher energy efficiency of 98.6% ± 0.6%, 96.7% ± 0.6%, and 94.3% ± 0.4%, for C/20, C/10, and C/5, respectively (Figure 4.11f).[40]

The dQ/dV signature of Region II (Figure 4.11d) provides insight regarding the intermediate species formed over this potential range. The two peaks observed in this region correspond to a stepwise change in overpotential obtained from GITT measurements, suggesting that even within Region II, slightly different kinetics associated with each peak may exist (Figure 4.14). While detailed structural characterization of the intermediate species is outside the scope of this work, we note two possibilities based on recent results reported in the literature. E*x-situ* XRD indicates that no new peaks occur in Region II, denoting that no new crystalline phases form within this potential region (Figure 4.7b). One possibility is that the intermediate phase formed in Region I (Figure 4.9) supports lithium insertion, allowing for lithium incorporation without phase change.[32] From our previous comparison of h-FeS and FeS_2 (Figure 4.9), cycling h-FeS resulted in the appearance of a second peak at ~30º which corresponds well to the diffraction peak of t-FeS (mackinawite), a recently reported charge product of FeS_2 (Figure 4.10).[12] Moreover, t-FeS possesses a layered structure with a Van der Waals gap containing two possible interstitial sites and has been reported to intercalate water molecules[41], various alkylammonium ions[42], and alkali hydroxides.[43] Another possibility is that the intermediate species could represent a poorly ordered lamellar iron sulfide which bears similarity to the mackinawite structure and has recently been

reported to reversibly intercalate solvated lithium ions.[44] We note that both of these structures feature a tetrahedrally coordinated iron which is consistent with previous synchrotron studies that characterized the Fe K-edge of the intermediate phase.[32] While more studies are needed to identify the exact structure of the intermediate species, we propose that the intermediate region involves Li insertion/extraction[32] into/out of a mackinawite-based structure (Li_xFeS) at 60°C (Equation 4.4).

$$Li_xFeS \leftrightarrow x\ Li^+ + x\ e^- + t\text{-}FeS \qquad \text{(Eqn. 4.4)}$$

Chapter 4.3.2.3. Region III: Li_2S Redox [2.3 – 2.42 V]

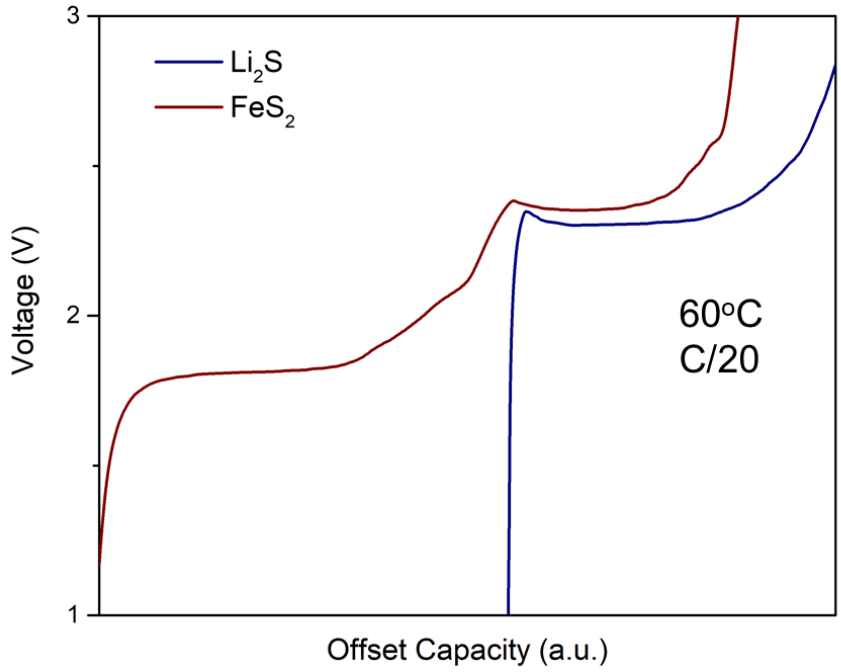

Figure 4.15. Comparison of the delithiation profile of Li_2S in FeS_2 system (red) vs Li_2S-C composite electrodes.

Region III (2.3 – 2.42 V) is commonly cited as the disproportionation of $Li_{2-x}FeS_2$ into an iron sulfide (FeS_x or o-FeS_2) and S.[10,13] While sulfur is also identified above 2.3 V in this work, we attribute its formation to a separate redox mechanism. From *ex-situ* XRD, this region is associated with the disappearance of Li_2S peaks above 2.3 V (Figure 4.7a,b). Li_2S is a well-studied cathode material whose delithiation potential is reported to vary depending on the particle size due to the high activation overpotential originating from its low ionic and electronic conductivity.[37] Studies have shown reduced activation potentials in nano-sized Li_2S around ~2.4 V,[45] similar to the redox potential observed in Region III. In comparing the delithiation potential of nanocrystalline Li_2S with that of FeS_2 at 60ºC (in 1M LiFSI $PYR_{14}TFSI$), both systems exhibit similar potentials in addition to the kink feature unique to Li_2S delithiation (Figure 4.15). In addition, sulfur signals from UV-Vis (Figure 4.16) above 2.3 V further confirm the formation of S_8 from Li_2S redox in Region III.

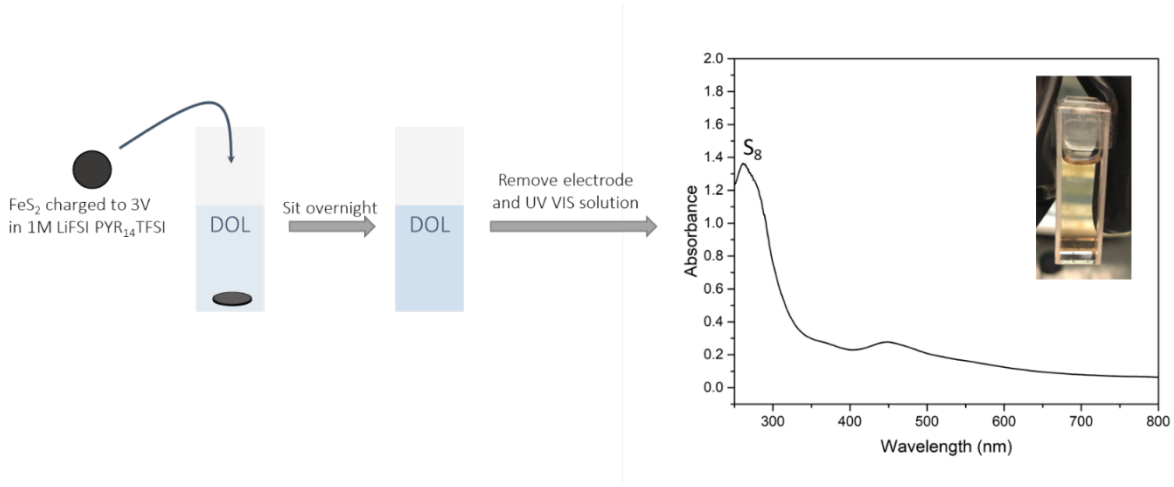

Figure 4.16. Evidence of S_8 as a Charge Product at 3V via DOL extraction UV-Vis.

A FeS_2 coin cell analyzed after one discharge-charge cycle at 60ºC. The coin cell was disassembled and the electrode was left to sit in DOL overnight to extract any soluble and adsorbed polysulfide species. The UV-Vis spectrum of the resulting solution is shown on the right. S_8 signals were detected at ~275 nm.[7]

Therefore, in this work, we establish that sulfur formation in Region III at 60°C originates from Li_2S redox to form sulfur in contrast to the disproportionation of $Li_{2-x}FeS_2$ proposed in earlier studies.[10,11] Although the products formed in Region III, an iron sulfide and elemental sulfur, are consistent with prior work (Table 4.1), the pathways that govern the formation of these species are different. That is, the iron sulfide phase is formed from the delithiation (Region II) of the intermediate phase (Li_xFeS) formed in Region I (Equations 4.3 and 4.4) while the sulfur is formed from Li_2S redox in Region III (Equation 4.5). The identification of Region III as Li_2S redox plays an integral role in properly identifying the origin of capacity loss observed in this specific region upon cycling (*vide infra*).

$$Li_2S \rightarrow 2\,Li^+ + 2e^- + \frac{1}{8}S_8 \quad (\sim 2.4\ V) \qquad \text{(Eqn. 4.5)}$$

Chapter 4.3.2.4. Region IV: Fe_3S_4 Formation [2.42 – 3 V]

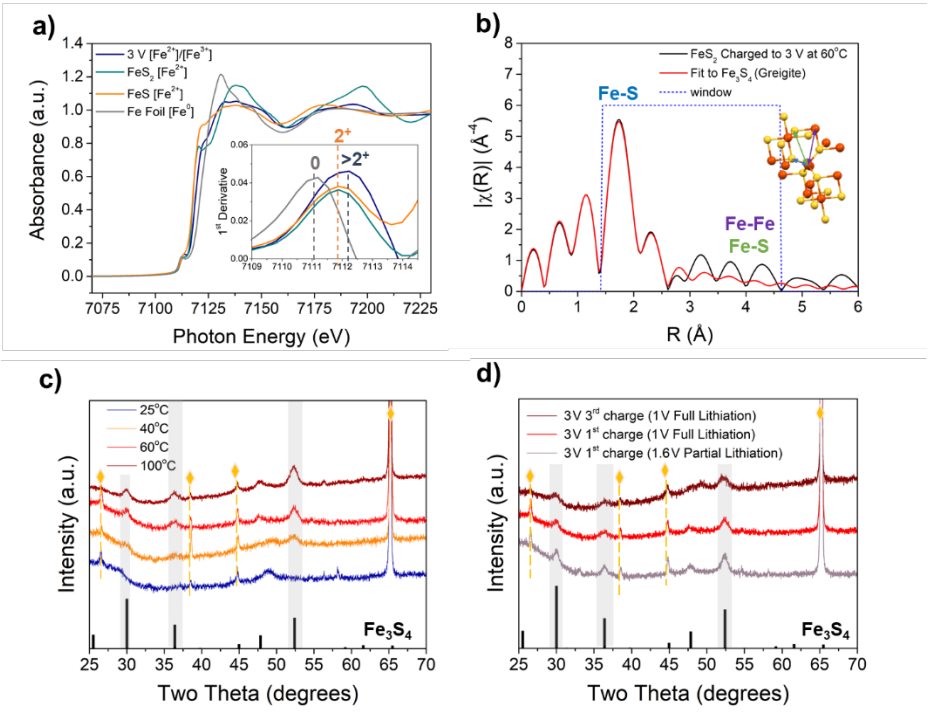

Figure 4.17. Formation of greigite Fe_3S_4 as a charge product. a) XAS spectra of an FeS_2 electrode charged up to 3 V in comparison to other iron sulfide species (Fe foil, h-FeS powder, c-FeS_2

powder). h-FeS and FeS_2 standards represent Fe^{2+}. The inset shows the first derivative plot. The 3 V sample is slightly shifted to the right of FeS and FeS_2 which can be attributed to the mixed Fe $2^+/3^+$ valence of greigite Fe_3S_4 b) k3-weighted Fe K edge Fourier Transform-EXAFS spectra for an FeS_2 electrode charged up to 3 V (black) along with the modeled fit for Fe_3S_4 (red). Fe_3S_4 structure with colored arrows indicate the Fe-S and Fe-Fe bonds fit in the FT-EXAFS spectra. c) XRD graph at 3 V showing temperature dependence of Fe_3S_4 formation from room temperature to 100 ºC. Broad Fe_3S_4 peaks can be seen starting at 40 ºC and become the dominant phase by 60 ºC. Yellow diamonds indicate Al current collector peaks. d) *ex-situ* XRD of FeS_2 electrodes charged to 3 V under varying conditions at 60 ºC: 1) first cycle (red), 2) third cycle (dark red), and 3) partially lithiated to 1.6 V and subsequently charged to 3 V (lavender). Yellow diamonds indicate Al current collector peaks.

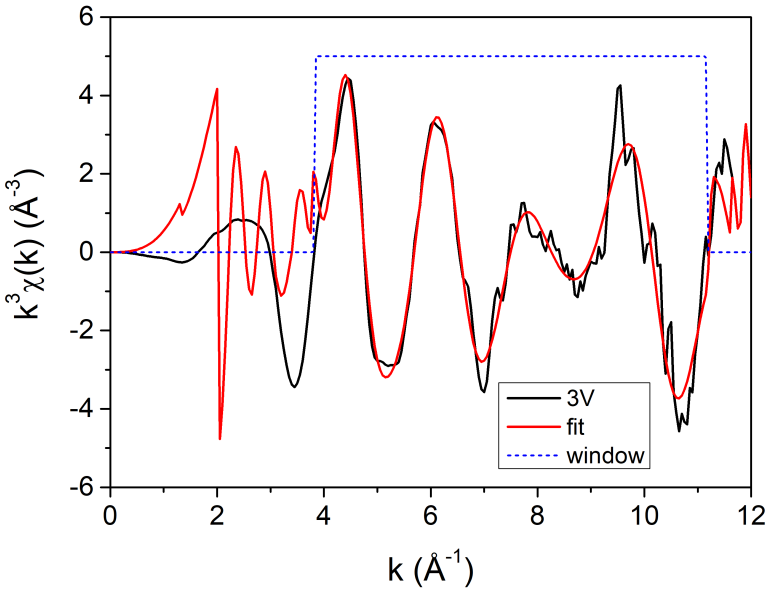

Figure 4.18. Fe K-edge EXAFS spectrum in k-space at 3V (black) alongside fit to Fe_3S_4 standard (red).

Region IV (2.42 -3 V) represents a new reaction which has not been reported previously.[10–12] At 60°C, charging above 2.42 V results in the disappearance of mackinawite-like FeS and the formation of Fe_3S_4 greigite (Figure 4.7b). To the best of our knowledge, this is the first report of an electrochemically-formed Fe_3S_4 from FeS_2. Fe_3S_4 is a less studied iron sulfide battery material,[46,47] but it is a well-studied iron sulfide in the field of geology for its role as an intermediate phase involved in pyrite formation on earth.[8,48] Greigite has been reported to form geologically from mackinawite (t-FeS) in the presence of excess sulfur and known to be an intermediate phase formed prior to pyrite FeS_2 formation under anoxic conditions (Equation 4.6).[8,48–50] More recently, greigite been shown to be a thermodynamically stable Fe-S phase near ambient conditions.[51] To further validate the electrochemically formed Fe_3S_4, the Fe valence state was compared to other iron sulfides (FeS_2 and h-FeS) in XAS. As a result of the mixed Fe $2^+/3^+$ valence in the inverse-spinel Fe_3S_4 structure, the formation of Fe_3S_4 exhibits an average Fe valence $>2^+$. XAS of an electrode cycled up to 3 V at 60 ºC is shown in Figure 4.17a alongside reference spectra for FeS_2 (Fe^{2+}), FeS (Fe^{2+}), and Fe foil (Fe^0). At 3 V, the formation of Fe_3S_4 results in a peak shift to higher energies (7112.1 eV) which helps to confirm that the average valence in the electrode is greater than 2 (7111.9 eV) at the 3 V charge state (Figure 4.17a). Moreover, this peak energy lies at a lower energy than that identified for Fe^{3+}.[52] Further, the EXAFS spectrum of the charge product at 3 V provides a good fit (R-factor= 0.01268) for the Fe_3S_4 structure up to the third shell (Figure 4.17b, Figure 4.18).

$$3\ \text{t-FeS} + S \rightarrow Fe_3S_4\ (>2.42\ V) \qquad \text{(Eqn. 4.6)}$$

To better understand the conditions for the formation of Fe_3S_4, varying temperature and cycling conditions were investigated. At 60 ºC, Fe_3S_4 is the dominant phase detected in XRD and is found to be reversibly formed over a limited number of cycles (Figure 4.17c). Moreover, the

formation of Fe_3S_4 is observed even if FeS_2 is only partially lithiated during the first lithiation and fully charged to 3V, indicating that formation of Li_2S and Fe^0 is not a prerequisite for Fe_3S_4 formation (Figure 4.17d). We find that the sulfur produced from the Li_2S redox above 2.3 V (Region III, Equation 4.5) is crucial to forming the charge product as it provides the sulfur necessary to drive FeS (1 Fe: 1 S) to Fe_3S_4 (1 Fe: 1.33 S), as observed in geological literature under anoxic conditions.[8,48,49] Without the presence of the sulfur generated from Li_2S in Region III, Fe_3S_4 does not form. Therefore, we can conclude that Fe_3S_4 formation is driven by both temperature (~60ºC) and sulfur availability. The latter is further explored in the next section.

Chapter 4.3.3. Evolution of charge product formation in FeS_2

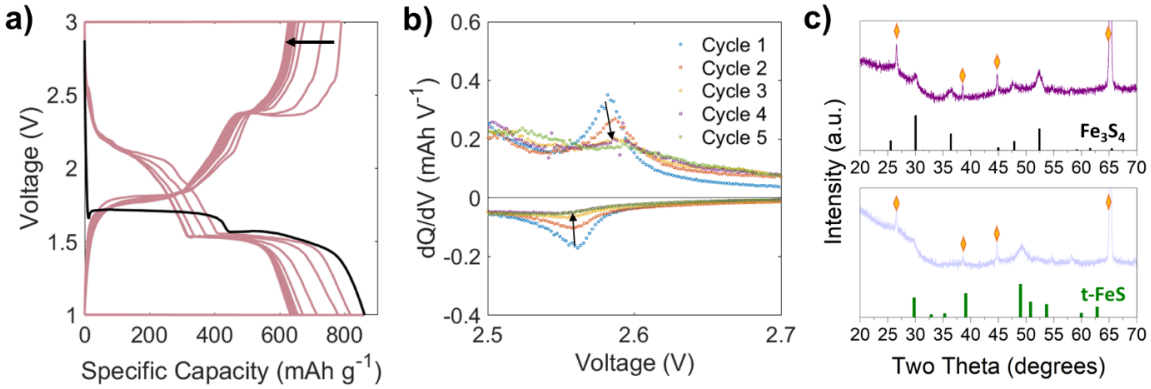

Figure 4.19. Loss of Fe_3S_4 upon cycling of FeS_2 at 60ºC. a) FeS_2 cycling at C/20 for 10 cycles. Initial lithiation is outlined in black. b) dQ/dV obtained from the first 5 cycles of the data shown in part a. Focusing on 2.5-2.7V, the loss of Fe_3S_4 within the first 5 cycles is shown by the steady decreasing peak around ~2.6V. c) top: XRD of an FeS_2 electrode after first charge at 3V. Peak positions for Fe_3S_4 diffraction peaks are provided in black (PDF 96-900-0124). bottom: XRD of an FeS_2 electrode after 10 cycles at 3V. Peak positions for t-FeS mackinawite are provided in green (PDF 00-015-0037). Yellow diamonds represent diffraction peaks for the Al current collector.

The ability to identify degradation mechanisms upon cycling is critical in order to effectively address the limitations in the battery performance of FeS_2. At 60ºC, the greatest capacity loss in the Li-FeS_2 system occurs within the first 5 cycles which is associated with the upper conversion reactions (Region III & IV) (Figure 4.19a). Further, this loss in capacity is linked directly to the decrease in a dQ/dV peak around ~2.6 V which is attributed to Fe_3S_4 conversion (Figure 4.19b). This mechanism is consistent with XRD data (Figure 4.7b) showing Fe_3S_4 formation to occur above 2.42 V in addition to the absence of this dQ/dV peak at room temperature (Figure 4.20).

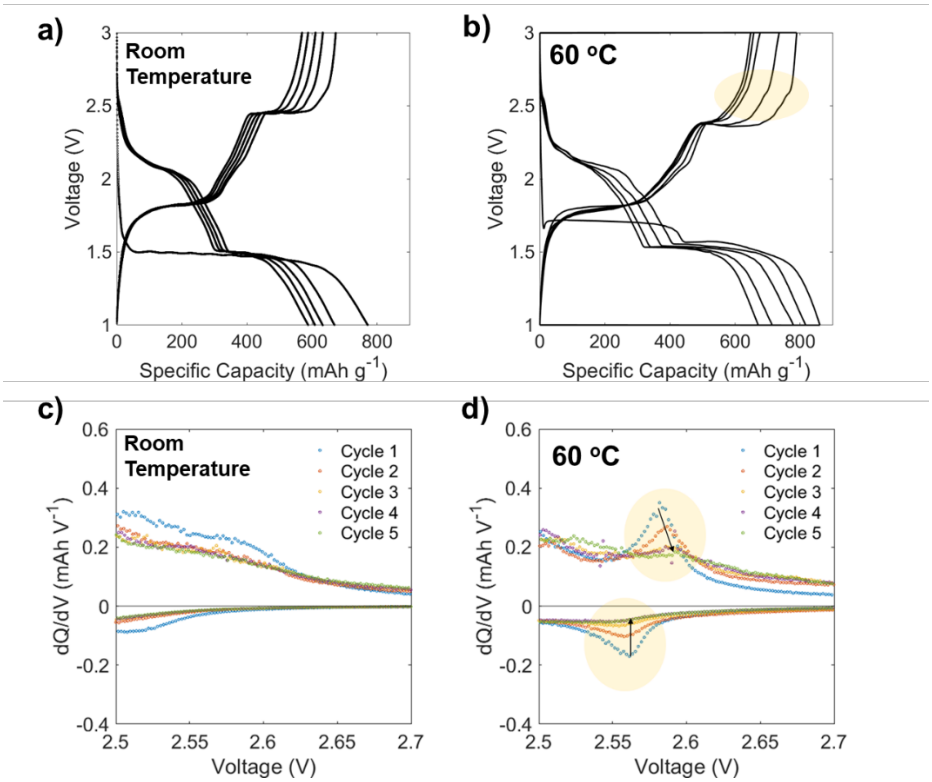

Figure 4.20. dQ/dV comparison for room temperature and 60 ºC. Fe_3S_4 conversion reactions highlighted in yellow region at 60 ºC are absent at room temperature, where Fe_3S_4 does not form.

The absence of this peak is not surprising since Fe_3S_4 is not formed as a charge product at room temperature. The gradual decrease and eventual loss of the dQ/dV peak for Fe_3S_4 coincides with a loss of capacity from Region III (Equation 4.5) indicating that less sulfur is being formed each cycle. This loss of sulfur is facilitated by polysulfide shuttling into the electrolyte upon cycling as detected in UV-Vis (Figure 4.21).

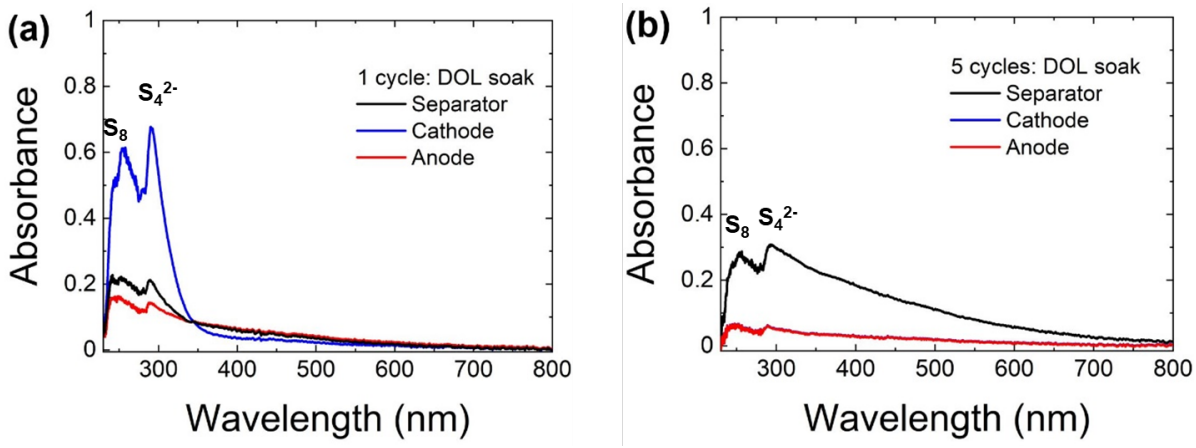

Figure 4.21. *Ex-situ* UV-vis spectra of the separated coin cell components (anode, cathode, and separator) soaked in DOL solvent after the (a) first and (b) fifth cycles. After the first charge (3 V) cycle, the polysulfides are primarily localized near the cathode. However, upon further cycling, the largest polysulfide signals originate from the separator indicative of polysulfide shuttling. Each component was soaked in 4.0 mL of DOL (in separate vials) for 24 h before UV-vis analysis. A blank spectrum of pure DOL was used for background subtraction in all cases. S_8 and S_4^{2-} signals were observed at ~275 and ~300 nm, respectively.[7] For graph b, the cathode signal overlaps with the anode (red).

Comparing the XRD of the first and tenth charge cycle, the disappearance of Fe_3S_4 and the detection of its precursors, t-FeS (Figure 4.19c; formed in Region II) and sulfur (formed in

Region III), upon charge are observed. We note that the precursors for Fe_3S_4 are also the charge products formed at room temperature, a temperature at which Fe_3S_4 does not form (Figure 4.22).

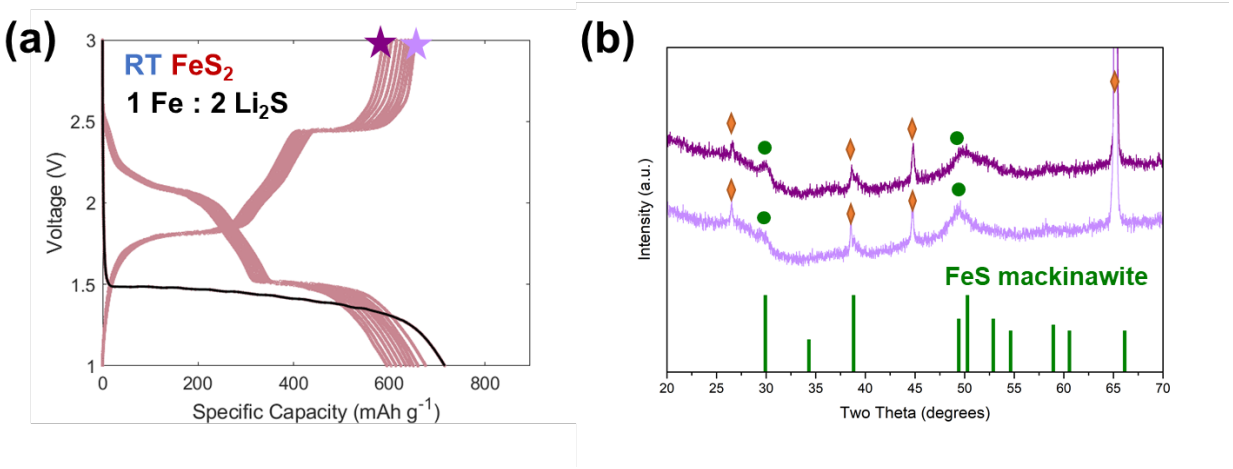

Figure 4.22. XRD comparison of the 1st charge (light purple) and 10th charge (dark purple) cycle at room temperature. t-FeS mackinawite diffraction peaks are shown in green. Orange diamonds indicate Al current collector peaks.

Compositionally, the change in the charge product reflects a loss of sulfur from Fe_3S_4 (1 Fe: 1.33 S) to FeS (1 Fe: 1 S). This is reflected in the electrochemistry by the shrinking redox plateau in Region III within the first few cycles indicating a loss of sulfur produced from Li_2S redox. That is, the inability to form Fe_3S_4 after the first few cycles is attributed to the loss of sulfur which inhibits the formation of a more sulfur rich Fe_3S_4 from a less sulfur rich mackinawite t-FeS precursor. Additionally, it should be noted that this initial capacity loss was observed even when imposing a cutoff voltage to prevent the formation of Fe_3S_4 (Figure 4.23), suggesting that the loss of sulfur plays a more significant role in the initial capacity loss than the Fe_3S_4 reaction itself.

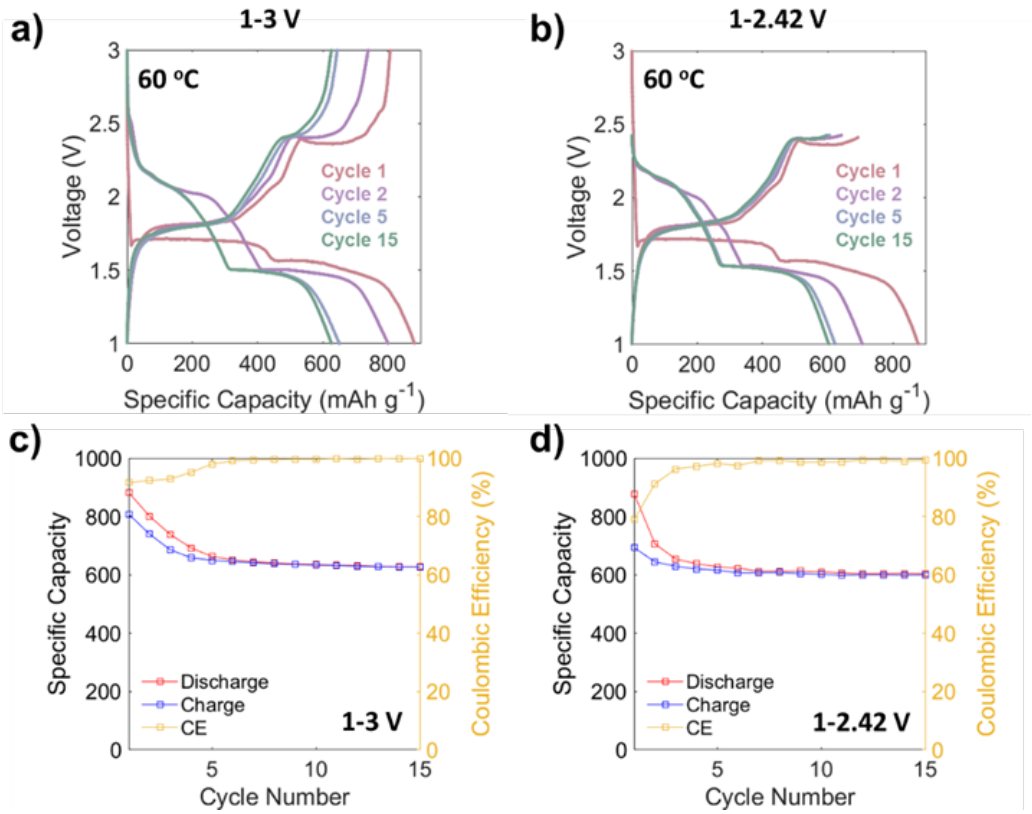

Figure 4.23. a) FeS_2 cycle stability test at 60 ºC for a) 1-3 V window and b) 1-2.42 V window. For both a) and b), the first cycle (pink) was conducted at C/20 while the subsequent cycles were cycled at C/5 (purple, blue, green). Specific capacity as a function of cycle number for c) 1-3 V and d) 1-2.42 V. For both c) and d), the coulombic efficiency is shown in yellow.

The results presented here underscore the importance of sulfur availability and retention in achieving the reproducible formation of charge products and stable cycling performance. The low polysulfide solubility of the ionic liquid used in this study enables the formation of Fe_3S_4 in the first charge. However, upon cycling, the continuous loss of sulfur through polysulfide solubility inhibits its long-term formation and its precursors are detected upon charge instead. Comparing Fe_3S_4 to other charge products reported at 60ºC (Table 4.1.), the electrolyte, and more specifically, the relative polysulfide/sulfur solubility, is critical. For solid state electrolyte systems,

the ability to inhibit polysulfide shuttling allows for high sulfur retention and the formation of sulfur rich phases such as o-FeS_2 (1 Fe: 2 S).[11] In contrast, organic solvents, such as DOL:DME, suffer higher losses of sulfur due to polysulfide shuttling, resulting in the formation of lower sulfur content phases such as t-FeS (1 Fe: 1 S).[12] The ionic liquid used in this study represents a middle ground in terms of polysulfide/sulfur solubility resulting in the formation of Fe_3S_4 (1 Fe: 1.33 S).

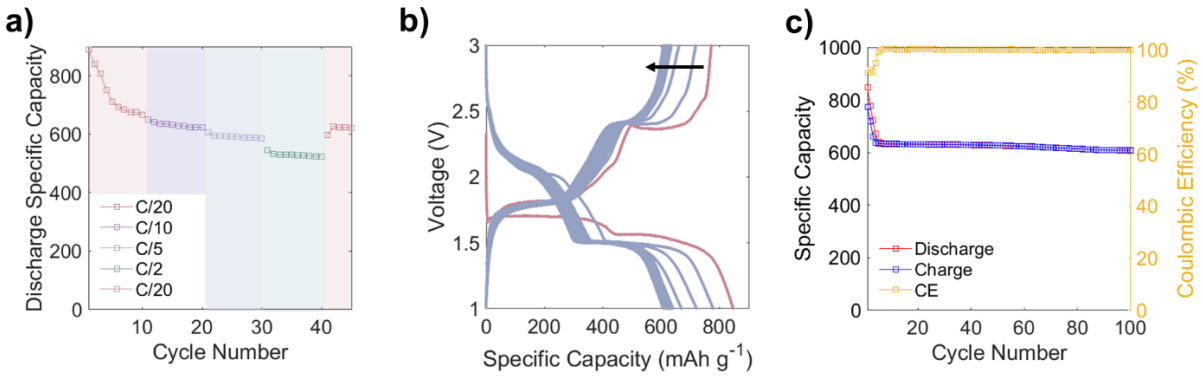

Figure 4.24. Electrochemical Performance of FeS_2 in 1M LiFSI $PYR_{14}TFSI$ at 60 ºC. a) C-rate testing for FeS_2. b) FeS_2 cycle stability test. The first cycle (pink) was conducted at C/20 and then subsequently cycled at C/5 for a total of 100 cycles. c) Specific capacity as a function of cycle number from data shown in b). Coulombic efficiency is shown in yellow.

The new understanding gained regarding lithiation and delithiation of FeS_2 provides a basis for demonstrating stable electrochemical performance observed in the iron sulfide-based battery. Using the ionic liquid electrolyte, testing at 60ºC indicates that the reversible system based on the charge products, t-FeS and S_8, can be cycled at rates as fast as C/2 without significant loss of capacity (Figure 4.24a). As mentioned previously, the largest capacity losses occur within the first few cycles which coincide with the loss of Fe_3S_4 and formation of t-FeS as the charge product. However, beyond the 5th cycle, stable capacity is achieved and cycling at

C/5 for 100 cycles demonstrates a capacity of 600 mAh g^{-1} with an average coulombic efficiency of 99.4% ± 0.2% for cycles 6-100 (Figure 4.24 b-c).

Chapter 4.4. Conclusion

The present study has used a variety of characterization methods to determine the products and reaction pathways involved in the rechargeable Li-FeS_2 system. The research involved the use of an ionic liquid electrolyte (1M LiFSI in $PYR_{14}TFSI$) to reduce the influence of the polysulfide shuttle as well as enable operation at slightly elevated temperatures (~60°C) to better resolve phase formation. In studying the rechargeable reaction pathway of FeS_2, we provide several new insights associated with the reactions occurring upon lithiation and delithiation in different potential ranges. After the first lithiation, FeS_2 is no longer formed as a charge product and the reversible electrochemical properties result from the formation of other iron sulfide phases. In particular, greigite Fe_3S_4 is detected as a charge product, for the first time, establishing temperature and sulfur availability as key components for its formation. Within the first few cycles, greigite Fe_3S_4 is no longer formed and an iron sulfide phase best resembling tetragonal mackinawite (t-FeS) is produced. The change in charge product to a lower sulfur content iron sulfide phase coincides with the loss of sulfur based on the new reaction pathways established in this work. t-FeS and sulfur are identified as the long-term charge products which demonstrate a stable capacity of ~600 mAh/g (at C/5, 60 ºC). The connection between sulfur loss, capacity fade, and charge product composition highlights the critical need to retain sulfur in the active material upon cycling. The importance of sulfur retention, taken together with the ability to replicate FeS_2 electrochemistry from the ball milling of lithium containing intermediates presented in this research, provides a basis for linking the current work with emerging solid-state anode-free systems.

Chapter 4.5. References

(1) IEA. *Net Zero by 2050: A Roadmap for the Global Energy Sector*; 2021.

(2) Castelvecchi, D. Electric Cars and Batteries: How Will the World Produce Enough? *Nature* **2021**, *596* (7872), 336–339. https://doi.org/10.1038/d41586-021-02222-1.

(3) Cabana, J.; Monconduit, L.; Larcher, D.; Palacín, M. R. Beyond Intercalation-Based Li-Ion Batteries: The State of the Art and Challenges of Electrode Materials Reacting through Conversion Reactions. *Adv. Mater.* **2010**, *22* (35), 170–192. https://doi.org/10.1002/adma.201000717.

(4) Whittingham, M. S. Ultimate Limits to Intercalation Reactions for Lithium Batteries. *Chem. Rev.* **2014**, *114* (23), 11414–11443. https://doi.org/10.1021/cr5003003.

(5) Schmuch, R.; Wagner, R.; Hörpel, G.; Placke, T.; Winter, M. Performance and Cost of Materials for Lithium-Based Rechargeable Automotive Batteries. *Nat. Energy* **2018**, *3* (4), 267–278. https://doi.org/10.1038/s41560-018-0107-2.

(6) Cutting Cobalt. *Nat. Energy* **2020**, *5* (11), 825. https://doi.org/10.1038/s41560-020-00731-3.

(7) Nassar, N. T.; Fortier, S. M. Methodology and Technical Input for the 2021 Review and Revision of the U . S . Critical Minerals List. *U.S. Geol. Surv. Open File Rep.* **2021**, *2021–1045*, 31.

(8) Rickard, D.; Luther, G. W. Chemistry of Iron Sulfides. *Chem. Rev.* **2007**, *107* (2), 514–562. https://doi.org/10.1021/cr0503658.

(9) Schoonen, M. A. A. Mechanisms of Sedimentary Pyrite Formation. *Spec. Pap. Geol. Soc. Am.* **2004**, *379*, 117–134. https://doi.org/10.1130/0-8137-2379-5.117.

(10) Fong, R. Electrochemistry of Pyrite-Based Cathodes for Ambient Temperature Lithium Batteries. *J. Electrochem. Soc.* **1989**, *136* (11), 3206. https://doi.org/10.1149/1.2096426.

(11) Yersak, T. A.; Macpherson, H. A.; Kim, S. C.; Le, V. D.; Kang, C. S.; Son, S. B.; Kim, Y. H.; Trevey, J. E.; Oh, K. H.; Stol dt, C.; Lee, S. H. Solid State Enabled Reversible Four Electron Storage. *Adv. Energy Mater.* **2013**, *3* (1), 120–127. https://doi.org/10.1002/aenm.201200267.

(12) Zou, J.; Zhao, J.; Wang, B.; Chen, S.; Chen, P.; Ran, Q.; Li, L.; Wang, X.; Yao, J.; Li, H.; Huang, J.; Niu, X.; Wang, L. Unraveling the Reaction Mechanism of FeS 2 as a Li-Ion Battery Cathode. *ACS Appl. Mater. Interfaces* **2020**, *12* (40), 44850–44857. https://doi.org/10.1021/acsami.0c14082.

(13) Zhang, S. S. The Redox Mechanism of FeS2 in Non-Aqueous Electrolytes for Lithium and Sodium Batteries. *J. Mater. Chem. A* **2015**, *3* (15), 7689–7694. https://doi.org/10.1039/c5ta00623f.

(14) a.R. Lennie; Vaughan, D. J. Spectroscopic Studies of Iron Sulfide Formation and Phase Relations at Low Temperatures. *Miner. Spectrosc. a Tribut. to Roger G. Burn.* **1996**, No. 5, 117–131.

(15) Evans, T.; Piper, D. M.; Kim, S. C.; Han, S. S.; Bhat, V.; Oh, K. H.; Lee, S. H. Ionic Liquid Enabled FeS2 for High-Energy-Density Lithium-Ion Batteries. *Adv. Mater.* **2014**, *26* (43), 7386–7392. https://doi.org/10.1002/adma.201402103.

(16) Liu, H.; Jing, R.; Wang, Z.; You, C.; Science, M. FeS 2 Encapsulated with Mesoporous Carbon for High - Performance Lithium - Ion Batteries Material Characterization Synthesis of MPC Electrochemical Measurements. *MRS Commun.* **2021**, *XX* (xx), 1–7. https://doi.org/10.1557/s43579-021-00048-6.

(17) Mwizerwa, J. P.; Zhang, Q.; Han, F.; Wan, H.; Cai, L.; Wang, C.; Yao, X. Sulfur-Embedded FeS2 as a High-Performance Cathode for Room Temperature All-Solid-State Lithium-Sulfur Batteries. *ACS Appl. Mater. Interfaces* **2020**, *12* (16), 18519–18525. https://doi.org/10.1021/acsami.0c01607.

(18) Dewald, G. F.; Liaqat, Z.; Lange, M. A.; Tremel, W.; Zeier, W. G. Influence of Iron Sulfide Nanoparticle Sizes in Solid-State Batteries**. *Angew. Chemie* **2021**, *133* (33), 18096–18100. https://doi.org/10.1002/ange.202106018.

(19) Li, L.; Cabán-Acevedo, M.; Girard, S. N.; Jin, S. High-Purity Iron Pyrite (FeS2) Nanowires as High-Capacity Nanostructured Cathodes for Lithium-Ion Batteries. *Nanoscale* **2014**, *6* (4), 2112–2118. https://doi.org/10.1039/c3nr05851d.

(20) Schorr, B. N. B.; Kolesnichenko, I. V.; Merrill, L. C.; Wygant, B. R.; Harrison, K. L.; Lambert, T. N. Stable Cycling of Lithium Batteries Utilizing Iron Disulfide Nanoparticles. *ACS Appl. Nano Mater.* **2021**, *4* (11), 11636–11643. https://doi.org/10.1021/acsanm.1c02178.

(21) Xu, K. Nonaqueous Liquid Electrolytes for Lithium-Based Rechargeable Batteries. *Chem. Rev.* **2004**, *104* (10), 4303–4417. https://doi.org/10.1021/cr030203g.

(22) Kim, Y.; Goodenough, J. B. Lithium Insertion into Transition-Metal Monosulfides: Tuning the Position of the Metal 4s Band. *J. Phys. Chem. C* **2008**, *112* (38), 15060–15064. https://doi.org/10.1021/jp8038847.

(23) Li, C.; Sarapulova, A.; Pfeifer, K.; Luo, X.; Maria Casati, N. Pietro; Welter, E.; Melinte, G.; Fu, Q.; Dsoke, S. Elucidating the Mechanism of Li Insertion into Fe1- XS/Carbon via in Operando Synchrotron Studies. *ACS Appl. Mater. Interfaces* **2020**, *12* (47), 52691–52700. https://doi.org/10.1021/acsami.0c15500.

(24) Liao, F.; Świątowska, J.; Maurice, V.; Seyeux, A.; Klein, L. H.; Zanna, S.; Marcus, P. Electrochemical Lithiation and Passivation Mechanisms of Iron Monosulfide Thin Film as Negative Electrode Material for Lithium-Ion Batteries Studied by Surface Analytical Techniques. *Appl. Surf. Sci.* **2013**, *283*, 888–899. https://doi.org/10.1016/j.apsusc.2013.07.039.

(25) Lapp, A. S.; Whang, G.; Bhandarkar, A.; Kolesnichenko, I. V.; Dunn, B. S.; Lambert, T. N.; Talin, A. A. In Situ UV–Vis Analysis of Polysulfide Shuttling in Ionic Liquid-Based Li-FeS 2 Batteries. *J. Phys. Chem. C* **2022**, *126* (11), 5101–5111. https://doi.org/10.1021/acs.jpcc.1c10074.

(26) Pelé, V.; Flamary, F.; Bourgeois, L.; Pecquenard, B.; Le Cras, F. Perfect Reversibility of the Lithium Insertion in FeS2: The Combined Effects of All-Solid-State and Thin Film Cell Configurations. *Electrochem. commun.* **2015**, *51*, 81–84. https://doi.org/10.1016/j.elecom.2014.12.009.

(27) Hu, Z.; Zhang, K.; Zhu, Z.; Tao, Z.; Chen, J. FeS2 Microspheres with an Ether-Based Electrolyte for High-Performance Rechargeable Lithium Batteries. *J. Mater. Chem. A* **2015**, *3* (24), 12898–12904. https://doi.org/10.1039/c5ta02169c.

(28) Lu, J.; Lian, F.; Guan, L.; Zhang, Y.; Ding, F. Adapting FeS 2 Micron Particles as an Electrode Material for Lithium-Ion Batteries: Via Simultaneous Construction of CNT Internal Networks and External Cages. *J. Mater. Chem. A* **2019**, *7* (3), 991–997. https://doi.org/10.1039/c8ta09955c.

(29) Wan, H.; Liu, G.; Li, Y.; Weng, W.; Mwizerwa, J. P.; Tian, Z.; Chen, L.; Yao, X. Transitional Metal Catalytic Pyrite Cathode Enables Ultrastable Four-Electron-Based All-Solid-State Lithium Batteries. *ACS Nano* **2019**, *13* (8), 9551–9560. https://doi.org/10.1021/acsnano.9b04538.

(30) Tryk, D. A.; Kim, S.; Hu, Y.; Xing, W.; Scherson, D. A.; Antonio, M. R.; Leger, V. Z.; Blomgren, G. E. Electrochemical Insertion of Lithium into Pyrite from Nonaqueous Electrolytes at Room Temperature. An in Situ Fe K-Edge X-Ray Absorption Fine Structure Study. *J. Phys. Chem.* **1995**, *99* (11), 3732–3735. https://doi.org/10.1021/j100011a047.

(31) Shao-Horn, Y.; Osmialowski, S.; Horn, Q. C. Reinvestigation of Lithium Reaction Mechanisms in FeS[Sub 2] Pyrite at Ambient Temperature. *J. Electrochem. Soc.* **2002**, *149* (12), A1547. https://doi.org/10.1149/1.1516772.

(32) Butala, M. M.; Mayo, M.; Doan-Nguyen, V. V. T.; Lumley, M. A.; Göbel, C.; Wiaderek, K. M.; Borkiewicz, O. J.; Chapman, K. W.; Chupas, P. J.; Balasubramanian, M.; Laurita, G.; Britto, S.; Morris, A. J.; Grey, C. P.; Seshadri, R. Local Structure Evolution and Modes of Charge Storage in Secondary Li-FeS2 Cells. *Chem. Mater.* **2017**, *29* (7), 3070–3082. https://doi.org/10.1021/acs.chemmater.7b00070.

(33) Jones, C. H. W.; Kovacs, P. E.; Sharma, R. D.; McMillan, R. S. An 57Fe Mössbauer Study of the Intermediates Formed in the Reduction of FeS2 in the Li/FeS2 Battery System. *J. Phys. Chem.* **1991**, *95* (2), 774–779. https://doi.org/10.1021/j100155a053.

(34) Fantauzzi, M.; Elsener, B.; Atzei, D.; Rigoldi, A.; Rossi, A. Exploiting XPS for the Identification of Sulfides and Polysulfides. *RSC Adv.* **2015**, *5* (93), 75953–75963. https://doi.org/10.1039/c5ra14915k.

(35) Nandasiri, M. I.; Camacho-Forero, L. E.; Schwarz, A. M.; Shutthanandan, V.; Thevuthasan, S.; Balbuena, P. B.; Mueller, K. T.; Murugesan, V. In Situ Chemical Imaging of Solid-Electrolyte Interphase Layer Evolution in Li-S Batteries. *Chem. Mater.* **2017**, *29* (11), 4728–4737. https://doi.org/10.1021/acs.chemmater.7b00374.

(36) Klein, M. J.; Goossens, K.; Bielawski, C. W.; Manthiram, A. Elucidating the Electrochemical Activity of Electrolyte-Insoluble Polysulfide Species in Lithium-Sulfur Batteries. *J. Electrochem. Soc.* **2016**, *163* (9), A2109–A2116. https://doi.org/10.1149/2.0051610jes.

(37) Ye, H.; Li, M.; Liu, T.; Li, Y.; Lu, J. Activating Li2S as the Lithium-Containing Cathode in Lithium-Sulfur Batteries. *ACS Energy Lett.* **2020**, *5* (7), 2234–2245. https://doi.org/10.1021/acsenergylett.0c00936.

(38) Ponrouch, A.; Cabana, J.; Dugas, R.; Slack, J. L.; Palacín, M. R. Electroanalytical Study of the Viability of Conversion Reactions as Energy Storage Mechanisms. *RSC Adv.* **2014**, *4* (68), 35988–35996. https://doi.org/10.1039/c4ra05189k.

(39) Tomczuk, Z.; Roche, M. F.; Vissers, D. R. Phase Relationships in Positive Electrodes of High Temperature Lithium Aluminum/Iron Sulfide Cells. *Proc Electrochem Soc* **1981**, 81–4, 381–391.

(40) Eftekhari, A. Energy Efficiency: A Critically Important but Neglected Factor in Battery Research. *Sustain. Energy Fuels* **2017**, *1* (10), 2053–2060. https://doi.org/10.1039/c7se00350a.

(41) Wolthers, M.; Gaast, S. J. Van Der; Rickard, D. The Structure of Disordered Mackinawite. *Am. Mineral.* **2003**, *88* (11–12), 2007–2015. https://doi.org/doi:10.2138/am-2003-11-1245.

(42) Lim, H.; Pham, D. T.; Jung, J. H.; Lee, H. C.; Ihm, J.; Cho, K. Alkylammonium-Intercalated 2D Mackinawite FeS as Electrode Materials for Rechargeable Batteries. *Chem. Mater.* **2020**, *32* (21), 9147–9154. https://doi.org/10.1021/acs.chemmater.0c02308.

(43) Zhou, X.; Eckberg, C.; Wilfong, B.; Liou, S. C.; Vivanco, H. K.; Paglione, J.; Rodriguez, E. E. Superconductivity and Magnetism in Iron Sulfides Intercalated by Metal Hydroxides. *Chem. Sci.* **2017**, *8* (5), 3781–3788. https://doi.org/10.1039/c6sc05268a.

(44) Horwitz, N. E.; Shevchenko, E. V.; Park, J.; Lee, E.; Xie, J.; Chen, B.; Zhong, Y.; Filatov, A. S.; Anderson, J. S. Synthesis, Modular Composition, and Electrochemical Properties of Lamellar Iron Sulfides. *J. Mater. Chem. A* **2020**, *8* (31), 15834–15844. https://doi.org/10.1039/d0ta00689k.

(45) Takeuchi, T.; Kageyama, H.; Taguchi, N.; Nakanishi, K.; Kawaguchi, T.; Ohara, K.; Fukuda, K.; Sakuda, A.; Ohta, T.; Fukunaga, T.; Sakaebe, H.; Kobayashi, H.; Matsubara, E. Structure Analyses of Fe-Substituted Li2S-Based Positive Electrode Materials for Li-S Batteries. *Solid State Ionics* **2018**, *320* (February), 387–391. https://doi.org/10.1016/j.ssi.2018.03.028.

(46) Paolella, A.; George, C.; Povia, M.; Zhang, Y.; Krahne, R.; Gich, M.; Genovese, A.; Falqui, A.; Longobardi, M.; Guardia, P.; Pellegrino, T.; Manna, L. Charge Transport and Electrochemical Properties of Colloidal Greigite (Fe3S4) Nanoplatelets. *Chem. Mater.* **2011**, *23* (16), 3762–3768. https://doi.org/10.1021/cm201531h.

(47) Li, G.; Zhang, B.; Yu, F.; Novakova, A. A.; Krivenkov, M. S.; Kiseleva, T. Y.; Chang, L.; Rao, J.; Polyakov, A. O.; Blake, G. R.; De Groot, R. A.; Palstra, T. T. M. High-Purity Fe3S4 Greigite Microcrystals for Magnetic and Electrochemical Performance. *Chem. Mater.* **2014**, *26* (20), 5821–5829. https://doi.org/10.1021/cm501493m.

(48) Hunger, S.; Benning, L. G. Greigite: A True Intermediate on the Polysulfide Pathway to Pyrite. *Geochem. Trans.* **2007**, *8*, 1–20. https://doi.org/10.1186/1467-4866-8-1.

(49) Roberts, A. P.; Chang, L.; Rowan, C. J.; Horng, C.-S.; Florindo, F. Magnetic Properties of

Sedimentary Greigite (Fe 3 S 4): An Update. *Rev. Geophys.* **2011**, *49* (1), RG1002. https://doi.org/10.1029/2010RG000336.

(50) Benning, L. G.; Wilkin, R. T.; Barnes, H. L. Reaction Pathways in the Fe-S System below 100°C. *Chem. Geol.* **2000**, *167* (1–2), 25–51. https://doi.org/10.1016/S0009-2541(99)00198-9.

(51) Subramani, T.; Lilova, K.; Abramchuk, M.; Leinenweber, K. D.; Navrotsky, A. Greigite (Fe3S4) Is Thermodynamically Stable: Implications for Its Terrestrial and Planetary Occurrence. *Proc. Natl. Acad. Sci. U. S. A.* **2020**, *117* (46), 28645–28648. https://doi.org/10.1073/pnas.2017312117.

(52) Simon, H.; Cibin, G.; Freestone, I.; Schofield, E. Fe K-Edge x-Ray Absorption Spectroscopy of Corrosion Phases of Archaeological Iron: Results, Limitations, and the Need for Complementary Techniques. *J. Phys. Condens. Matter* **2021**, *33* (34), 344002. https://doi.org/10.1088/1361-648X/ac08b6.

Chapter 5. Photopatternable Porous Separators for Micro-Electrochemical Energy Storage Systems

The miniaturization of electrochemical energy storage systems (EES), one of the key challenges facing the rapid expansion of the Internet of Things, has been limited by poor performance of various energy storage components at the micron scale. In this paper, we report the development of a unique photopatternable porous separator which overcomes the electrolyte difficulties involving resistive losses at small dimensions. The separator is based on modifying the chemistry of SU-8, an epoxy derived photoresist, through the addition of a miscible ionic liquid. The ionic liquid serves as a templating agent which is selectively removed by solution methods, leaving the SU-8 scaffold whose interconnected porosity provides ion transport from the confined liquid electrolyte. The photopatternable separator exhibits good electrochemical, chemical, thermal and mechanical stability during the operation of electrochemical devices in both 2D and 3D formats. For the latter, the separator demonstrated the ability to form functional conformal coatings over 3D structures. The development of the photopatternable separator overcomes the electrolyte issues which have limited progress in the field of micro-EES.

Chapter 5.1. Introduction

Continuous improvement in device functionality coupled with reduction of the hardware form factor are the key enabling factors in the Internet of Things (IoT) era.[1] The miniaturization of microelectronics sets new requirements for device components, component packages, and fabrication technologies. One of the challenges associated with the continuous miniaturization is related to the poor performance of energy storage components at a small scale, resulting from their low packaged areal energy density and inadequate cyclability.[2,3] To overcome this limitation, the application of micro-fabrication technology has enabled on-chip electrochemical energy systems to adopt unique device structures as opposed to the conventional sandwich configuration

that is incompatible with integrated circuits.[4] These miniaturized energy storage systems are designed to be assembled alongside silicon chip components and are often required to be integrated into a limited footprint area. Therefore, designing the components of energy storage systems, that is, the electrode, electrolyte, and separator, to enable chip-level integration is essential to attaining high electrochemical performance at a small form factor.

The well-established microfabrication-based technologies, such as photolithography and etching, have been used widely to fabricate micro-Electrochemical Energy Storage (EES) devices.[5–8] These processes are mature technologically, able to form high-resolution patterns, and compatible with conventional semiconductor processes. Recent advances in electrode development have included the demonstration of three-dimensional electrode arrays,[9–11] highly porous electrode architectures,[3,6,12] and high surface area electrode scaffolds.[6,13–16] In contrast, electrolyte development has encountered limitations in terms of low conductivity or interfacial reactions which lead to unwanted resistive losses. Our previous work on incorporating mobile Li-ions into the SU-8 matrix produced a photopatternable solid electrolyte, but its low conductivity limited the power of electrochemical devices.[17] In the present paper, we successfully transform the polymeric photoresist into a photopatternable, conformal, porous separator which can spatially confine high conductivity liquid electrolytes, thus enabling higher power performance.

Polyolefin-based films, such as polypropylene (PP) or polyethylene (PE), are typically used as the separators for non-aqueous lithium-ion battery systems due to their excellent electrochemical stability and mechanical integrity.[18] In recent years, there have been extensive efforts at developing these separators with various functionalities, such as the abilities to suppress lithium dendrite growth,[19,20] improve the surface wettability,[21–23] mitigate polysulfide shuttling,[24] and enhance the thermal and mechanical stabilities of the separators.[25,26] While separator advancements have primarily focused on improving properties of traditional 2D membranes used

in standard battery formats (coin cell, pouch cell, and jelly roll), creating separators designed for micro-EES devices has received virtually no attention despite the growing demands of the IoT industry.[1] Current energy storage devices utilizing semiconductor processes take the form of either planar interdigitated electrodes or three-dimensional arrays.[4,9,27] A separator for these architectures thus needs to provide 1) spatial control to form consistent thickness 2) good adhesion to the electrode 3) sufficient porosity to allow for facile ion transport and 4) conformal coverage to prevent electrical shorts. Due to the unique set of requirements for micro-EES devices, separators used in traditional battery formats are insufficient and non-transferable, highlighting the critical need to develop new approaches suitable for on-chip EES.

In the present work, we modified the chemistry of SU-8, an epoxy based negative photoresist, by adding a miscible ionic liquid. After photopolymerizing and post baking the material, an appropriate solvent preferentially removes the ionic liquid component, leaving an interconnected porous network of SU-8. The electrochemical performance of devices using photopatterned separators is compared to traditional separators and validated in half and full cell formats. The photopatterned porous separators possess good chemical and electrochemical stability during battery operation in addition to maintaining stability in contact with both lithium metal and silicon. In addition to demonstrating the operation of the photopatterned separator in 2D device formats, these SU-8 separators were also fabricated onto 3D post arrays, thus exhibiting the ability to form a conformal coating over three-dimensional architectures. The development of a photopatternable separator enables high conductivity to be obtained in small dimensions, thus overcoming the resistive losses which have limited progress in the field of miniaturized energy storage systems. Moreover, this approach is broadly applicable to systems beyond the Li-ion batteries presented in this work.

Chapter 5.2. Experimental Methods

Materials

1-Ethyl-3-methylimidazolium-bistrifluoromethanesulfonylimide ([EMI][TFSI], 99.9% purchased from Solvionic), Acetone (99.5%, purchased from Sigma-Aldrich), SU-8 3010 (purchased from MicroChem), Lithium perchlorate ($LiClO_4$, battery grade, dry, purchased from Sigma-Aldrich), Propylene carbonate (anhydrous, 99.7%, purchased from Sigma-Aldrich), Lithium Iron Phosphate (200 nm, purchased from SkySprings NanoMaterials), Super P (99%+, Alfa Aesar), Polyvinylidene fluoride (purchased from Kynar), 1-Methyl-2-pyrrolidinone (anhydrous, 99.5%, purchased from Sigma), and highly doped silicon wafer (p-type, Boron doped, 0.001–0.005 Ω cm, purchased from University Wafer) were used as received.

SU-8 Sample Preparation

The ionic liquid modified SU-8 photoresist (EMI-TFSI SU-8) was prepared by mixing 50 weight percent [EMI][TFSI] with SU-8 3010 prior to deposition. The precursor [EMI][TFSI]/SU-8 was spin-coated onto substrates. Samples were then soft-baked at 100 °C for 15 min for solvent removal prior to patterning. Features were patterned using a Karl Suss MA6 Contact Aligner and photomask. The films were then postexposure baked at 100 °C for 15 min to crosslink the material. To obtain the porous SU-8 network, the ionic liquid phase of [EMI][TFSI]/SU-8 was washed out via solvent exchange in a supercritical dryer. To do this, the [EMI][TFSI]/SU-8 samples were first immersed in acetone. The acetone is then removed through supercritical drying with CO_2 at 40°C and 1,300 psi.

Characterization Methods

Nitrogen adsorption–desorption isotherms were measured at –196 °C on an accelerated surface area and porosity analyzer (Micromeritics Instruments Corp. ASAP2020 Plus, Norcross,

GA). Specific surface area was calculated using the Brunauer–Emmett–Teller method (BET) based on nitrogen adsorption data in the relative pressure range 0.05–0.3 (P/P_0). SEM of porous SU-8 separators were obtained on a Nova NanoSEM230 (Thermo Fisher Scientific) with an Noran System 7 EDX analyzer (Thermo Fisher Scientific). To reduce charging from the electron beam, samples were sputtered with Au/Pd for 45 secs at a pressure of 150 mTorr and 40 mA current using a Denton Desk II Sputter. Transmission electron microscopy (TEM) of the porous separators was obtained on a FEI Tecnai T12. Porous separator films were scraped from the substrate, ground into a powder, suspended in ethanol (1 mg/mL), and drop cast onto the TEM grid. Contact angle measurements were obtained on a FTA125 contact angle goniometer (First Ten Ångstroms Inc., Portsmouth, VA, USA). FTIR spectroscopy was carried out using a Jasco-6100 with a 4 cm^{-1} spectral resolution from 4000 to 400 cm^{-1}. The spectra were averaged over 100 scans. The modulus of the porous separators was measured using an MTS Nano Indenter XP Instrument with a Berkovich tip. Samples were indented a depth of 1000 um across 10 different locations and averaged. Thermogravimetric Analysis (TGA) was conducted on a Perkin Elmer Pyris TGA. Porous separator films were scraped off the silicon wafer and were measured in air using a ramp rate of 10 ℃ min^{-1}.

a-Si Electrode Fabrication and Processing

Amorphous silicon (a-Si) was deposited by electron beam physical vapor deposition (CHA Mark 40, CHA Industries, Fremont, CA, USA) onto stainless steel current collectors with a thickness of 30 nm. Samples were cut into 1x1 cm^2 squares and processed in the steps outlined in Figure 5.1.

Lithium Iron Phosphate ($LiFePO_4$, LFP) Slurry Fabrication and Processing

LFP slurry electrodes were fabricated by mixing LFP, Super P carbon, and PVDF (dissolved in N-Methyl-2-pyrrolidone) in 80:10:10 weight ratios. The slurry was doctor bladed onto a carbon coated aluminum foil. The mass loading was around ~1 mg/cm^2. Due to the porosity of the slurry electrode, LFP samples were spin coated with [EMI][TFSI]/SU-8 solution and soft baked for 10 minutes and repeated three times prior to UV exposure to allow for the monomer solution to fill inside the pores and also coat the top surface of the electrode. For the slurry electrodes, samples were directly pumped into a glovebox after the post bake procedure and solvent exchanged in 1M $LiClO_4$ in PC for a total of 3 times within a 24 hour period.

Silicon Post Electrode Fabrication and Processing

Silicon post arrays were fabricated using semiconductor processing techniques. Details of the materials synthesis were described in a previous publication.[7] Briefly, a photopatterned SiO_2 etch mask was formed using plasma-enhanced chemical vapor deposition (STS Multiplex CVD) and AZ5214 photoresist (MicroChemicals). The exposed silicon was then anisotropically etched using deep reactive-ion etching (Plasma-Therm DSE II) to form silicon posts. The geometry of silicon post arrays was designed to have 100 μm diameter, 150 μm height, and 200 μm pitch. To photopattern porous separators on the 3D posts, a two-step exposure process was conducted. In short, the first exposure ensured that a conformal separator on the bottom layer was polymerized while the second exposure photopatterned the side walls and top of the 3D posts. Concerning the electrochemical testing of 3D electrodes, we previously demonstrated good cyclability of the Si array by avoiding full lithiation.[7] The volume expansion and pulverization of Si posts upon lithium alloying reactions were minimized by limiting the amount of lithiation to 10%, which provides a gravimetric capacity comparable to that of graphite. Because lithium diffuses

into silicon, the volume expansion associated with 10% lithiation is spread out over the post diameter (100 microns) so that the effective volume increase is < 10%.

Electrochemical Characterization

Electrochemical characterizations were carried out using a Bio-Logic VMP-3 Potentiostat. For Li-ion cells, silicon was used as a working electrode and a lithium foil was used as reference and counter electrodes in a coin cell format. For comparison studies, amorphous silicon thin films with photopolymerized porous separators were compared to ones containing glass fiber separators (Whatman, 200 μm thickness). The electrolyte used in this study was 1M $LiClO_4$ in PC. Electrochemical impedance spectroscopy (EIS) was performed between 1 MHz and 5 mHz using a 10 mV amplitude and 0 V bias. The electrolyte/separator property was evaluated in a 2-electrode coin cell configuration containing two stainless steel electrodes each with the separator deposited directly. Full cell testing for planar electrodes was conducted using an LFP cathode containing excess capacity. The Si thin film was precycled for one cycle to form the SEI at a rate of C/5. Charge is defined by the delithiation of LFP and lithiation of Si while discharge represents the lithiation of LFP and delithiation of Si. 3D silicon posts were tested in a flooded three electrode cell. The posts were tested with and without the conformal SU-8 separator.

Chapter 5.3. Results and Discussion

Chapter 5.3.1. Fabrication of Photopatternable Porous Separators

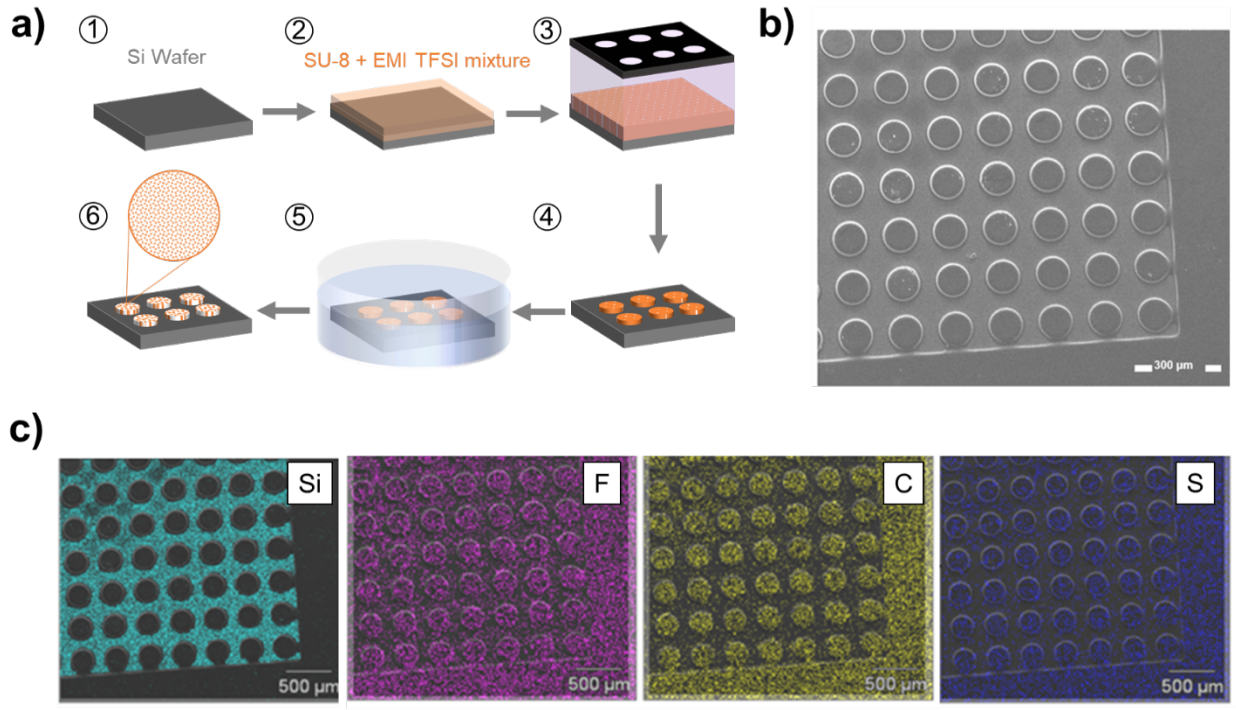

Figure 5.1. a) Process flow for fabricating porous SU-8 separators: 1) spin coating of the [EMI][TFSI]/SU-8 solution 2) a pre bake at 100 °C 3) UV exposure 4) a post-bake at 100 °C 5) acetone solvent exchange to remove the [EMI][TFSI] from the porous SU-8 matrix 6) CO_2 supercritical drying to preserve microstructure. b) SEM of a photopatterned circle array on a silicon wafer using a 50 wt% [EMI][TFSI] SU-8 solution. The diameter of each circle is 100 µm. c-f) EDX spectral maps showing that the [EMI][TFSI] is locally confined in the polymerized SU-8 matrix.

The process for fabricating the porous SU-8 separators is shown in Figure 5.1a. The [EMI][TFSI] and SU-8 monomer are completely miscible and were mixed to various weight percentages of [EMI][TFSI]. Upon UV exposure, photoacid generators are activated within the

exposed regions of the composite film, which initiates the protonation of the epoxy groups of the SU-8 monomer. This initial crosslinking step is further propagated by the application of heat, leading to chains of epoxy ring opening reactions that result in the formation of an ether-based polymer network. This polymerization process can be observed optically by the transparent to translucent transition of the film, resulting from the formation of a sub-micron-scale porous network (Figure 5.2). Once the post-exposure bake is complete, the resulting film consists of an interconnected, bicontinuous matrix composed of a solid SU-8 phase and an ionic liquid phase. The non-uniform microstructures for the [EMI][TFSI]/SU-8 are consistent with the presence of separate phases. The photopatterning capability of the SU-8 matrix is preserved with the incorporation of 50 wt% [EMI][TFSI] as evident in Figure 5.1 b whereby each circle has a diameter of 100 μm. Furthermore, the local sulfur and fluorine signals in Energy-dispersive X-ray spectroscopy (EDX) confirm that the ionic liquid within the polymerized SU-8 regions can be spatially confined (Figure 5.1 c).

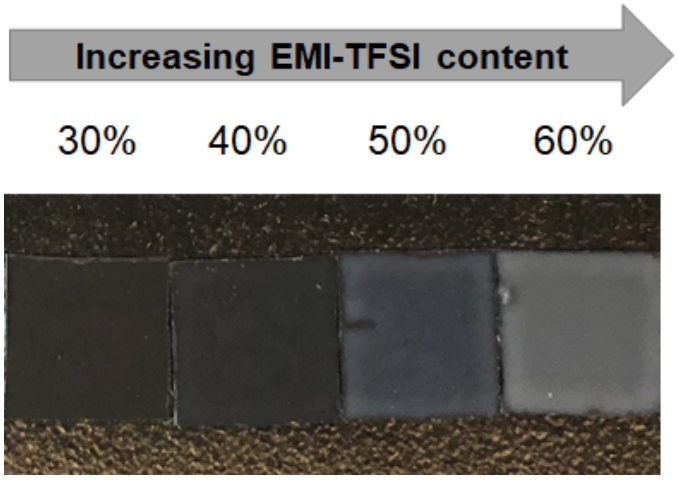

Figure 5.2. Photograph of SU-8/[EMI][TFSI] films after 10 minute post exposure bake at 100 ℃ as a function of [EMI][TFSI] wt%.

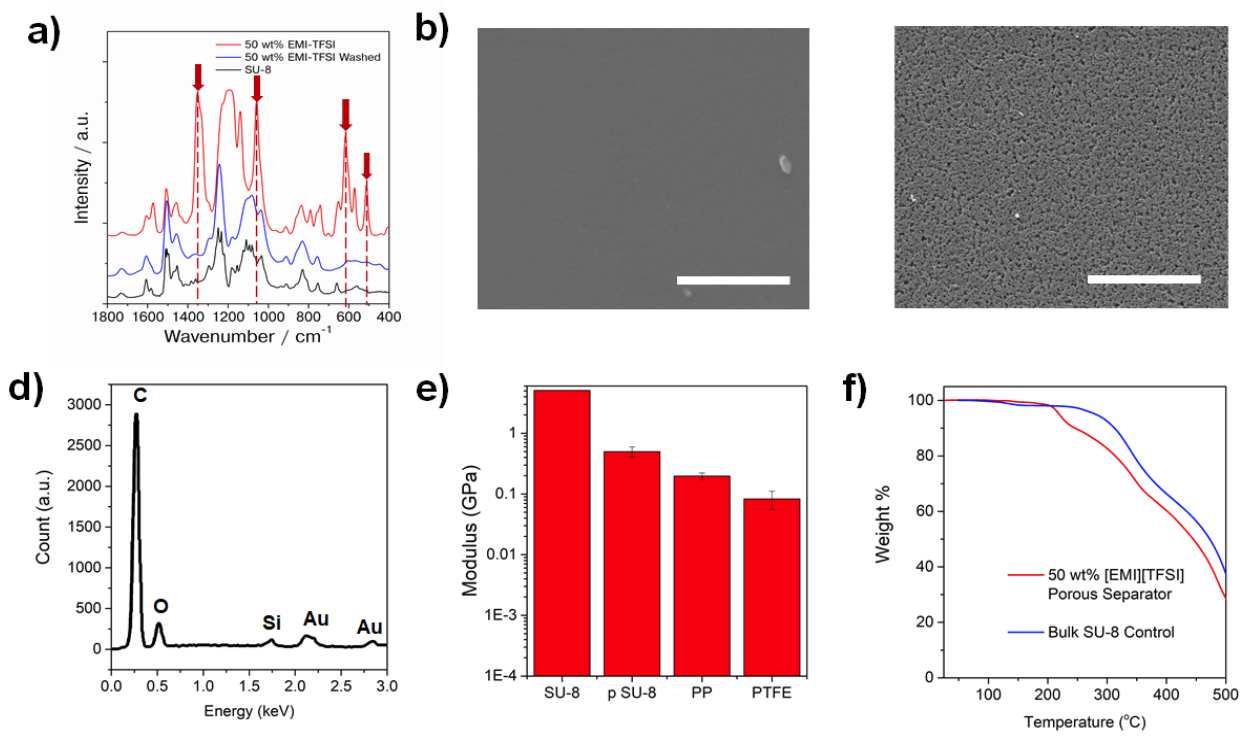

Figure 5.3. a) FTIR of a 50 wt% [EMI][TFSI]/SU-8 film before and after ionic liquid removal. Upon removal of ionic liquid, the absorbance bands of the TFSI anions (red dashed lines) disappear indicating the complete removal of ionic liquid from the porous SU-8 matrix. b-c) SEM image of porous separator (b) before (c) and after ionic liquid removal. Upon acetone solvent exchange and CO_2 supercritical drying, the porous SU-8 network is revealed. The scale bar is 10 μm. d) EDX of Figure 5.3c shows that the ionic liquid is completely removed (absence of fluorine and sulfur signals) and only the carbon and oxygen signals from the SU-8 matrix remain. Si signals are from the substrate and Au signals are from sputtering to minimize charging from the electron beam. e) Elastic modulus of neat SU-8[17], 50 wt% [EMI][TFSI] porous separator, polypropylene (PP)[30] and Polytetrafluoroethylene (PTFE)[30] separators measured using nanoindentation. f) TGA profiles for a 50 wt% [EMI][TFSI] porous separator and a bulk SU-8 control. The porous separator can withstand temperatures up to 219 °C with only 5% weight loss.

Removal of the ionic liquid by an acetone solvent exchange, followed by CO_2 supercritical drying, leads to the formation of a three-dimensional porous morphology (Figure 5.3 b-c). The supercritical drying of the liquid phase was necessary to avoid the collapse of the pore network as the supercritical liquid loses all surface tension and can no longer exert capillary stress. Optically, the removal of ionic liquid from the film can be observed by a translucent to opaque transition due to scattering events throughout the microstructure. The complete removal of the ionic liquid was confirmed by the disappearance of fluorine and sulfur signals from [EMI][TFSI] and the retention of carbon and oxygen signals in EDX (Figure 5.3d). This can be further confirmed by the disappearance of characteristic absorption peaks of EMI-TFSI after the solvent treatment (Figure 5.3a). For the 50 wt% [EMI][TFSI] sample shown in Figure 5.3c, the porosity was determined to be 59.5 ± 0.8 % based on density comparisons between the porous SU-8 and 100% dense SU-8 film in Table 5.1. Porosity calculated from BET matched well with these values and was estimated to be around 55% with a surface area of 248 ± 7.2 m^2/g. The porosity of the 50 wt% [EMI][TFSI]/SU-8 falls within the target porosity between 40-60 % designed for lithium-ion battery separators,[28] and is on par with the porosity values of the commercially available Celgard 2500 separator.[29]

Table 5.1. Porosity values for 40-60 wt% [EMI][TFSI] samples (n=3).

Each sample was processed as outlined in Figure 5.1. Upon acetone solvent exchange and supercritical drying, the samples were weighed, and the mass of the substrate was subtracted to obtain the mass of the porous separator film. The density of the porous separator ($\rho_{\text{porous separator}}$) was calculated by dividing the mass of the porous separator by the volume of the separator which was calculated by multiplying the area of the sample by the thickness values obtained in Figure 5.4. The porosity of the film was calculated by comparing the density of the porous film with the

density of bulk SU-8 ($\rho_{SU\text{-}8\ 3010}$ =1.106 g cm^{-3}). The percent error refers to the standard deviation of porosity values obtained from 3 separate samples.

% [EMI][TFSI]	Porosity [%]	Error (+/-) [%]
40	41.9	0.2
50	59.5	0.8
60	69.5	1.0

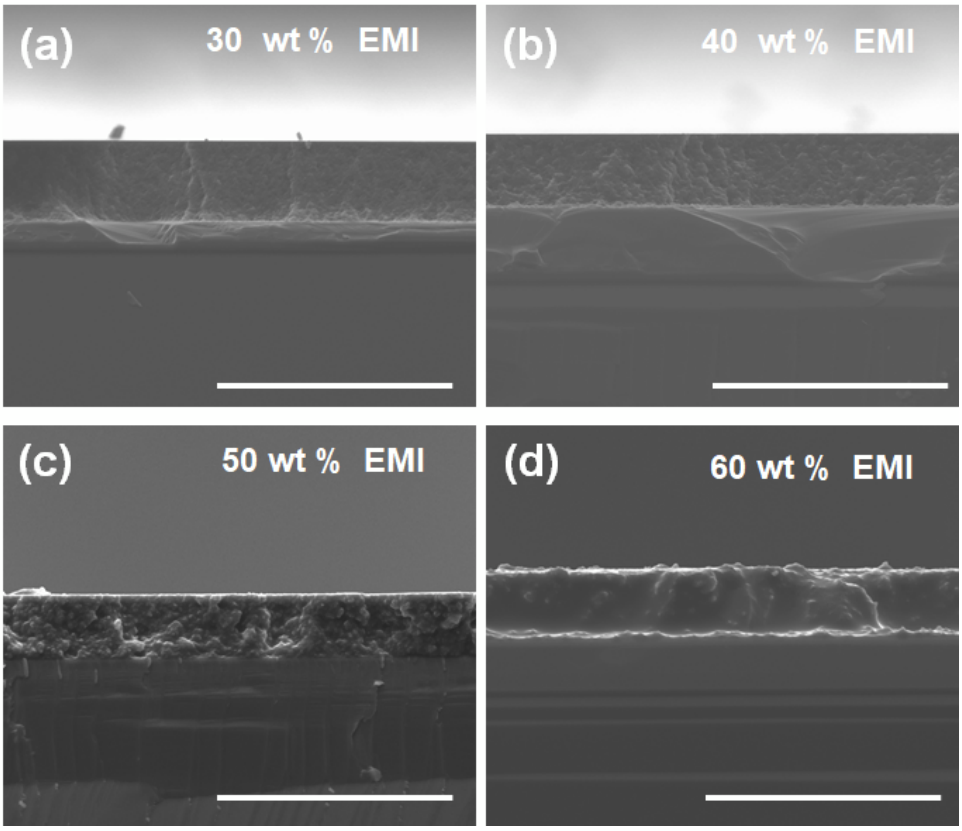

Figure 5.4. Cross Section SEM of [EMI][TFSI]/SU-8 ionogel as a function of [EMI][TFSI] wt% a) 30 wt% [EMI][TFSI] b) 40 wt% [EMI][TFSI] c) 50 wt% [EMI][TFSI] d) 60 wt% [EMI][TFSI]. At 60 wt% the [EMI][TFSI] is the dominant phase and the smooth morphology is attributed to the ionic liquid phase. Scale bar for each image is 30 μm. Spin coat speed is 3000 rpm. The

thicknesses of the 30-60 wt.% [EMI][TFSI] samples are 9.91 ± 0.13 µm , 9.12 ± 0.10 µm, 7.69 ± 0.13 µm, and 5.71 ± 0.15 µm, respectively.

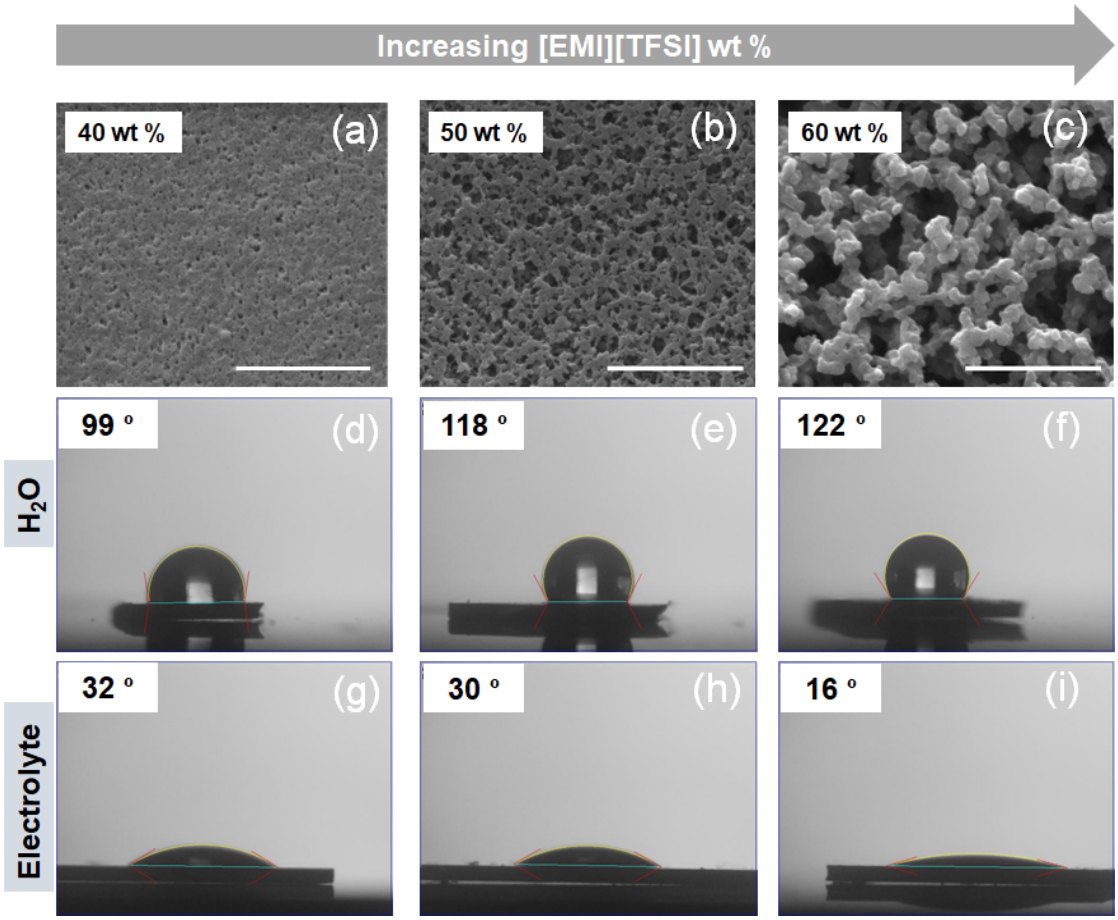

Figure 5.5. Plan view SEM of a) 40 b) 50 and c) 60 wt% [EMIM][TFSI] samples spin coated onto a silicon wafer. Scale bar is 3 µm. d-f) Contact angle measurements using water as the solvent for 40, 50, and 60 wt% [EMIM][TFSI] porous SU-8 samples demonstrating the hydrophobic property of SU-8. The contact angle increases with increasing porosity. g-i) Contact angle measurements using propylene carbonate (PC), the electrolyte solvent used in electrochemical testing, for 40, 50, and 60 wt% [EMIM][TFSI], respectively.

The pore properties of SU-8 based separators can be readily tuned based on the ratio of ionic liquid to SU-8 monomer. Varying the [EMI][TFSI] wt% in the SU-8 mixture prior to UV

exposure resulted in large differences in pore structures for the 40-60 wt% [EMI][TFSI] range (Figure 5.5, Figure 5.4). We note that 30 wt % [EMI][TFSI] resulted in small pores that could not be resolved in SEM while porosity above 70 wt % [EMI][TFSI] resulted in poor mechanical integrity due to the dominant volume fraction of the ionic liquid phase. From density measurements, the porosity of the 40, 50, and 60 wt% [EMI][TFSI] samples were calculated to be 41.9 ± 0.2 %, 59.5 ± 0.8 %, and 69.5 ± 1.0 % (Table 5.1). From SEM image analysis, the average pore sizes for 40, 50 and 60 wt% [EMI][TFSI] were approximately 33, 116, and 287 nm, respectively (Figure 5.6). By increasing the ionic liquid wt%, the free volume in the separator is effectively increased, resulting in larger pores and higher porosity upon ionic liquid removal (Figure 5.5). For Li-ion battery separators, the pore size is generally targeted to be < 1 μm to help prevent lithium dendrite penetration through the separator.[18,28] In the current study, the 50 wt% [EMIM][TFSI]/SU-8 presents the best overall properties due to its high porosity, sub-micron pores, and good mechanical integrity (*vide infra)*. The ability to control the film thickness as a function of spin coating speed is shown in Figure 5.7.

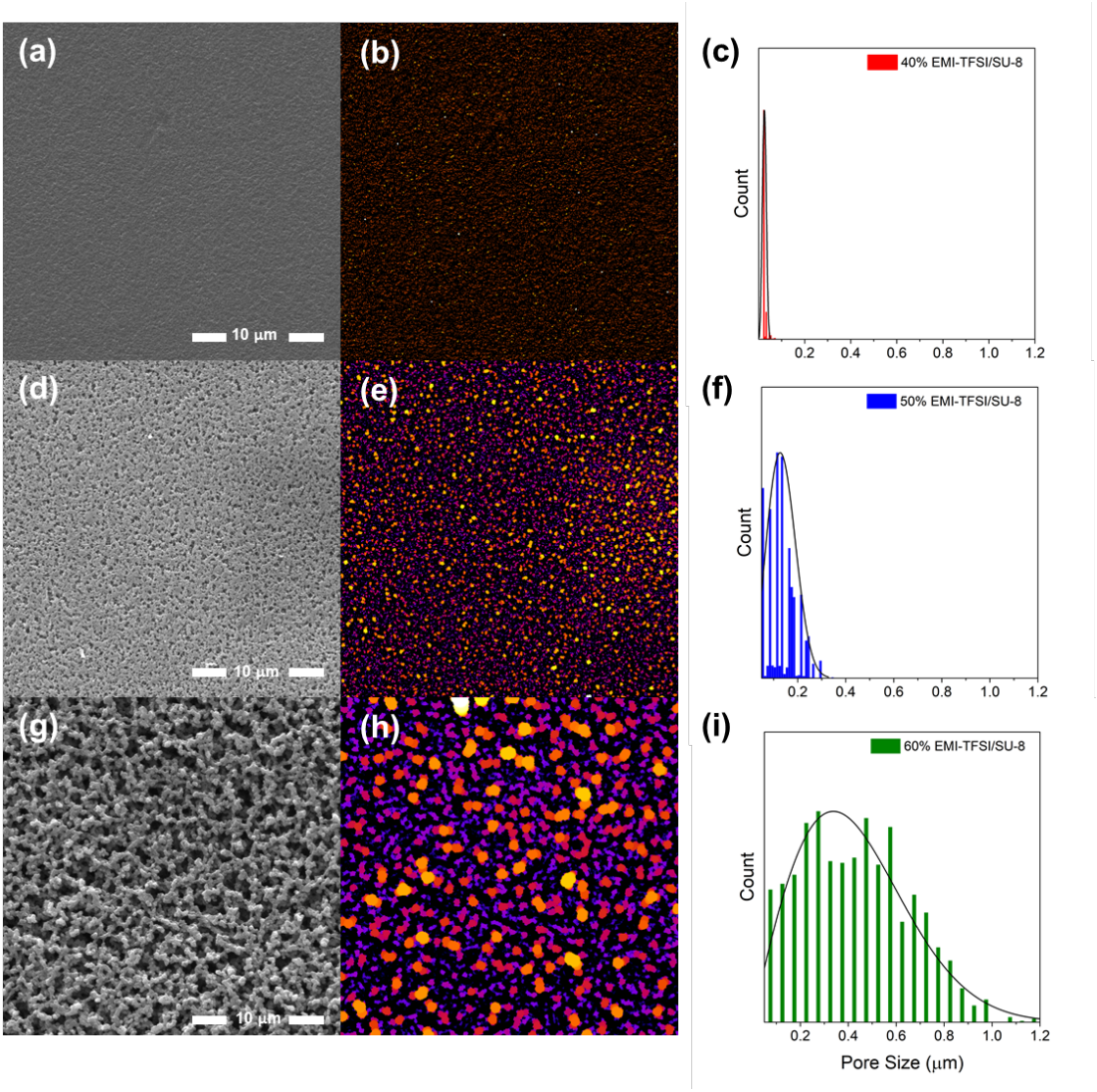

Figure 5.6. Pore size distribution analysis of (a-c) 40 wt%, (b-f) 50 wt%, and (g-i) 60 wt% [EMI][TFSI] porous separators. SEM images of the porous separators are shown in (a,d,g) while the corresponding pore size analysis images are shown in (b,e,h). The pore size distributions are shown in (c,f,i). The average pore sizes for 40, 50 and 60 wt% [EMI][TFSI] were approximately 33, 116, and 287 nm, respectively. The image analysis computes the local thickness of the SEM images by evaluating the diameter of the largest sphere that fits inside the pore and contains the voxel. The number of voxels with respective local thickness values and the corresponding pore sizes were then obtained.

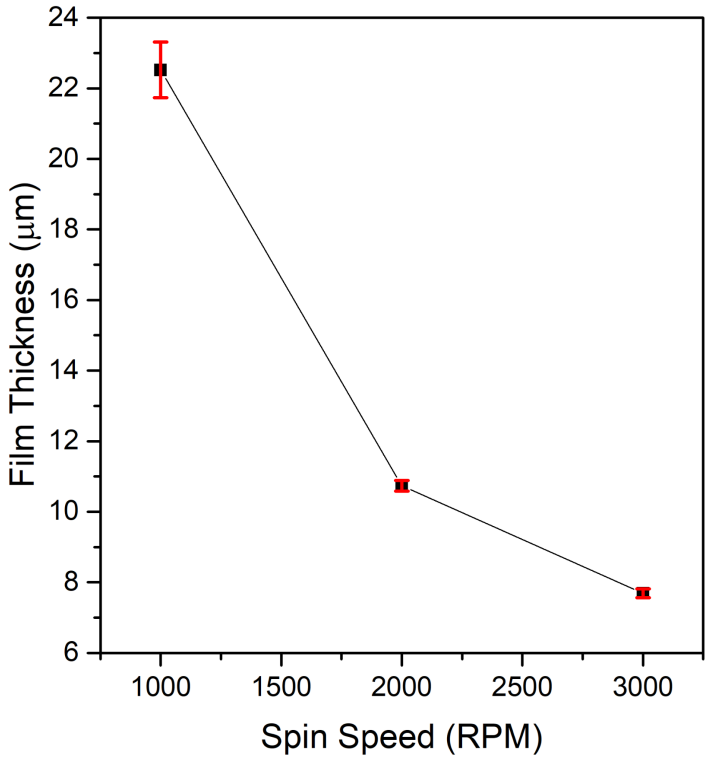

Figure 5.7. Spin coater speed vs film thickness for 50 wt% [EMI][TFSI]. The thickness of the photopatternable separator can be tuned as a function of spin coating speed. Moreover, it is possible to obtain thinner films by further diluting the SU-8 prepolymer solution in cyclopentanone, while thicker films can be obtained by using a higher viscosity SU-8 photoresist, such as SU-8 3050. Error bars correspond to the standard deviation across 5 samples.

The wetting behavior of an electrolyte on the separator has a significant effect on electrochemical performance. When the wettability of a separator is insufficient, the pores in a separator are not completely saturated with liquid electrolyte. Charge storage properties are limited as Li ions do not have full access to the redox active material. In addition, impeding Li-ion transport leads to higher cell resistance. The wetting properties of porous SU-8 separators were evaluated through contact angle measurements (Figure 5.5). The hydrophobic properties of SU-

8 are further enhanced in the porous SU-8 as is evident by the increasing contact angle with increased porosity. However, the porous separator demonstrates good wetting behavior with solvents such as propylene carbonate, and wettability is further enhanced in the higher [EMI][TFSI] wt% samples. As the porosity of the separator increases, the observed surface roughness of the separator also increases, improving wettability.[31] While the addition of $LiClO_4$ salt into propylene carbonate should alter the wetting properties, prior research has shown the changes to be quite small and will not affect the overall wetting behavior. [32]

Chapter 5.3.3. Thermal and Mechanical Characterization of Porous Separators

The thermal and mechanical properties of separators are critical in order to withstand the temperature excursions and physical stresses during cell assembly, operation, and under abuse conditions. During operating conditions, the battery separator experiences mechanical deformation due to external compression, expansion/contraction of the electrodes and local heating associated with the electrochemical reactions. Commercial separators of polypropylene (PP) and polyethylene (PE) demonstrate an acceptable elastic modulus near room temperature but are known to suffer from low glass transition temperatures (165 °C and 135 °C, respectively).[33] While additional modifications, such as the incorporation of ceramic coatings[34,35] and multilayer structures,[18] can help improve thermal stability and safety, it comes at the expense of increased processing and cost. One of the well-known features of SU-8 photoresist is its excellent thermomechanical stability upon crosslinking which is reflected by its high glass transition temperature (~200 °C)[36] and elastic modulus of 5.1 GPa.[17] Thermogravimetric analysis (TGA) indicates that SU-8 readily withstands 200°C before it begins to undergo thermal decomposition (Figure 5.3f) demonstrating 5% weight loss at 219 ℃ . The introduction of porosity from the 50 wt% [EMI] [TFSI] addition has little effect on thermal stability. This response is not surprising as studies of porous epoxy foams have found that introducing porosity in the polymer

has minimal influence on the glass transition temperature.[37] In contrast, porous materials, such as aerogels, exhibit lower elastic modulus as this property scales with ρ^3, where ρ is the density of the non-porous material.[38] Thus, it is not surprising that the elastic modulus determined by nanoindentation measurements for a 50 wt% [EMI][TFSI] separator is found to be 0.5 GPa. Nonetheless, this value is as much as 5 times higher than traditional polypropylene (PP, 0.1-0.2 GPa) and polytetrafluoroethylene (PTFE, <0.1 GPa) porous separators (Figure 5.3e).[30]

Chapter 5.3.4. Electrochemical Validation of Photopatternable Porous Separators

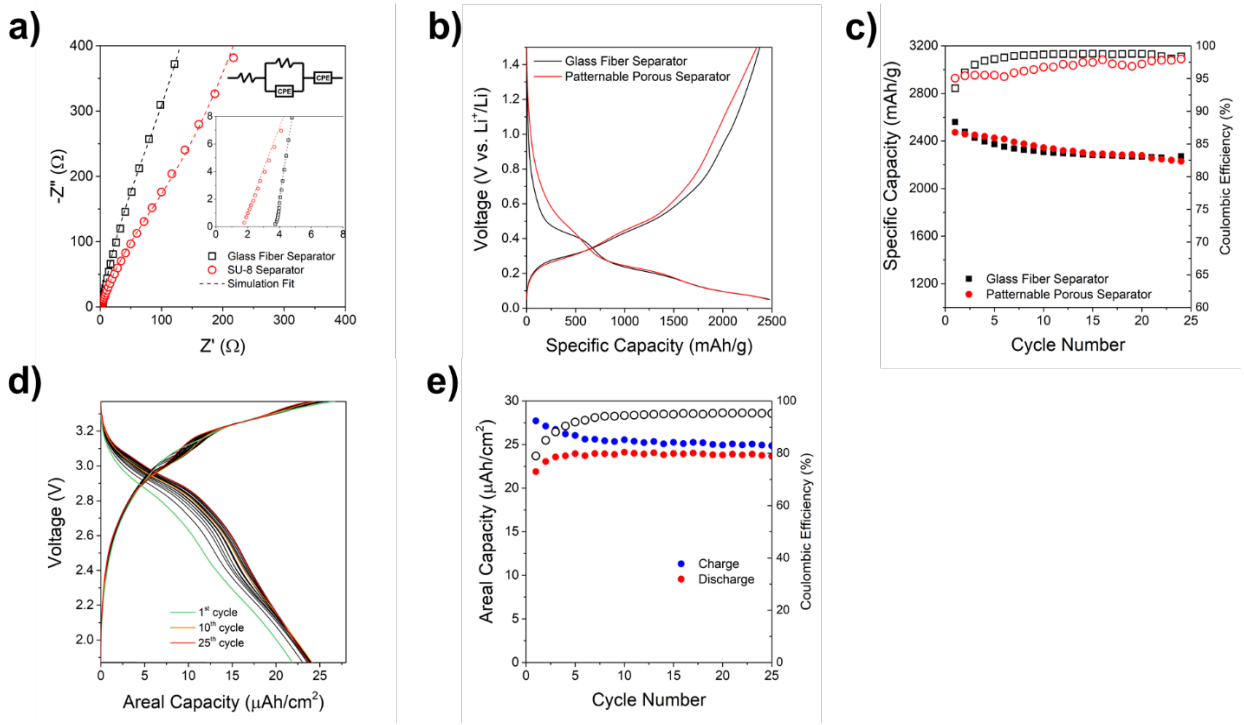

Figure 5.8. a) Impedance spectra for glass fiber separator and porous SU-8 separator saturated with a liquid electrolyte (1 M $LiClO_4$ in PC) along with the corresponding equivalent circuit. Inset: Expanded view of the impedance spectra showing the high frequency Z' intercept. b) Galvanostatic measurements of the amorphous Si thin film half cell showing lithiation and delithiation at C/5 (5 μA cm^{-2}). Similar galvanostatic profiles are obtained for both the SU-8 porous separator and glass fiber separator. c) Specific capacity and coulombic efficiency of the

amorphous Si/porous SU-8/Li metal and amorphous Si/ Glass fiber/Li metal coin cells cycled at a C/5 rate for 25 cycles. d) Charge-discharge characteristics for the full cell of amorphous Si|porous separator|LFP cycled at C/5 (5 μA cm^{-2}) for 25 cycles. e) Areal charge/discharge capacities and coulombic efficiency for 25 cycles for the full cell shown in (d) above. A charge is defined as the delithiation of LFP and lithiation of the Si.

We carried out a series of experiments designed to evaluate the effectiveness of the SU-8 porous separator in electrochemical measurements. These experiments include electrochemical impedance spectroscopy (EIS), cycling of lithium in Si anodes and the operation of a full cell consisting of an amorphous silicon anode (a-Si) and $LiFePO_4$ (LFP) cathode. The EIS for the 50 wt% [EMI][TFSI] porous SU-8 filled with a Li-ion electrolyte (1M $LiClO_4$ in propylene carbonate) was conducted in a two-electrode configuration. The SU-8/50 wt% [EMI][TFSI] precursor was deposited and processed (UV polymerization, ionic liquid removal) directly on the stainless steel current collector. The complex impedance plot is that of a liquid electrolyte with the high-frequency Z′ intercept representing the bulk ionic resistance of liquid electrolytes (Figure 5.8a). This response is comparable to that of a glass fiber separator. When the geometry of the given separators was considered, the ionic conductivities obtained from the porous SU-8 and glass fiber control were consistent ($\sigma = 5 \cdot 10^{-3}$ S cm^{-1}) and agreed well with literature values.[39,40]

The evaluation of the photopatternable membrane as a separator in a half-cell configuration with an amorphous Si electrode was carried out using a 10 μm thick 50 wt% [EMI][TFSI]-based porous SU-8 separator paired with a 30 nm silicon thin film. The 30 nm thin-film a-Si electrode has previously been demonstrated to be stable under repeated cycling, while thicker a-Si films have been shown to pulverize due to the tensile stresses developed during delithiation.[41,42] The fabrication of the electrode/separator structure is significantly different from that of a traditional half-cell with a standard separator. First, the deposition of a-Si on a stainless

steel substrate takes place, followed by spin coating the SU-8/50 wt% [EMI][TFSI] precursor which is then processed to polymerize the SU-8 and remove the ionic liquid phase. In this way, the porous separator is firmly attached to the a-Si electrode with its area spatially defined by the patterning protocol. The electrochemical testing was carried out using a standard 2-electrode coin cell configuration with lithium metal as the counter electrode and 1M $LiClO_4$ in PC electrolyte. The room temperature Li-ion charge storage mechanism for amorphous silicon can be described as a two-step lithiation reaction where a-Si is lithiated to form a-Li_xSi (x~2.5) followed by the formation of an a-Li_xSi (x~3.75) phase.[43] The galvanostatic charge and discharge characteristics at a C/5 rate (5 μA cm^{-2}) are virtually identical to that of a comparable cell with a glass fiber separator (Figure 5.8 b-c). Cycling studies demonstrate no significant differences in capacity for 25 cycles with a gravimetric capacity over 2200 mAh g^{-1} on the 24th discharge (Figure 5.8d). The corresponding areal capacity for the a-Si thin film was determined to be ~25 μAh cm^{-2} from a cyclic voltammetry measurement (Figure 5.9). Cyclic voltammetry was also used to assess the electrochemical stability of the Li|porous separator and Si|porous separator interfaces. The CV of an a-Si|porous separator|Li cell demonstrated nearly identical peaks as the glass fiber control (Figure 5.9 and Figure 5.10). The similarity of the glass fiber control and porous separator CVs indicates that the peaks observed in the first cycle originate from SEI formation of the a-Si electrode[44,45]. The slight capacity decay observed in the silicon thin films in both separator systems (Figure 5.8c) are the result of both surface-related side reactions and other undesirable redox reactions occurring at the stainless-steel substrate as previously reported in a study using the same electrolyte system and film thickness.[46] Overall, the experimental measurements establish that the porous SU-8 exhibits the most important separator properties, that of demonstrating good ion transport properties, high chemical and electrochemical stability against lithium metal and lithiated silicon, and preventing electrical short-circuits between the cathode and anode. The electrochemical validation of 2D a-Si electrode with the porous SU-8 separator also

indicates that the photopatternable separator approach can be effectively extended to crystalline silicon electrodes, which can be processed via microfabrication techniques (*vide infra*).

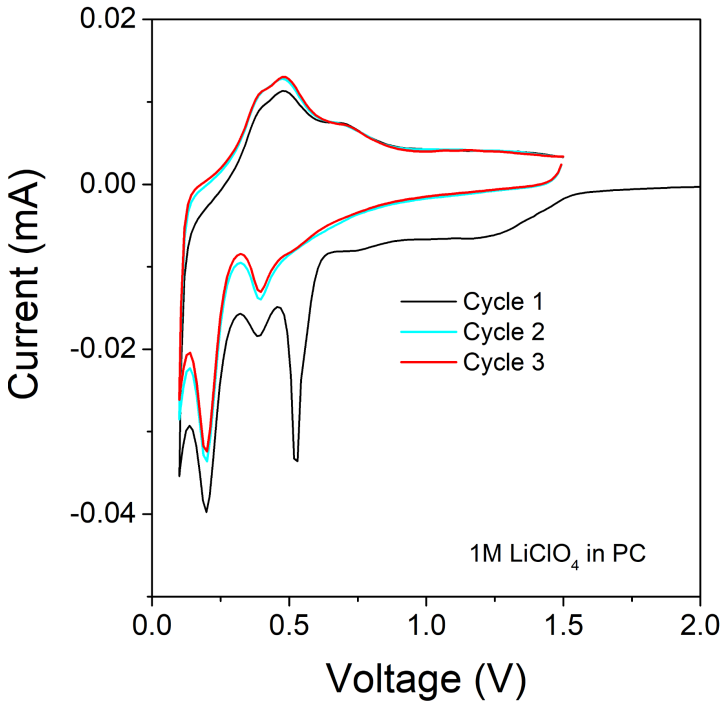

Figure 5.9. Cyclic voltammogram of a-Si thin film cycled at 0.1 mV s^{-1} using a glass fiber separator in 1M $LiClO_4$. Beyond the initial cycle, the a-Si demonstrates good reversibility shown by the similar CV curves for cycle 2 & 3. The areal capacity used in this study was obtained by integrating current (mA) vs time (hr) plot for the second cycle (~25 µAh cm^{-2}).

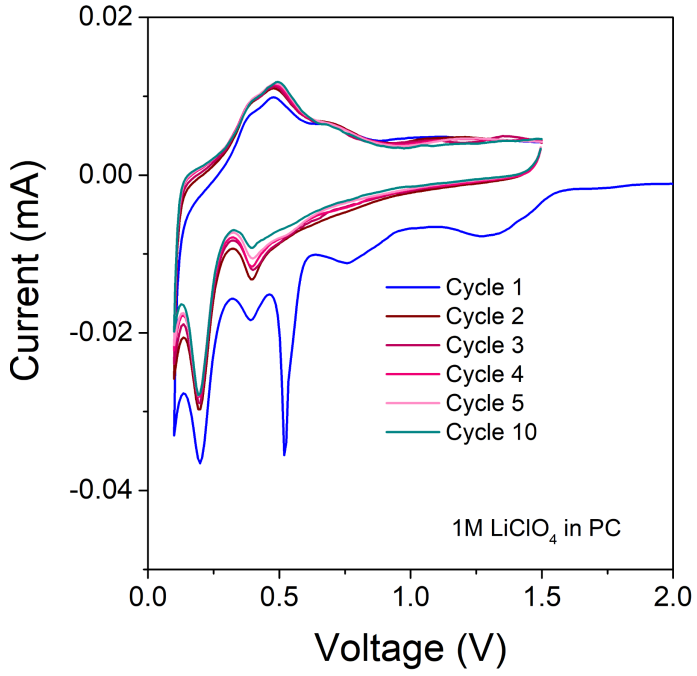

Figure 5.10. CV of an amorphous silicon thin film with a 50 wt% [EMI][TFSI] photopolymerized porous separator coin cell with lithium metal counter electrode. Lithium metal is in direct contact with the porous separator. Scan rate is 0.1 mV/s.

The photopatternable porous separator was also tested in a full cell using a-Si as a thin film anode with a LPF cathode and cycled at C/5 (5 μA cm^{-2}) based on the capacity of the a-Si electrode (Figure 5.9). In these experiments, both the a-Si and LFP were processed similarly to the half-cell mentioned above, so that the porous separator was attached to each electrode. Half-cell testing of a LFP electrode with a photopolymerized porous separator showed reversible CV peaks with no new peaks upon cycling indicating good electrochemical stability of the separator/LFP interface (Figure 5.11). After the first few cycles, the coulombic efficiency stabilized and by the 25th cycle, CE was ~95% reaching an areal capacity around 24 μAh cm^{-2}. This value is in good agreement with the areal capacity of the a-Si half-cell. These results demonstrate that

processing the porous SU-8 separator is compatible with traditional slurry-cast electrodes and that the resulting electrode/porous separator integration is an effective route for fabricating battery structures. This integration distinguishes the SU-8 separator from traditional polymer separators which constitute mobile components that are detached from the electrode. Here, the strong adhesion and chemical inertness provided by SU-8 photoresist chemistry[36] effectively integrates the electrode and separator into a single structure.

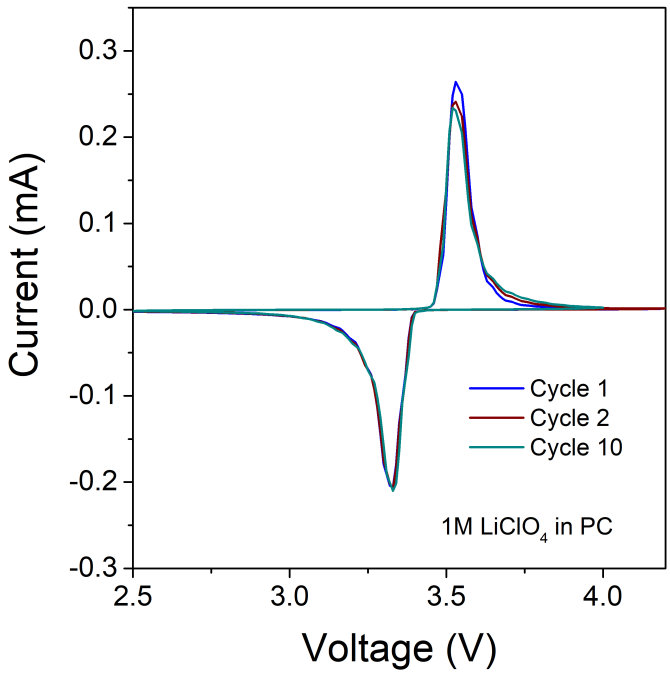

Figure 5.11. CV of an LFP electrode with a 50 wt% [EMI][TFSI] photopolymerized porous separator in 3 electrode experiment with lithium counter and reference electrode at a scan rate of 0.1 mV/s.

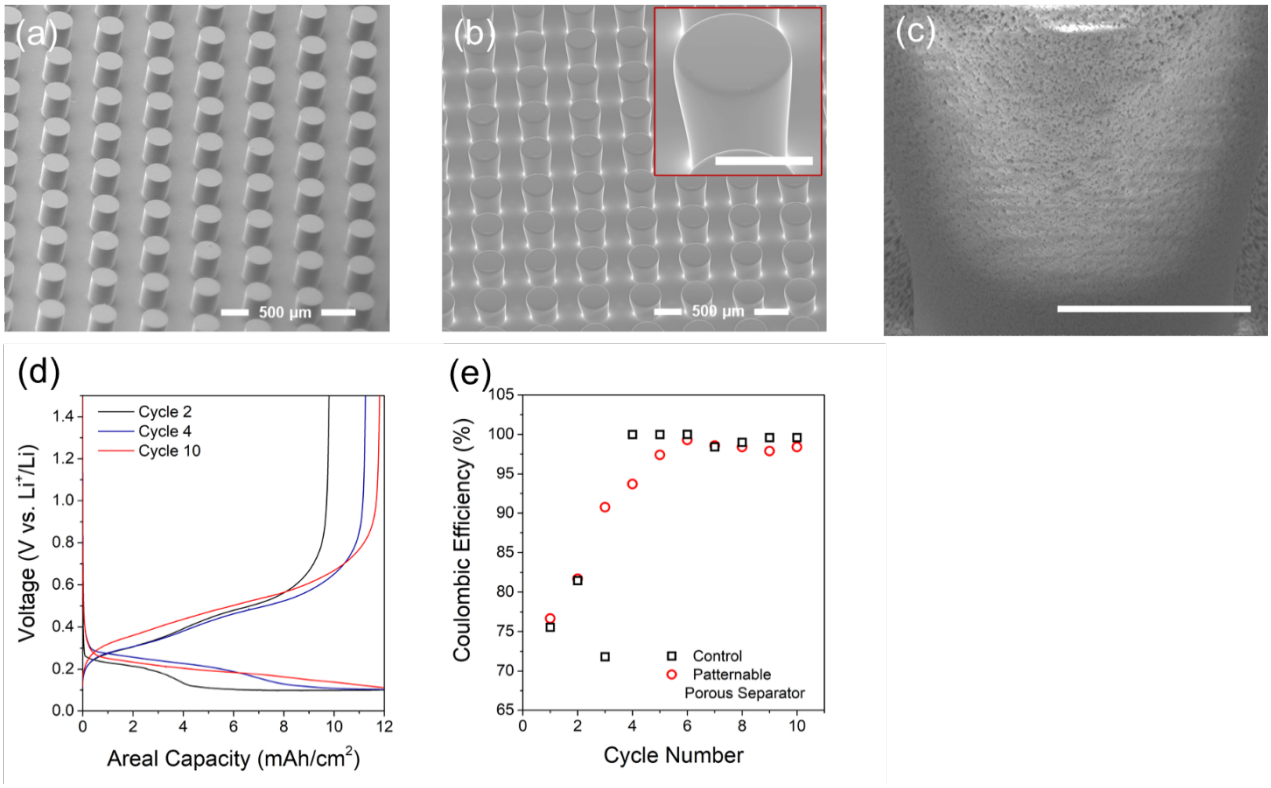

Figure 5.12. SEM images of (a) bare silicon array and (b) silicon array coated with the [EMIM][TFSI] modified photopatternable SU-8 electrolyte. Each silicon post represents 100 µm diameter with 150 µm in height and 15 µm thick SU-8 layer. Inset in (b) shows close up of the conformal separator on the Si post after photopatterning. Scale bar for the inset image is 100 µm. c) Expanded view of the highly porous surface once the ionic liquid has been removed. The scale bar is 50 µm. d) Galvanostatic profile of the separator coated 3D silicon array with a lithium counter and reference electrode and 1M $LiClO_4$ in propylene carbonate as an electrolyte. e) Comparison plot of the coulombic efficiency of silicon post arrays with and without porous separator coating.

The purpose in fabricating the planar a-Si films is to provide validation of the porous separator in the Li-ion battery environment; the low mass loading of a-Si precludes viable applications. However, with silicon microfabrication methods, there is the opportunity to create non-planar configurations, such as the post array geometry investigated in the current study which increases the areal energy density significantly. The advantages of utilizing microfabrication-prepared silicon post arrays are that it offers highly reliable, high-throughput wafer-scale fabrication of 3D microbattery arrays and ease of co-packaging with other integrated circuits. In addition, the high values of gravimetric and volumetric energy densities for crystalline silicon are such that approximately 10% lithiation of the theoretical capacity for silicon is comparable to the gravimetric capacity of graphite and thus sufficient to operate a full cell Li-ion system. A limited degree of lithiation also reduces volume expansion from the conversion-type phase evolution process and allows for stable cycling of silicon without pulverization.[7] In previous work, we showed that photopatterning of nonporous SU-8 around 3D silicon posts proved to be an effective approach in forming a conformal solid electrolyte over high-aspect-ratio structures. However, the low ionic conductivity of nonporous SU-8 was on the order of 10^{-7} S cm^{-1} and limited battery performance.[7] To this end, the application of a porous SU-8 separator for nonplanar 3D electrodes offers a unique opportunity to achieve high power and high energy micro-EES systems. Figure 5.12a shows SEM images of silicon post arrays of 100 μm diameter, 150 μm height, and 200 μm pitch. In order to photopattern a conformal separator, a two-step exposure process was used (Figure 5.13). After conformal coating the ionic liquid modified SU-8 (15 μm thick) over the 3D Si arrays, the porous separator structure was developed by the acetone treatment. Upon removal of ionic liquid, the porous morphology of the conformal separator is revealed (Figure 5.12 b-c).

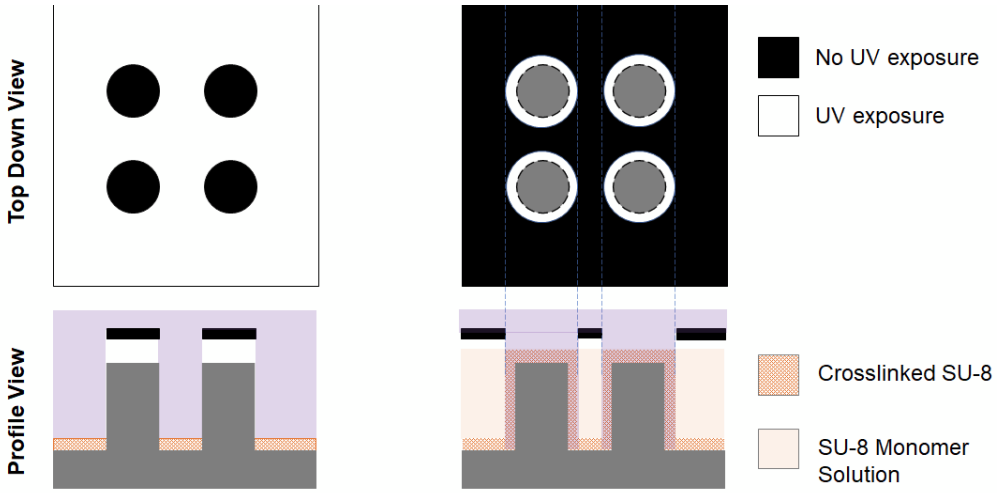

Figure 5.13. Two-part exposure process for patterning conformal separators for Si post array. To conformally coat the separator on the 3D Si post, a two part exposure process was employed. The first step consists of forming a base layer to cover the bottom layer (left) followed by the second step in which the side walls and top of the posts are patterned (right).

The charge storage properties of the separator-coated silicon post arrays were evaluated in a half-cell configuration with a lithium counter and reference electrode and compared to an uncoated silicon array electrode operated under the same conditions. The degree of lithiation of these anode arrays was set to be 12 mAh cm^{-2} in anticipation of having high-capacity cathode materials (180 mAh g^{-1}) fill the cathode volume.[7,47] Galvanostatic profiles of the 3D silicon post arrays cycled at a current density of 1 mA cm^{-2} are shown in Figure 5.12d. It is evident that the silicon arrays take a few cycles to undergo the formation process, in which the stable lithiation front is developed and the solid electrolyte interface layer is formed at the surface of electrodes.[42,48,49] The amorphization of the lithiation front of silicon during the formation process is indicated by the evolution of the sloping voltage profile (Figure 5.12d). A similar trend is observed for the uncoated silicon control sample, suggesting that this behavior is primarily coming from the silicon working electrode rather than the porous separator. By the 6th cycle, both samples exhibit a reversible cycling behavior with a coulombic efficiency of over 98% (Figure 5.12e).

Chapter 5.4. Conclusion

One critical feature which is essential for achieving miniaturized EES is to improve the separator fabrication approaches at micron-scale while maintaining device functionality and reliability. In the current study, we developed a photopatternable porous separator material that can be patterned over multidimensional high-aspect-ratio structures with sub-100 μm resolution. In this novel synthetic approach, an imidazolium-based ionic liquid was used as a templating agent, while the epoxy-based host scaffold facilitated ion transport and provided the photopatterning capability. The photopatterning process was demonstrated with both thin film and slurry cast electrodes. The separator properties of the SU-8 are superior to traditional polyolefin separators in terms of mechanical integrity (modulus of 0.5 GPa) and thermal properties (>200°C). Although the present study was directed at 3D lithium-ion microbatteries, the separator presented here offers opportunities in other systems beyond the one presented here. The outstanding benefit of the SU-8 separator is its photopatterning capability which not only enables non-planar device structures as demonstrated here for 3D lithium ion batteries but also can be adapted and incorporated in other emerging micro electrochemical energy storage systems, such as on-chip supercapacitors and micro fuel cells.[50,51] Devices based on photopatternable porous SU-8 materials potentially offer advantages in high spatial resolution patternability, miniaturization and the scale-up of fabrication processes. Further, porous SU-8 membranes also present opportunities beyond energy storage applications such as microfluidics[52] (i.e. separations and analytical applications) due to their flexible processability, mechanical integrity, and versatile surface chemistry, and biomedical applications[53] for their microstructure tunability and biocompatibility.

Chapter 5.5 References

[1] S. Li, L. D. Xu, S. Zhao, *Inf. Syst. Front.* 2015, *17*, 243.

[2] P. Zhang, F. Wang, M. Yu, X. Zhuang, X. Feng, *Chem. Soc. Rev.* 2018, *47*, 7426.

[3] J. H. Pikul, H. Gang Zhang, J. Cho, P. V. Braun, W. P. King, *Nat. Commun.* 2013, *4*, 1732.

[4] N. A. Kyeremateng, T. Brousse, D. Pech, *Nat. Nanotechnol.* 2017, *12*, 7.

[5] P. Zhang, F. Zhu, F. Wang, J. Wang, R. Dong, X. Zhuang, O. G. Schmidt, X. Feng, *Adv. Mater.* 2017, *29*, 1604491.

[6] H. Ning, J. H. Pikul, R. Zhang, X. Li, S. Xu, J. Wang, J. A. Rogers, W. P. King, P. V. Braun, *Proc. Natl. Acad. Sci.* 2015, *112*, 6573.

[7] J. I. Hur, L. C. Smith, B. Dunn, *Joule* 2018, *2*, 1187.

[8] C. Choi, K. Robert, G. Whang, P. Roussel, C. Lethien, B. Dunn, *Joule* 2021, *5*, 2466.

[9] J. W. Long, B. Dunn, D. R. Rolison, H. S. White, *Adv. Energy Mater.* 2020, *10*, 2002457.

[10] M. Sternad, M. Forster, M. Wilkening, *Sci. Rep.* 2016, *6*, 31712.

[11] D. S. Ashby, C. S. Choi, M. A. Edwards, A. A. Talin, H. S. White, B. S. Dunn, *ACS Appl. Energy Mater.* 2020, *3*, 8402.

[12] Y.-Q. Li, H. Shi, S.-B. Wang, Y.-T. Zhou, Z. Wen, X.-Y. Lang, Q. Jiang, *Nat. Commun.* 2019, *10*, 4292.

[13] D. Cao, Y. Xing, K. Tantratian, X. Wang, Y. Ma, A. Mukhopadhyay, Z. Cheng, Q. Zhang, Y. Jiao, L. Chen, H. Zhu, *Adv. Mater.* 2019, *31*, 1807313.

[14] Y. Bai, C. Liu, Y. Shan, T. Chen, Y. Zhao, C. Yu, H. Pang, *Adv. Energy Mater.* 2021, 2100346.

[15] X. Guo, S. Zheng, Y. Luo, H. Pang, *Chem. Eng. J.* 2020, *401*, 126005.

[16] X. Li, X. Yang, H. Xue, H. Pang, Q. Xu, *EnergyChem* 2020, *2*, 100027.

[17] C. S. Choi, J. Lau, J. Hur, L. Smith, C. Wang, B. Dunn, *Adv. Mater.* 2018, *30*, 1703772.

[18] P. Arora, Z. (John) Zhang, *Chem. Rev.* 2004, *104*, 4419.

[19] K. Liu, D. Zhuo, H.-W. Lee, W. Liu, D. Lin, Y. Lu, Y. Cui, *Adv. Mater.* 2017, *29*, 1603987.

[20] S. Rajendran, Z. Tang, A. George, A. Cannon, C. Neumann, A. Sawas, E. Ryan, A. Turchanin, L. M. R. Arava, *Adv. Energy Mater.* 2021, *11*, 2100666.

[21] Q. Cheng, W. He, X. Zhang, M. Li, X. Song, *RSC Adv.* 2016, *6*, 10250.

[22] C. Huang, C.-C. Lin, C.-Y. Tsai, R.-S. Juang, *Plasma Process. Polym.* 2013, *10*, 407.

[23] B. Li, Y. Li, D. Dai, K. Chang, H. Tang, Z. Chang, C. Wang, X.-Z. Yuan, H. Wang, *ACS Appl. Mater. Interfaces* 2015, *7*, 20184.

[24] D.-R. Deng, J. Lei, F. Xue, C.-D. Bai, X.-D. Lin, J.-C. Ye, M.-S. Zheng, Q.-F. Dong, *J. Mater. Chem. A* 2017, *5*, 23497.

[25] Y. Song, K. Wu, T. Zhang, L. Lu, Y. Guan, F. Zhou, X. Wang, Y. Yin, Y. Tan, F. Li, T. Tian, Y. Ni, H. Yao, S. Yu, *Adv. Mater.* 2019, *31*, 1905711.

[26] Y. Li, L. Yu, W. Hu, X. Hu, *J. Mater. Chem. A* 2020, *8*, 20294.

[27] M. Zhang, H. Mei, P. Chang, L. Cheng, *J. Mater. Chem. A* 2020, *8*, 10670.

[28] H. Lee, M. Yanilmaz, O. Toprakci, K. Fu, X. Zhang, *Energy Env. Sci* 2014, *7*, 3857.

[29] M. F. Lagadec, R. Zahn, V. Wood, *Nat. Energy* 2019, *4*, 16.

[30] I. C. Halalay, M. J. Lukitsch, M. P. Balogh, C. A. Wong, *J. Power Sources* 2013, *238*, 469.

[31] W. Song, A. Gu, G. Liang, L. Yuan, *Appl. Surf. Sci.* 2011, *257*, 4069.

[32] Y. Sun, C. J. Radke, B. D. McCloskey, J. M. Prausnitz, *J. Colloid Interface Sci.* 2018, *529*, 582.

[33] C. J. Orendorff, *Interface Mag.* 2012, *21*, 61.

[34] X. Wang, Y. Hu, L. Li, H. Fang, X. Fan, S. Li, *E-Polym.* 2019, *19*, 470.

[35] X. Jiang, X. Zhu, X. Ai, H. Yang, Y. Cao, *ACS Appl. Mater. Interfaces* 2017, *9*, 25970.

[36] R. Martinez-Duarte, M. Madou, *SU-8 Photolithography and Its Impact on Microfluidics*, Taylor And Francis, Hoboken, 2012.

[37] M. Cavasin, S. Giannis, M. Salvo, V. Casalegno, M. Sangermano, *J. Appl. Polym. Sci.* 2018, *135*, 46864.

[38] A. Emmerling, J. Fricke, *J. Sol-Gel Sci. Technol.* 1997, *8*, 781.

[39] S.-I. Tobishima, M. Arakawa, J.-I. Yamaki, *Electrochimica Acta* 1988, *33*, 239.

[40] M. Deepa, *Solid State Ion.* 2002, *152–153*, 253.

[41] G. Ferraresi, L. Czornomaz, C. Villevieille, P. Novák, M. El Kazzi, *ACS Appl. Mater. Interfaces* 2016, *8*, 29791.

[42] M. T. McDowell, S. W. Lee, W. D. Nix, Y. Cui, *Adv. Mater.* 2013, *25*, 4966.

[43] J. W. Wang, Y. He, F. Fan, X. H. Liu, S. Xia, Y. Liu, C. T. Harris, H. Li, J. Y. Huang, S. X. Mao, T. Zhu, *Nano Lett.* 2013, *13*, 709.

[44] X. Zhang, R. Kostecki, T. J. Richardson, J. K. Pugh, P. N. Ross, *J. Electrochem. Soc.* 2001, *148*, A1341.

[45] X. Chang, W. Li, J. Yang, L. Xu, J. Zheng, X. Li, *J. Mater. Chem. A* 2015, *3*, 3522.

[46] C. Pereira-Nabais, J. Światowska, M. Rosso, F. Ozanam, A. Seyeux, A. Gohier, P. Tran-Van, M. Cassir, P. Marcus, *ACS Appl. Mater. Interfaces* 2014, *6*, 13023.

[47] H. Zheng, L. Tan, G. Liu, X. Song, V. S. Battaglia, *J. Power Sources* 2012, *208*, 52.

[48] M. K. Y. Chan, C. Wolverton, J. P. Greeley, *J. Am. Chem. Soc.* 2012, *134*, 14362.

[49] S.-P. Kim, D. Datta, V. B. Shenoy, *J. Phys. Chem. C* 2014, *118*, 17247.

[50] X. Pan, X. Hong, L. Xu, Y. Li, M. Yan, L. Mai, *Nano Today* 2019, *28*, 100764.

[51] C. Lethien, J. Le Bideau, T. Brousse, *Energy Environ. Sci.* 2019, *12*, 96.

[52] J. B. Nielsen, R. L. Hanson, H. M. Almughamsi, C. Pang, T. R. Fish, A. T. Woolley, *Anal. Chem.* 2020, *92*, 150.

[53] A. Shiohara, B. Prieto-Simon, N. H. Voelcker, *J. Mater. Chem. B* 2021, *9*, 2129.

Chapter 6. Concluding Remarks

While rechargeable Li batteries have certainly shaped modern-day life, the field itself continues to grow and evolve in a number of directions and applications. From fundamental material challenges to application-driven materials design, this dissertation considers various promising directions and offers a broad perspective on the targets and technologies for the next generation of batteries.

The first section of this dissertation focuses on electrochemical interfaces, regions commonly prone to degradation. The Li metal interface is by far one of the most challenging interfaces due to the combined effect of the inevitable solid electrolyte interphase in addition to the age-old problem of Li dendrites upon repeated plating/stripping. The revisitation of Li metal after years of dormancy highlights the necessity of Li metal anodes in next generation high energy density batteries. This is particularly significant for emerging solid-state batteries whereby Li metal is required to access higher energy densities. The revival of Li metal batteries furthermore opens up a new era of Li metal research to re-address the safety and performance challenges from new perspectives and characterization techniques. In chapter 3, Li dendrites are revisited from the lens of interfacial coatings layers which serve as Li transport layers and confine Li deposition underneath the coating to effectively mitigate dendrite formation at the coating surface. While coatings have been previously studied, the mechanism of Li plating underneath coating layers has received far less attention and thus is less understood. Li-Sn coatings are fabricated through a solution-based approach resulting in microns thick coatings containing mixed nanocrystalline Li-Sn intermetallic and amorphous phases. Electrochemical analysis is used to better understand the kinetics of Li plating/stripping and the larger exchange current exhibited in the coated systems highlights the enhanced charge transfer kinetics relative to bare Li. Furthermore, the ability to tune the deposition location as a function of current density provides insights on the limitations and conditions required for plating underneath. Lastly, the use of state-of-the-art characterization

techniques such as Cryo-FIB SEM reveals the morphologies of lithium deposits above and below the coating layers, highlighting its dual role as a transport layer at lower current and nucleation substrate at higher currents. Further, the results from this work emphasize the under recognized importance of high exchange currents, fast Li transport through coatings, and provides the framework for designing future coating systems. The insights drawn from studying coatings on lithium interfaces also provides new opportunities to explore other challenging interfaces such as those on Na metal.

The fundamental mechanism of charge storage presents additional challenges, especially as one moves away from simple intercalation chemistries. The rapid rise of interest in conversion electrodes highlights the attractive appeal of multi-electron redox as a means to obtain higher specific capacities and thus higher energy densities. However, in order to access such high capacities, the issues of capacity fade and other loss mechanisms must be better understood in order to improve and make them competitive as commercial electrodes. The growing demand for higher energy density rechargeable batteries has placed the spotlight on FeS_2 which can provide energy density as a commercialized primary battery cathode but with limited reversibility demonstrated. While capacity fade in rechargeable FeS_2 has been a known problem for decades, the lack of congruency in the reaction pathways responsible for rechargeable FeS_2 has impeded in providing targeted solutions. Therefore, the work in Chapter 4 of this dissertation focuses on revisiting the reaction pathways in order to address he discrepancies and identify the key contributors to capacity loss. We highlight the formation of a new charge product (Fe_3S_4) at elevated temperatures and furthermore use its detection as a way to better understand the electrochemical reaction pathways of rechargeable FeS_2. From better understanding the reaction pathways to form Fe_3S_4, we establish a new electrochemical reaction pathway for FeS_2. Furthermore, the capacity losses observed in rechargeable FeS_2 are identified to 1) affect the charge product that can be formed and 2) shown to originate primarily from sulfur loss in the active

material. Based on the latter point, future work should be directed towards studying FeS_2 in electrolyte systems with little to no polysulfide and sulfur solubility (i.e. solid state electrolyte) as a means to circumvent capacity fade and maintain sulfur-rich charge products during electrochemical cycling. Lastly, in studying (de)lithiation of FeS_2 at elevated temperatures, the reaction pathways established in this work help bridge the gap in discrepancies in the products and intermediates reported over the past few decades while providing new insights on how to address the problems of capacity fade.

The last part of this dissertation switches the focus towards the challenges associated with miniaturization of batteries and more specifically the pursuit of on-chip battery systems. While batteries currently remain as external plug-and-play components of small devices, the integration of the battery onto the device as an on-chip battery provides a promising direction to address the bottlenecks in scaling down for next generation batteries. However, reducing the device and power source footprint provides its own set of unique challenges and opportunities to develop new materials and processes compatible with the semiconductor processing techniques used to make the devices themselves. For miniaturized electrochemical energy storage systems, spatially controlled and well-defined geometries and structures for electrode materials have been successfully demonstrated using photolithographic techniques. However, the limitation iin the device is often the electrolyte and more specifically the lack of a high ionic conductivity photopatternable solid state electrolyte which ultimately places limitations on high power applications. In Chapter 5 of this dissertation, a SU-8 photoresist is transformed it into a photopatternable porous separator with the use of an ionic liquid templating agent that is selectively removed after polymerization. The resulting porous separators demonstrate good adhesion, thermal, and mechanical properties making them suitable as on-chip separators. By infiltrating the porous separator with high ionic conductivity liquid electrolytes, fast ion transport can be achieved as shown through a series of electrochemical validation studies. The ability to

photopattern onto planar, porous, and three-dimensional architectures highlights the versatility of photoresist-based separators which can be extended to other electrolyte systems beyond the one presented in this particular work. Furthermore, the ability to conformally photopattern porous separators onto three dimensional architectures provides the basis for achieving high energy and high power density for on-chip batteries. Building off the research presented here, future work should focus on incorporating a slurry cathode into the three dimensional Si array and realize a truly 3D microbattery with high energy and high power performance.